

Lectures on the Theory of the Weak Interaction

MICHAEL E. PESKIN¹*SLAC, Stanford University, Menlo Park, CA 94025, USA*

ABSTRACT

I review aspects of the theory of the weak interaction in a set of lectures originally presented at the 2016 CERN-JINR European School of Particle Physics. The topics discussed are: (1) the experimental basis of the $V-A$ structure of the weak interaction; (2) precision electroweak measurements at the Z resonance; (3) the Goldstone Boson Equivalence Theorem; (4) the Standard Model theory of the Higgs boson; (5) the future program of precision study of the Higgs boson.

Lectures presented at the CERN-JINR
European School of Particle Physics
Skeikampen, Norway, June 15-28, 2016

¹Work supported by the US Department of Energy, contract DE-AC02-76SF00515.

Contents

1	Introduction	1
2	Formalism of the Standard Model	2
2.1	Gauge boson interactions	2
2.2	Massless fermions	6
3	Tests of the $V-A$ Interaction	8
3.1	Polarization in β decay	9
3.2	Muon decay	10
3.3	Pion decay	12
3.4	Neutrino deep inelastic scattering	13
3.5	e^+e^- annihilation at high energy	16
4	Precision electroweak measurements at the Z resonance	20
4.1	Properties of the Z boson in the Standard Model	22
4.2	Measurements of the Z properties	23
4.3	Constraints on oblique radiative corrections	33
5	The Goldstone Boson Equivalence Theorem	37
5.1	Questions about W and Z bosons at high energy	39
5.2	W polarization in top quark decay	41
5.3	High energy behavior in $e^+e^- \rightarrow W^+W^-$	43
5.4	Parametrizing corrections to the Yang-Mills vertex	47
5.5	W parton distributions	49
6	The Standard Model theory of Higgs boson decays	53
6.1	Decay modes of the Higgs boson	54
6.2	Study of the Higgs boson at the LHC	62

7	Precision measurements of the Higgs boson properties	67
7.1	The mystery of electroweak symmetry breaking	69
7.2	Expectations for the Higgs boson in theories beyond the Standard Model	72
7.3	The Decoupling Theorem	75
7.4	Effects on the Higgs boson couplings from models of new physics . . .	76
7.5	Measurement of the Higgs boson properties at e^+e^- colliders	81
8	Conclusions	87

1 Introduction

Today, all eyes in particle physics are on the Higgs boson. This particle has been central to the structure of our theory of weak interactions ever since Weinberg and Salam first wrote down what we now call the Standard Model of this interaction in 1967 [1,2]. As our understanding of particle physics developed over the following decades, what lagged behind was our knowledge of this particle and its interactions. Increasingly, the remaining mysteries of particle physics became centered on this particle and the Higgs field of which it is a part.

In 2012, the Higgs boson was finally discovered by the ATLAS and CMS experiments at the LHC [3,4]. Finally, we have the opportunity to study this particle in detail and to learn some of its secrets by direct observation. Many students at this summer school, and many others around the world, are involved in this endeavor. So it is worthwhile to review the theory of the Higgs boson and the broader theory of weak interactions in which it is embedded. That is the purpose of these lectures.

To learn where we are going, it is important to understand thoroughly where we have been. For this reason, the first half of this lecture series is devoted to historical topics. In Section 2, I review the basic formulae of the Standard Model and set up my notation. An important property of the Standard Model is that, unexpectedly at first sight, charge-changing weak interactions couple only to left-handed-polarized fermions. This structure, called the $V-A$ interaction, is the reason that we need the Higgs field in the first place. In Section 3, I review the most convincing experimental tests of $V-A$. Section 4 reviews the precision measurements on the weak interaction made possible by the e^+e^- experiments of the 1990's at the Z resonance. These experiments confirmed the basic structure of the Standard Model and made the Higgs field a necessity.

One aspect of the Higgs field that is subtle and difficult to understand but very powerful in its application is the influence of the Higgs field on the high-energy dynamics of vector bosons W and Z . Section 5 is devoted to this topic. The physics of W and Z bosons at high energy is full of seemingly mysterious enhancements and cancellations. The rule that explains these is the connection to the Higgs field through a result called the Goldstone Boson Equivalence Theorem, first enunciated by Cornwall, Levin, and Tiktopoulos and Vayonakis [5,6]. In Section 5, I explain this theorem and illustrate the way it controls the energy-dependence of a number of interesting high-energy processes.

In Sections 6 and 7, I turn to the study of the Higgs boson itself. Section 6 is devoted to the Standard Model theory of the Higgs boson. I will review the general properties of the Higgs boson and explain in some details its expected pattern of decay models. Section 7 is devoted to the remaining mysteries of the Higgs boson and the possibility of their elucidation through a future program of precision measurements.

2 Formalism of the Standard Model

To begin, I write the formalism of the Standard Model (SM) in a form convenient for the analysis given these lectures. The formalism of the SM is standard material for students of particle physics, so I assume that you have seen this before. It is explained more carefully in many textbooks (for example, [7,8]).

2.1 Gauge boson interactions

The SM is a gauge theory based on the symmetry group $SU(2) \times U(1)$. A gauge theory includes interactions mediated by vector bosons, one boson for each generator of the gauge symmetry G . The coupling of spin 0 and spin $\frac{1}{2}$ particles to these vector bosons is highly restricted by the requirements of gauge symmetry. The interactions of these fermions and scalars with one another is much less restricted, subject only to the constraints of the symmetry G as a global symmetry. Thus, the theory of fermions and vector bosons is extremely tight, while the introduction of a scalar field such as the Higgs field introduces a large number of new and somewhat uncontrolled interaction terms.

The SM contains 4 vector bosons corresponding to the 3 generators of $SU(2)$ and 1 generator of $U(1)$. I will call these

$$A_\mu^a, \quad B_\mu, \quad (1)$$

with $a = 1, 2, 3$. These couple to fermion and scalar fields only through the replacement of the derivatives by covariant derivative

$$\partial_\mu \rightarrow D_\mu = (\partial_\mu - igA_\mu^a t^a), \quad (2)$$

where t^a is the generator of G in the representation to which the fermions or scalars are assigned. For the SM, fermion and scalar fields are assigned $SU(2)$, or weak isospin, quantum numbers 0 or $\frac{1}{2}$ and a $U(1)$, or hypercharge, quantum number Y . The covariant derivative is then written more explicitly as

$$D_\mu = \partial_\mu - igA_\mu^a t^a - ig' B_\mu Y, \quad (3)$$

with

$$t^a = 0 \text{ for } I = 0, \quad t^a = \frac{\sigma^a}{2} \text{ for } I = \frac{1}{2}. \quad (4)$$

This formalism makes precise predictions for the coupling of the weak interaction vector bosons to quarks and leptons, and to the Higgs field. To obtain the masses of the vector bosons, we need to make one more postulate: The Higgs field obtains a nonzero value in the ground state of nature, the vacuum state, thus spontaneously

breaking the $SU(2) \times U(1)$ symmetry. This postulate is physically very nontrivial. I will discuss its foundation and implications in some detail in Section 7. However, for now, I will consider this a known aspect of the SM.

We assign the Higgs field φ the $SU(2) \times U(1)$ quantum numbers $I = \frac{1}{2}$, $Y = \frac{1}{2}$. The Higgs field is thus a spinor in isospin space, a 2-component complex-valued vector of fields

$$\varphi = \begin{pmatrix} \varphi^+ \\ \varphi^0 \end{pmatrix} \quad (5)$$

The action of an $SU(2) \times U(1)$ transformation on this field is

$$\varphi \rightarrow \exp\left[i\alpha^a \frac{\sigma^a}{2} + i\beta \frac{1}{2}\right] \begin{pmatrix} \varphi^+ \\ \varphi^0 \end{pmatrix} . \quad (6)$$

If φ obtains a nonzero vacuum value, we can rotate this by an $SU(2)$ symmetry transformation into the form

$$\langle \varphi \rangle = \frac{1}{\sqrt{2}} \begin{pmatrix} 0 \\ v \end{pmatrix} . \quad (7)$$

where v is a nonzero value with the dimensions of GeV. Once $\langle \varphi \rangle$ is in this form, any $SU(2) \times U(1)$ transformation will disturb it, except for the particular direction

$$\alpha^3 = \beta , \quad (8)$$

which corresponds to a $U(1)$ symmetry generated by $Q = (I^3 + Y)$. We say that the $SU(2) \times U(1)$ symmetry generated by (I^a, Y) is spontaneously broken, leaving unbroken only the $U(1)$ subgroup generated by Q .

This already gives us enough information to work out the mass spectrum of the vector bosons. The kinetic energy term for φ in the SM Lagrangian is

$$\mathbb{L} = \left| D_\mu \varphi \right|^2 \quad (9)$$

Replacing φ by its vacuum value (7), this becomes

$$\mathbb{L} = \frac{1}{2} (0 \quad v) \left(g \frac{\sigma^a}{2} A_\mu^a + g' \frac{1}{2} B_\mu \right)^2 \begin{pmatrix} 0 \\ v \end{pmatrix} . \quad (10)$$

Multiplying this out and taking the matrix element, we find, from the σ^1 and σ^2 terms

$$\frac{g^2 v^2}{8} \left[(A_\mu^1)^2 + (A_\mu^2)^2 \right] , \quad (11)$$

and, from the remaining terms

$$\frac{v^2}{8} \left(-g A_\mu^3 + g' B_\mu \right)^2 \quad (12)$$

So, three linear combinations of the vector fields obtain mass by virtue of the spontaneous symmetry breaking. This is the mechanism of mass generation called the *Higgs mechanism* [9,10,11]. The mass eigenstates are

$$\begin{aligned} W^\pm &= (A^1 \mp iA^2)/\sqrt{2} & m_W^2 &= g^2 v^2/4 \\ Z &= (gA^3 - g'B)/\sqrt{g^2 + g'^2} & m_Z^2 &= (g^2 + g'^2)v^2/4 \\ A &= (g'A^3 + gB)/\sqrt{g^2 + g'^2} & m_A^2 &= 0 \end{aligned} \quad (13)$$

As we will see more clearly in a moment, the massless boson A is associated with the unbroken gauge symmetry Q . The combination of local gauge symmetry and the Higgs mechanism is the only known way to give mass to a vector boson that is consistent with Lorentz invariance and the positivity of the theory.

The linear combinations in (13) motivate the definition of the *weak mixing angle* θ_w , defined by

$$\begin{aligned} \cos \theta_w &\equiv c_w = g/\sqrt{g^2 + g'^2} \\ \sin \theta_w &\equiv s_w = g'/\sqrt{g^2 + g'^2} . \end{aligned} \quad (14)$$

The factors c_w , s_w will appear throughout the formulae that appear in these lectures. For reference, the value of the weak mixing angle turns out to be such that

$$s_w^2 \approx 0.231 \quad (15)$$

I will describe the measurement of s_w in some detail in Section 3.

An important relation that follows from (13), (14) is

$$m_W = m_Z c_w . \quad (16)$$

This is a nontrivial consequence of the quantum number assignments for the Higgs field, and the statement that the masses of W and Z come only from the vacuum value of φ . Using the Particle Data Group values for the masses [12] and the value (15), we find

$$80.385 \text{ GeV} \approx 91.188 \text{ GeV} \cdot 0.877 = 79.965 \text{ GeV} . \quad (17)$$

so this prediction works well already at the leading order. We will see in Section 3 that, when radiative corrections are included, the relation (16) is satisfied to better than 1 part per mil.

Once we have the mass eigenstates of the vector bosons, the couplings of quarks and leptons to these bosons can be worked out from the expression (3) for the covariant derivative. The terms in (3) involving A_μ^1 and A_μ^2 appear only for $I = \frac{1}{2}$ particles and can be recast as

$$-i\frac{g}{\sqrt{2}}(W_\mu^+ \sigma^+ + W_\mu^- \sigma^-) , \quad (18)$$

The W bosons couple only to $SU(2)$ doublets, with universal strength g .

The terms with A_μ^3 and B_μ can similarly be recast in terms of Z_μ and A_μ ,

$$\begin{aligned}
-igA_\mu^3 - ig'B_\mu Y &= -i\sqrt{g^2 + g'^2} \left[c_w(c_w Z_\mu + s_w A_\mu) I^3 + s_w(-s_w Z_\mu + c_w A_\mu) \right] \\
&= -i\sqrt{g^2 + g'^2} \left[s_w c_w A_\mu (I^3 + Y) + Z_\mu (c_w^2 I^3 - s_w^2 Y) \right] \\
&= -i\sqrt{g^2 + g'^2} \left[s_w c_w A_\mu (I^3 + Y) + Z_\mu (I^3 - s_w^2 (I^3 + Y)) \right]. \quad (19)
\end{aligned}$$

We now see explicitly that the massless gauge boson A_μ couples to $Q = (I^3 + Y)$, as we had anticipated. Its coupling constant is

$$e = s_w c_w \sqrt{g^2 + g'^2} = \frac{gg'}{\sqrt{g^2 + g'^2}}. \quad (20)$$

We can then identify this boson with the photon and the coupling constant e with the strength of electric charge. The quantity Q is the (numerical) electric charge of each given fermion or boson species. The expression (19) then simplifies to

$$-ieA_\mu Q - i\frac{e}{s_w c_s} Z_\mu Q_Z, \quad (21)$$

where the Z charge is

$$Q_Z = (I^3 - s_w^2 Q). \quad (22)$$

To complete the specification of the SM, we assign the $SU(2) \times U(1)$ quantum numbers to the quarks and leptons in each generation. As I will explain below, each quark or lepton is build up from fields of left- and right-handed chirality, associated with massless left- and right-handed particles and massless right- and left-handed antiparticles. For the applications developed in Sections 3–5, it will almost always be appropriate to ignore the masses of quarks and leptons, so these quantum number assignments will apply literally. The generation of masses for quarks and leptons is part of the physics of the Higgs field, which we will discuss beginning in Section 6.

In the SM, the left-handed fields are assigned $I = \frac{1}{2}$, and the right-handed fields are assigned $I = 0$. It is not so easy to understand how these assignments come down from fundamental theory. They are required by experiment, as I will explain in later in this section.

With this understanding, we can assign quantum numbers to the quarks and leptons as

$$\begin{aligned}
\nu_L : I^3 = +\frac{1}{2}, Y = -\frac{1}{2}, Q = 0 & \quad \nu_R : I^3 = 0, Y = 0, Q = 0 \\
e_L : I^3 = -\frac{1}{2}, Y = -\frac{1}{2}, Q = -1 & \quad e_R : I^3 = 0, Y = -1, Q = -1
\end{aligned}$$

$$\begin{aligned}
u_L &: I^3 = +\frac{1}{2}, Y = \frac{1}{6}, Q = \frac{2}{3} & u_R &: I^3 = 0, Y = \frac{2}{3}, Q = \frac{2}{3} \\
d_L &: I^3 = +\frac{1}{2}, Y = \frac{1}{6}, Q = -\frac{1}{3} & d_R &: I^3 = 0, Y = -\frac{1}{3}, Q = -\frac{1}{3}
\end{aligned} \tag{23}$$

The ν_L and e_L , and the u_L and d_L , belong to the same $SU(2)$ multiplet, so they must be assigned the same hypercharge Y . Note that (23) gives the correct electric charge assignments for all quarks and leptons. The ν_R do not couple to the SM gauge fields and will play no role in the results reviewed in these lectures.

2.2 Massless fermions

The idea that massless fermions can be separated into left- and right-handed components will play a major role throughout these lectures. In this sentence, I introduce some notation that makes it especially easy to apply this idea.

To begin, write the the 4-component Dirac spinor and the Dirac matrices as

$$\Psi = \begin{pmatrix} \psi_L \\ \psi_R \end{pmatrix} \quad \gamma^\mu = \begin{pmatrix} 0 & \sigma^\mu \\ \bar{\sigma}^\mu & 0 \end{pmatrix}, \tag{24}$$

with

$$\sigma^\mu = (1, \vec{\sigma})^\mu \quad \bar{\sigma}^\mu = (1, -\vec{\sigma})^\mu. \tag{25}$$

In this representation, the vector current takes the form

$$j^\mu = \bar{\Psi} \gamma^\mu \Psi = \psi_L^\dagger \bar{\sigma}^\mu \psi_L + \psi_R^\dagger \sigma^\mu \psi_R \tag{26}$$

and splits neatly into pieces that involve only the L or R fields. The L and R fields are mixed by the fermion mass term. In circumstances in which we can ignore the fermion masses, the L and R fermion numbers are separately conserved. We can treat ψ_L and ψ_R as completely independent species and assign them different quantum numbers, as we have already in (23). The label L, R is called *chirality*. For massless fermions, the chirality of the fields and the helicity of the particles are identical. For massive fermions, there is a change of basis from the chirality states to the helicity eigenstates.

The spinors for massless fermions are very simple. In the basis (24), we can write these spinors as

$$U(p) = \begin{pmatrix} u_L \\ u_R \end{pmatrix} \quad V(p) = \begin{pmatrix} v_R \\ v_L \end{pmatrix}. \tag{27}$$

For massless fermions, where the helicity and chirality states are identical, the spinors for a fermion with left-handed spin have $u_R = 0$ and the spinors for an antifermion with right-handed spin have $v_L = 0$; the opposite is true for a right-handed fermion and

a left-handed antifermion. The nonzero spinor components for a massless fermion of energy E take the form

$$\begin{aligned} u_L(p) &= \sqrt{2E} \xi_L & v_R(p) &= \sqrt{2E} \xi_L \\ u_R(p) &= \sqrt{2E} \xi_R & v_L(p) &= \sqrt{2E} \xi_R \end{aligned} \quad (28)$$

where ξ_R is the spin-up and ξ_L is the spin-down 2-component spinor along the direction of motion. For example, for a fermion or antifermion moving in the $\hat{3}$ direction,

$$\xi_L = \begin{pmatrix} 0 \\ 1 \end{pmatrix} \quad \xi_R = \begin{pmatrix} 1 \\ 0 \end{pmatrix} . \quad (29)$$

Spinors for other directions are obtained by rotating these according to the usual formulae for spin $\frac{1}{2}$. The reversal for antifermions can be thought of by viewing right-handed (for example) antifermions as holes in the Dirac sea of left-handed fermions. For a massive fermion moving in the $\hat{3}$ direction, with

$$p^\mu = (E, 0, 0, p)^\mu , \quad (30)$$

the solutions to the Dirac equation are

$$\begin{aligned} U_L(p) &= \begin{pmatrix} \sqrt{E+p} \xi_L \\ \sqrt{E-p} \xi_L \end{pmatrix} & V_R(p) &= \begin{pmatrix} \sqrt{E+p} \xi_L \\ -\sqrt{E-p} \xi_L \end{pmatrix} \\ U_R(p) &= \begin{pmatrix} \sqrt{E-p} \xi_R \\ \sqrt{E+p} \xi_R \end{pmatrix} & V_L(p) &= \begin{pmatrix} \sqrt{E-p} \xi_R \\ -\sqrt{E+p} \xi_R \end{pmatrix} , \end{aligned} \quad (31)$$

with ξ_L, ξ_R given by (29). These formulae go over to (28) in the zero mass limit.

The matrix elements for creation or annihilation of a massless fermion pair will appear very often in these lectures. For annihilation of a fermion pair colliding along the $\hat{3}$ axis,

$$\begin{aligned} \langle 0 | j^\mu | e_L^- e_R^+ \rangle &= v_R^\dagger \bar{\sigma}^\mu u_L \\ &= \sqrt{2E} \begin{pmatrix} -1 & 0 \end{pmatrix} (1, -\sigma^1, -\sigma^2, -\sigma^3) \sqrt{2E} \begin{pmatrix} 0 \\ 1 \end{pmatrix} , \end{aligned} \quad (32)$$

Note that I have rotated the e^+ spinor appropriately by 180° . This gives

$$\langle 0 | j^\mu | e_L^- e_R^+ \rangle = 2E (0, 1, -i, 0)^\mu . \quad (33)$$

It is illuminating to write this as

$$\langle 0 | j^\mu | e_L^- e_R^+ \rangle = 2\sqrt{2E} \epsilon_-^\mu , \quad (34)$$

where

$$\epsilon_+^\mu = \frac{1}{\sqrt{2}}(0, 1, +i, 0)^\mu \quad \epsilon_-^\mu = \frac{1}{\sqrt{2}}(0, 1, -i, 0)^\mu \quad (35)$$

are the vectors of $J^3 = \pm 1$ along the $\hat{3}$ axis. The total spin angular momentum of the annihilating fermions ($J = 1$) is transferred to the current and, eventually, to the final state.

More generally, we find

$$\begin{aligned}
\langle 0 | j^\mu | e_R^- e_L^+ \rangle &= 2\sqrt{2}E \epsilon_+^\mu \\
\langle 0 | j^\mu | e_L^- e_R^+ \rangle &= 2\sqrt{2}E \epsilon_-^\mu \\
\langle e_R^- e_L^+ | j^\mu | 0 \rangle &= 2\sqrt{2}E \epsilon_+^{*\mu} \\
\langle e_L^- e_R^+ | j^\mu | 0 \rangle &= 2\sqrt{2}E \epsilon_-^{*\mu} .
\end{aligned} \tag{36}$$

For an annihilation process such as $e_L^- e_R^+ \rightarrow \mu_L^- \mu_R^+$ with annihilation by a current and creation by another current, the spinors appear as

$$(u_L^\dagger \bar{\sigma}^\mu v_R)(v_R^\dagger \bar{\sigma}_\mu u_L) = 2(2E)^2 \epsilon_-^{*\mu} \cdot \epsilon_- . \tag{37}$$

To evaluate this, rotate the ϵ_- vector for the muons into the muon direction. If the muons come off at polar angle θ , this gives

$$\epsilon_-^{*\mu} = \frac{1}{\sqrt{2}}(0, \cos \theta, -i, -\sin \theta) . \tag{38}$$

Then (37) becomes

$$2(2E)^2 \epsilon_-^{*\mu} \cdot \epsilon_- = s(1 + \cos \theta) = -2u , \tag{39}$$

in terms of the usual kinematic invariants s, t, u . Another way to write this is

$$|(u_L^\dagger \bar{\sigma}^\mu v_R)(v_R^\dagger \bar{\sigma}_\mu u_L)|^2 = 4(2p_{e^-} \cdot p_{\mu^+})(2p_{e^+} \cdot p_{\mu^-}) . \tag{40}$$

Similarly, for $e_L^- e_R^+ \rightarrow \mu_R^- \mu_L^+$,

$$|(u_R^\dagger \bar{\sigma}^\mu v_L)(v_R^\dagger \bar{\sigma}_\mu u_L)|^2 = 4(2p_{e^+} \cdot p_{\mu^+})(2p_{e^-} \cdot p_{\mu^-}) . \tag{41}$$

It is a nice exercise to check these answers using the usual trace theorems. The trace theorems are more automatic, but the helicity formalism gives more physical insight.

3 Tests of the $V-A$ Interaction

The property that the W boson only couples to fermions of left-handed chirality is a crucial property of the SM. It is responsible for many of the surprising features of the weak interactions, both the most attractive and the most puzzling ones. It is therefore important to understand that this feature is extremely well supported experimentally. In this section, I review the most convincing experimental tests of this property.

3.1 Polarization in β decay

The first applications discussed in this section involve exchange of W bosons at low energy. In this limit, we can simplify the W propagator to a pointlike interaction

$$\frac{-i}{q^2 - m_W^2} \rightarrow \frac{i}{m_W^2} . \quad (42)$$

In this limit, the W exchange can be represented by the product of currents

$$\Delta\mathbf{L} = \frac{g^2}{2m_W^2} J_\mu^+ J^{-\mu} , \quad (43)$$

where

$$\begin{aligned} J_\mu^+ &= \nu_{eL}^\dagger \bar{\sigma}_\mu e_L + u_L^\dagger \bar{\sigma}_\mu d_L + \dots \\ J_\mu^- &= e_L^\dagger \bar{\sigma}_\mu \nu_{eL} + d_L^\dagger \bar{\sigma}_\mu u_L + \dots \end{aligned} \quad (44)$$

Here and henceforth in these lectures, I replace the label ψ with a label that gives the flavor quantum numbers of the field. In (44), I write explicitly the terms associated with the first generation quarks and leptons; the omitted terms are those for the higher generations. I ignore Cabibbo mixing, a reasonable approximation for the topics discussed in these lectures. I will also ignore the masses of the neutrinos.

The theory (43) is called the $V-A$ interaction, since

$$u_L^\dagger \bar{\sigma}^\mu d_L = \bar{U} \gamma^\mu \frac{1 - \gamma^5}{2} D , \quad (45)$$

the difference of a vector and an axial vector current. The coefficient in (43) is conventionally represented by the Fermi constant G_F ,

$$\frac{g^2}{2m_W^2} = \frac{4G_F}{\sqrt{2}} . \quad (46)$$

This interaction has *maximal parity violation* in charge-changing weak interactions.

The simplest consequence of $V-A$ is that electrons emitted in β decay should be preferentially left-handed polarized. Since the energies of electrons in β decay are of order 1 MeV, it is typically not a good approximation to ignore the electron mass. However, since in $V-A$ the electron is produced in the L chirality eigenstate, we can work out the polarization from the relative magnitude of the u_L terms in the left- and right-handed helicity massive spinors given in (31). The electron polarization, in the left-handed sense, is then given by

$$\text{Pol}(e^-) = \frac{(\sqrt{E+p})^2 - (\sqrt{E-p})^2}{(\sqrt{E+p})^2 + (\sqrt{E-p})^2} = \frac{p}{E} = \frac{v}{c} . \quad (47)$$

A data compilation is shown in Fig. 1 [13]. Careful experiments both at high and low electron energies verify the regularity (47).

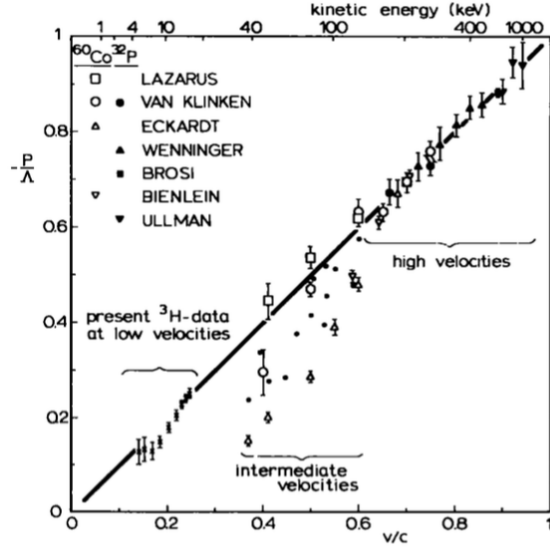


Figure 1: Polarization of the electron emitted in β decay for a variety of β decay transitions in different nuclei, from [13].

3.2 Muon decay

The $V-A$ interaction also has striking consequences for the electron energy and polarization in muon decay.

It is not difficult to work out the basic formulae for muon decay. In $V-A$ theory, and ignoring the electron mass, muon decay has a massive muon at rest decaying to $\nu_{\mu L} e_L^- \bar{\nu}_{e R}$. For the muon at rest, averaged over polarizations, we find, instead of (40),

$$|(u_L^\dagger \bar{\sigma}^\mu v_R)(v_R^\dagger \bar{\sigma}_\mu u_L)|^2 = 2(2p_{e^-} \cdot p_\nu)(2p_{\bar{\nu}} \cdot p_{\mu^-}) . \quad (48)$$

To integrate this over phase space, let

$$x_i = \frac{2p_i \cdot p_\mu}{p_\mu^2} , \quad (49)$$

where $i = e, \nu, \bar{\nu}$. Conservation of energy-momentum $p_\mu = p_e + p_\nu + p_{\bar{\nu}}$ implies

$$x_e + x_\nu + x_{\bar{\nu}} = 2 . \quad (50)$$

Each x_i takes the maximum value 1 when that massless particle recoils against the other two massless particles. Note also that

$$2p_e \cdot p_\nu = (p_e + p_\nu)^2 = (p_\mu - p_{\bar{\nu}})^2 = m_\mu^2(1 - x_{\bar{\nu}}) . \quad (51)$$

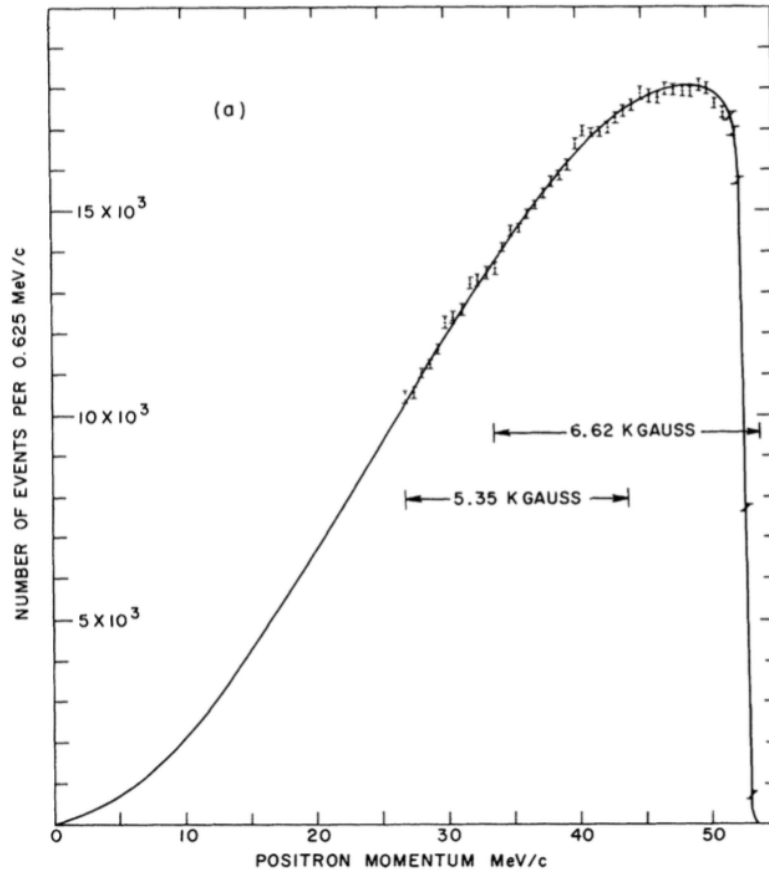


Figure 2: Energy spectrum of e^+ in μ^+ decay at rest, from [14].

Three-body phase space takes a simple form in the x_i variables,

$$\int d\Pi_3 = \frac{m_\mu^2}{128\pi^3} \int dx_e dx_{\bar{\nu}} . \quad (52)$$

Assembling the pieces, the muon decay rate is predicted to be

$$\Gamma = \frac{1}{2m_\mu} \left(\frac{4G_F}{\sqrt{2}} \right)^2 \frac{m_\mu^2}{128\pi^3} \int dx_e dx_{\bar{\nu}} 2m_\mu^4 x_{\bar{\nu}} (1 - x_{\bar{\nu}}) . \quad (53)$$

The integral over $x_{\bar{\nu}}$ is

$$\int_{1-x_e}^1 dx_{\bar{\nu}} x_{\bar{\nu}} (1 - x_{\bar{\nu}}) = \frac{1}{2} x_e^2 - \frac{1}{3} x_e^3 . \quad (54)$$

Then finally we find for the electron energy distribution

$$\frac{d\Gamma}{dx_e} = \frac{G_F^2 m_\mu^5}{16\pi^3} \left(\frac{x_e^2}{2} - \frac{x_e^3}{3} \right) . \quad (55)$$

This shape of this distribution is quite characteristic, with a double zero at $E_e = 0$ and zero slope at the endpoint at $E_e = m_\mu/2$. Both effects are slightly rounded by radiative corrections, but, with these taken into account, the prediction agrees with the measured spectrum to high precision, as shown in Fig. 2 [14].

3.3 Pion decay

Charged pion decay is mediated by the $V-A$ interaction

$$\frac{4G_F}{\sqrt{2}} (d_L^\dagger \bar{\sigma}^\mu u_L) \left(\nu_{eL}^\dagger \bar{\sigma}_\mu e_L + \nu_{\mu L}^\dagger \bar{\sigma}_\mu \mu_L \right) \quad (56)$$

At first sight, it might seem that the π^+ must decay equally often to e^+ and μ^+ . Experimentally, almost all pion decays are to μ^+ . Can this be reconciled with $V-A$?

The pion matrix element is

$$\langle 0 | d_L^\dagger \bar{\sigma}^\mu u_L | \pi^+(p) \rangle = -i \frac{1}{2} F_\pi p^\mu , \quad (57)$$

where F_π is the pion decay constant, equal to 135 MeV. The matrix element of (56) then evaluates to

$$\frac{4G_F}{\sqrt{2}} \cdot \left(-\frac{i}{2} F_\pi \right) p^\mu U_{\nu L}^\dagger \bar{\sigma}_\mu V_{\ell^+} . \quad (58)$$

The pion is at rest, so

$$p^\mu \bar{\sigma}_\mu = m_\pi \cdot 1 . \quad (59)$$

The neutrino is (essentially) massless and therefore must be left-handed. The pion has spin 0, so angular momentum requires that the ℓ^+ is also left-handed. But, from (31), the lepton spinor is then

$$V_L = \begin{pmatrix} \sqrt{E-p} \xi_R \\ \times \end{pmatrix} \quad (60)$$

The matrix element (58) reduces to

$$i \frac{4G_F}{\sqrt{2}} \cdot \left(\frac{1}{2}F_\pi\right) \sqrt{2E_\nu m_\pi} \sqrt{E_\ell - p_\ell} . \quad (61)$$

Two-body kinematics gives $E_\nu = p_\nu = p_\ell = (m_\pi^2 - m_\ell^2)/2m_\pi$. Then $(E_\ell - p_\ell) = m_\ell^2/m_\pi^2$. Phase space includes the factor $2p_\ell/m_\pi$, which brings another factor of $(E_\ell - p_\ell)$. Finally we find

$$\Gamma(\pi^+ \rightarrow \ell^+ \nu) = \frac{G_F^2 m_\pi^3 F_\pi^2 m_\ell^2}{8\pi m_\pi^2} \left(1 - \frac{m_\ell^2}{m_\pi^2}\right)^2 . \quad (62)$$

The overall factor m_ℓ^2/m_π^2 comes from the matrix element (60). Angular momentum conservation requires the ℓ^+ to have the wrong helicity with respect to $V-A$, accounting for this suppression factor.

The result (62) leads to the ratio of branching fractions

$$\frac{BR(\pi^+ \rightarrow e^+ \nu_e)}{BR(\pi^+ \rightarrow \mu^+ \nu_\mu)} = \frac{m_e^2}{m_\mu^2} \left(\frac{m_\pi^2 - m_e^2}{m_\pi^2 - m_\mu^2}\right)^2 = 1.28 \times 10^{-4} , \quad (63)$$

in good agreement with the observed value 1.23×10^{-4} .

3.4 Neutrino deep inelastic scattering

The helicity structure of the $V-A$ interaction is also seen in the energy distributions in deep inelastic neutrino scattering. For electrons, deep inelastic scattering is the scattering from a proton or nuclear target in which the momentum transfer is large and the target is disrupted to a high mass hadronic state. The kinematics is shown in Fig. 3(a). In the leading order of QCD, deep inelastic scattering is described by the scattering for the electron from a single quark in the parton distribution of the target. This kinematics is shown in Fig. 3(b).

Neutrino deep inelastic scattering experiments are done in the following way: One first creates a high-energy pion beam by scattering protons from a target. Then the pions are allowed to decay, producing a beam of neutrinos and muons. The beam is made to pass through a long path length of absorber to remove the muons and residual pions and other hadrons. Finally, the neutrinos are allowed to interact with a large-volume detector. A charged-current neutrino reaction then leads to a

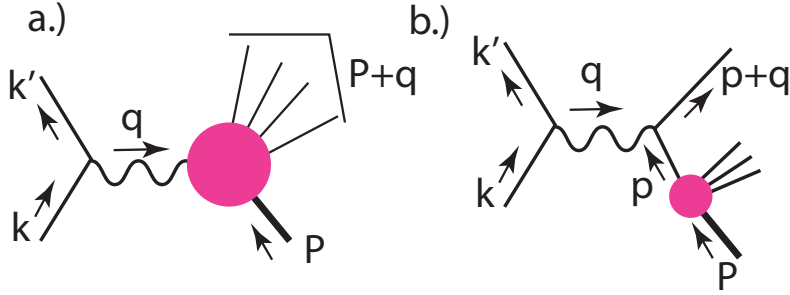


Figure 3: Kinematics of neutrino deep inelastic scattering: (a) for neutrino scattering from a proton or heavy nucleus, (b) for neutrino scattering from a quark in the parton model description.

scattering event whose result is a μ^\pm , depending on the charge of the decaying pion, and a high-multiplicity hadronic system.

If k is the initial momentum of the neutrino, k' is the final momentum of the muon, and P is the initial momentum of the target proton, we let $q = (k - k')$ and define the Lorentz invariants

$$\begin{aligned} s &= (k + P)^2 & Q^2 &= -q^2 \\ x &= \frac{Q^2}{2P \cdot q} & y &= \frac{2P \cdot q}{2P \cdot k} \end{aligned} \quad (64)$$

We are interested in the deep inelastic limit $Q^2 \gg P^2 = m_p^2$. Then $s \approx 2p \cdot k$ and $Q^2 = xys$. In the lab frame $P = (m_p, \vec{0})$, so $y = q^0/k^0$, the fraction of the initial neutrino energy transferred to the proton. To the extent that the initial neutrino energy k^0 is known, all of the invariants x , y , and Q^2 can be determined by measurement of the final muon momentum.

At leading order in QCD, a deep inelastic reaction is an essentially elastic lepton-quark scattering, for example, $\nu + d \rightarrow \mu^- + u$. Using Feynman's parton model, which is also the basis for QCD predictions at hadron colliders, we model the proton or nuclear target as a collection of quarks and antiquarks that move collinearly and share the total momentum of the proton. Let p be the momentum of the initial quark, and approximate

$$p = \xi P, \quad (65)$$

where $0 < \xi < 1$. The quarks might also have transverse momentum relative to the proton, but this is ignorable if the momentum transfer Q^2 from the neutrino scattering is large.

The final momentum of the quark is then $p + q$. The condition that this quark is

on-shell is

$$0 = (p + q)^2 = 2p \cdot q + q^2 = 2\xi P \cdot q - Q^2 . \quad (66)$$

Then

$$\xi = \frac{Q^2}{2P \cdot q} = x . \quad (67)$$

This is a remarkable result, also due to Feynman: To the leading order in QCD, deep inelastic scattering events at a given value of the invariant x arise from scattering from quarks or antiquarks in the proton with momentum fraction $\xi = x$.

We can now evaluate the kinematic invariants for a neutrino-quark scattering event. I call these \hat{s} , \hat{t} , \hat{u} to distinguish them from the invariants of neutrino-proton scattering. First,

$$\hat{s} = (p + k)^2 = 2p \cdot k = 2\xi P \cdot k = x s . \quad (68)$$

The momentum transfer can be evaluated from the lepton side, so

$$\hat{t} = q^2 = -Q^2 . \quad (69)$$

Finally, for scattering of approximately massless particles, $s + t + u = 0$, so

$$\hat{u} = xs - Q^2 = xs(1 - y) . \quad (70)$$

The aspect of the deep inelastic scattering cross section that is most important for the subject of this lecture is the distribution in y . To begin, consider the deep inelastic scattering of a ν_μ . The quark-level reaction is

$$\nu + d \rightarrow \mu^- + u \quad (71)$$

In the $V-A$ theory, the ν and the d must be left-handed. Similarly to (41),

$$|(u_L^\dagger(\mu^-)\bar{\sigma}^\mu u_L(\nu))(u_L^\dagger(u)\bar{\sigma}_\mu u_L(d))|^2 = 4(2p_{\mu^-} \cdot p_u)(2p_\nu \cdot p_d) = 4\hat{s}^2 . \quad (72)$$

On the other hand, antineutrino scattering from a quark, which proceeds by the reaction

$$\bar{\nu} + u \rightarrow \mu^+ + d , \quad (73)$$

is, in $V-A$ theory, the scattering of a right-handed $\bar{\nu}$ and a left-handed u . Then

$$|(v_R^\dagger(\mu^+)\bar{\sigma}^\mu v_R(\bar{\nu}))(u_L^\dagger(u)\bar{\sigma}_\mu u_L(d))|^2 = 4(2p_{\mu^+} \cdot p_u)(2p_{\bar{\nu}} \cdot p_d) = 4\hat{u}^2 . \quad (74)$$

Inserting (68), (70), we see that the dependence of the deep inelastic scattering cross section on y should be

$$\begin{aligned} \frac{d\sigma}{dy}(\nu p \rightarrow \mu^- X) &\sim \hat{s}^2 \sim 1 \\ \frac{d\sigma}{dy}(\bar{\nu} p \rightarrow \mu^+ X) &\sim \hat{u}^2 \sim (1 - y)^2 . \end{aligned} \quad (75)$$

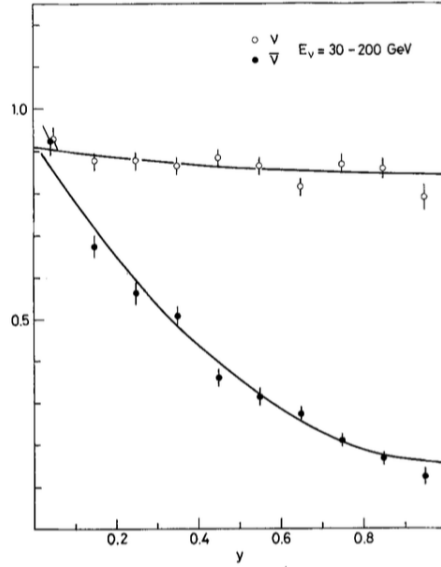


Figure 4: Dependence on the variable y of the cross sections for neutrino and antineutrino scattering on an iron target, from [15].

These results, which I have derived for a proton target, hold for any nuclear target under the assumption that we consider only scattering from quarks and not from antiquarks. For scattering from antiquarks, the dependence on y is reversed, with a $(1-y)^2$ dependence for neutrino scattering. The experimental result, from the CDHS experiment, a CERN neutrino experiment of the 1980's, is shown in Fig. 4 [15]. The y distribution for neutrino scattering is indeed almost flat, and that for antineutrino scattering is close to $(1-y)^2$. The deviations from these ideal results are consistent with arising from the antiquark content of the proton and neutron.

The same regularity can be seen in collider physics. For example, the Standard Model predicts that, in quark-antiquark annihilation to a W boson,

$$\begin{aligned} \frac{d\sigma}{d\cos\theta}(d\bar{u} \rightarrow W^- \rightarrow \mu^- \bar{\nu}) &\sim u^2 \sim (1 + \cos\theta)^2 \\ \frac{d\sigma}{d\cos\theta}(u\bar{d} \rightarrow W^+ \rightarrow \mu^+ \nu) &\sim t^2 \sim (1 - \cos\theta)^2, \end{aligned} \quad (76)$$

and these distributions are well verified at the LHC [16,17].

3.5 e^+e^- annihilation at high energy

The angular distributions in annihilation through the neutral current are more complex, first, because of photon- Z interference, and, second, because the weak neutral current couples to both left- and right-handed quarks and leptons.

To write formulae for the cross sections in e^+e^- annihilation to a fermion pair, it is simplest to begin with the cross sections for polarized initial and final states. Using the same principles for evaluating spinor products as before, it is not difficult to work these out. The general form of the differential cross sections is

$$\begin{aligned}
\frac{d\sigma}{d\cos\theta}(e_L^-e_R^+ \rightarrow f_L\bar{f}_R) &= \frac{\pi\alpha^2}{2s} |s F_{LL}(s)|^2 (1 + \cos\theta)^2 \\
\frac{d\sigma}{d\cos\theta}(e_R^-e_L^+ \rightarrow f_L\bar{f}_R) &= \frac{\pi\alpha^2}{2s} |s F_{RL}(s)|^2 (1 - \cos\theta)^2 \\
\frac{d\sigma}{d\cos\theta}(e_L^-e_R^+ \rightarrow f_R\bar{f}_L) &= \frac{\pi\alpha^2}{2s} |s F_{LR}(s)|^2 (1 - \cos\theta)^2 \\
\frac{d\sigma}{d\cos\theta}(e_R^-e_L^+ \rightarrow f_R\bar{f}_L) &= \frac{\pi\alpha^2}{2s} |s F_{RR}(s)|^2 (1 + \cos\theta)^2.
\end{aligned} \tag{77}$$

The form factors $F_{IJ}(s)$ reflect photon γ - Z interference, with the $p\gamma$ charges Q and the Z charges Q_Z in (22). Using the subscript f to denote the flavor and chirality of the fermion,

$$\begin{aligned}
F_{LL}(s) &= \frac{Q_f}{s} + \frac{(1/2 - s_w^2)(I_f^3 - s_w^2 Q_f)}{s_w c_w} \frac{1}{s - m_Z^2} \\
F_{RL}(s) &= \frac{Q_f}{s} + \frac{(-s_w^2)(-s_w^2 Q_f)}{s_w c_w} \frac{1}{s - m_Z^2} \\
F_{LR}(s) &= \frac{Q_f}{s} + \frac{1/2 - s_w^2)(I_f^3 - s_w^2 Q_f)}{s_w c_w} \frac{1}{s - m_Z^2} \\
F_{RR}(s) &= \frac{Q_f}{s} + \frac{(-s_w^2)(-s_w^2 Q_f)}{s_w c_w} \frac{1}{s - m_Z^2}.
\end{aligned} \tag{78}$$

The total cross sections predicted from these formulae for $e^+e^- \rightarrow$ hadrons, $e^+e^- \rightarrow \mu^+\mu^-$, and $e^+e^- \rightarrow \tau^+\tau^-$ are shown in Fig. 5 and compared to data from the DELPHI experiment at the CERN e^+e^- collider LEP. The resonance at the center of mass energy of 91 GeV is of course the Z boson.

Notice that, for $s > m_Z^2$, we have constructive interference in the LL and RR polarization states and destructive interference for RL and LR. Then in an experiment with unpolarized beams (as in the program of e^+e^- experiments at LEP), the LL and RR modes should dominate and produce a positive forward-backward asymmetry in the angular distribution. This behavior is actually seen in the data. Figure 6 shows the forward-backward asymmetry in $e^+e^- \rightarrow \mu^+\mu^-$ and $e^+e^- \rightarrow \tau^+\tau^-$ measured by the DELPHI experiment at LEP [18]. The solid line is the prediction of the SM.

It is interesting to explore the high-energy limits of the expressions (78). Begin with $F_{RL}(s)$, corresponding to $e_R^-e_L^+ \rightarrow f_L\bar{f}_R$. In the limit $s \gg m_Z^2$ and inserting $Q = I_f^3 + Y$, this becomes

$$F_{RL} \rightarrow \frac{s_w^2 c_w^2 (I_f^3 + Y_f) - s_w^2 I_f^3 + s_w^4 (I_f^3 + Y_f)}{s_w^2 c_w^2 s}$$

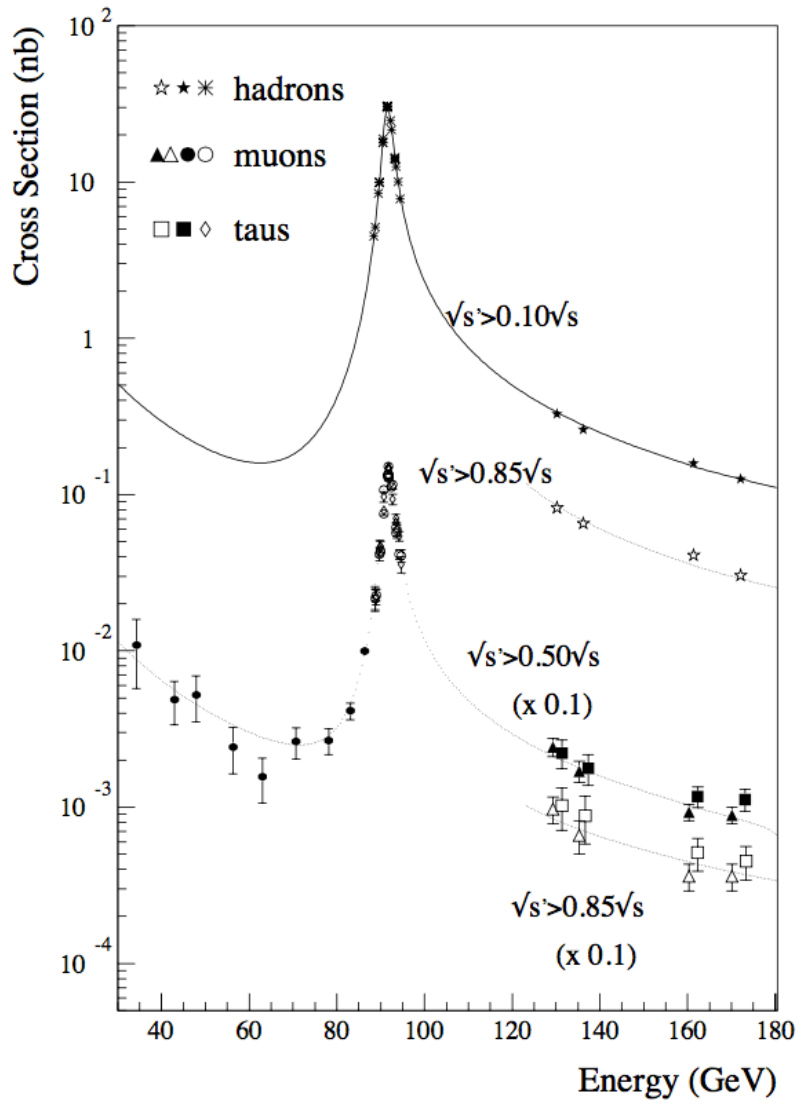


Figure 5: Total cross section for $e^+e^- \rightarrow \text{hadrons}$, $e^+e^- \rightarrow \mu^+\mu^-$, and $e^+e^- \rightarrow \tau^+\tau^-$, as a function of center of mass energy, as measured by the DELPHI experiment at the collider LEP [18]. The continuous lines are the predictions of the SM.

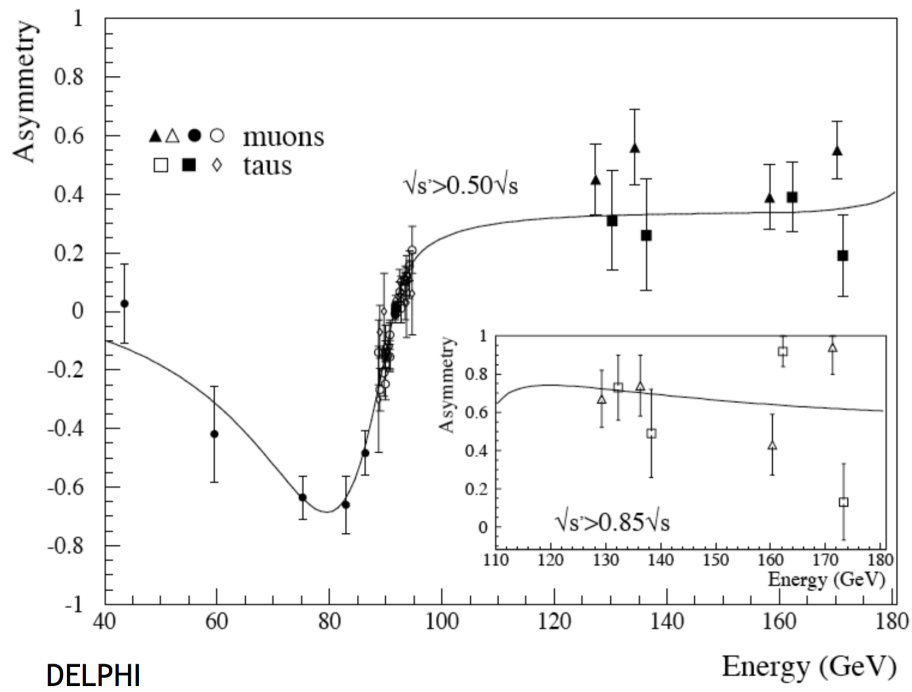


Figure 6: Forward-backward asymmetry in the reactions $e^+e^- \rightarrow \mu^+\mu^-$ and $e^+e^- \rightarrow \tau^+\tau^-$, as a function of center of mass energy, as measured by the DELPHI experiment at the collider LEP [18]. .

$$\begin{aligned}
&= \frac{s_w^2 Y_f}{s_w^2 c_w^2 s} \\
&= \frac{1}{e^2} \left(\frac{g'^2 Y_{eR} Y_f}{s} \right). \tag{79}
\end{aligned}$$

The expression in parentheses is exactly the amplitude for s -channel exchange of the $U(1)$ boson B in the situation in which the original $SU(2) \times U(1)$ symmetry was not spontaneously broken. So we see that the full gauge symmetry is restored at high energies.

Here is the same analysis for $F_{LL}(s)$:

$$\begin{aligned}
F_{RL} &\rightarrow \frac{s_w^2 c_w^2 (I_f^3 + Y_f) + (1/2 - s_w^2)(I_f^3 - s_w^2 (I_f^3 + Y_f))}{s_w^2 c_w^2 s} \\
&= \frac{(1/2) c_w^2 I_f^3 + (1/2) s_w^2 Y_f}{s_w^2 c_w^2 s} \\
&= \frac{1}{e^2} \left(\frac{g^2 I_{eL}^3 I_f^3}{s} + \frac{g'^2 Y_{eR} Y_f}{s} \right). \tag{80}
\end{aligned}$$

Now the result is a coherent sum of A^3 and B exchanges in the s -channel. Again, this is the result expected in a theory of unbroken $SU(2) \times U(1)$.

It is interesting to compare the values of ratios and asymmetries measured at LEP to the asymptotic values predicted by unbroken $SU(2) \times U(1)$. This comparison is shown in Fig. 7 from a compilation of preliminary LEP results [19]; final LEP results on 2-fermion processes are collected in [20]. The arrows at the extreme right show the values for restored $SU(2) \times U(1)$. The calculation of R_b involves a top quark box diagram that does not yet reach its asymptotic limit at 200 GeV. It is remarkable that, for all other observables, the LEP measurements at center of mass energies of 200 GeV are already close to the asymptotic values predicted at high energy.

4 Precision electroweak measurements at the Z resonance

It is possible to test the SM theory of the weak interactions more incisively by focusing more tightly on the properties of the Z boson. The Z boson appears as a resonance in e^+e^- annihilation. In the 1990's, the accelerators LEP at CERN and SLC at SLAC tuned their energies to the Z boson resonance to produce large numbers of Z bosons at rest in the lab, in an appropriate setting for precision measurements. In this section, I review the results of these precision measurements, which continue to provide important constraints on the SM and its generalizations.

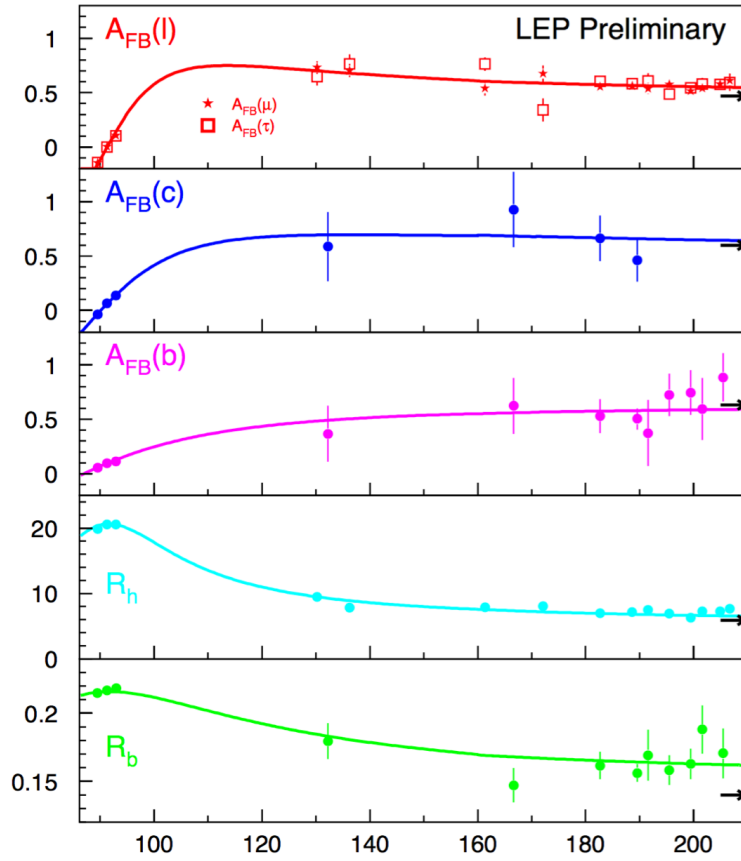


Figure 7: Compilation of preliminary LEP measurements of the forward-backward asymmetry in lepton, c , and b pair production, the hadron to lepton ratio R_h and the b to all hadron ratio R_b [19]. The solid curves show the SM prediction. The arrows at the right are the predictions of unbroken $SU(2) \times U(1)$.

4.1 Properties of the Z boson in the Standard Model

My discussion will be based on the leading order matrix elements for Z decay to $f_L\bar{f}_R$ and $f_R\bar{f}_L$. It is straightforward to work these out based on the spinor matrix elements computed in Section 2.2. The leading order matrix element for Z decay to $f_L\bar{f}_R$ is

$$\mathcal{M}(Z \rightarrow f_L\bar{f}_R) = i\frac{g}{c_w}Q_{Zf}u_L^\dagger\bar{\sigma}^\mu v_R\epsilon_{Z\mu}, \quad (81)$$

with

$$Q_Z = I^3 - s_w^2Q, \quad (82)$$

as in (22). Using (36) for the spinor matrix element, this becomes

$$\mathcal{M} = i\frac{g}{c_w}\sqrt{2}m_Z\epsilon_-^* \cdot \epsilon_Z. \quad (83)$$

Square this and average over the direction of the fermion, or, equivalently, average over three orthogonal directions for the Z polarization vector. The result is

$$\langle |\mathcal{M}|^2 \rangle = \frac{2}{3}\frac{g^2}{c_w^2}Q_{Zf}^2m_Z^2. \quad (84)$$

Then, since

$$\Gamma(Z \rightarrow f_L\bar{f}_R) = \frac{1}{2m_Z}\frac{1}{8\pi}\langle |\mathcal{M}|^2 \rangle, \quad (85)$$

we find

$$\Gamma(Z \rightarrow f_L\bar{f}_R) = \frac{\alpha_w m_Z}{6c_w^2}Q_{Zf}^2N_f, \quad (86)$$

where

$$\alpha_w = \frac{g^2}{4\pi} \quad (87)$$

and

$$N_f = \begin{cases} 1 & \text{lepton} \\ 3(1 + \alpha_s/\pi + \dots) & \text{quark} \end{cases} \quad (88)$$

accounts the number of color states and the QCD correction. The same formula holds for the Z width to $f_R\bar{f}_L$.

To evaluate this formula, we need values of the weak interaction coupling constants. The electromagnetic coupling α is famously close to $1/137$. However, in quantum field theory, α is a running coupling constant that becomes larger at small distant scales. At a scale of $Q = m_Z$, $\alpha(Q) = 1/129$. Later in the lecture, I will defend a value of the weak mixing angle

$$s_w^2 = 0.231. \quad (89)$$

Then the $SU(2)$ and $U(1)$ couplings take the values

$$\alpha_w = \frac{g^2}{4\pi} = \frac{1}{29.8} \quad \alpha' = \frac{g'^2}{4\pi} = \frac{1}{99.1} \quad (90)$$

It is interesting to compare these values to other fundamental SM couplings taken at the same scale $Q = m_Z$,

$$\alpha_s = \frac{1}{8.5} \quad \alpha_t = \frac{y_t^2}{4\pi} = \frac{1}{12.7} . \quad (91)$$

All of these SM couplings are roughly of the same order of magnitude.

Using (89) or (90), we can tabulate the values of the Z couplings to left- and right-handed fermions,

species	Q_{ZL}	Q_{ZR}	S_f	A_f
ν	$+\frac{1}{2}$	-	0.250	1.00
e	$-\frac{1}{2} + s_w^2$	$+s_W^2$	0.126	0.15
u	$+\frac{1}{2} - \frac{2}{3}s_w^2$	$-\frac{2}{3}s_W^2$	0.143	0.67
d	$-\frac{1}{2} + \frac{1}{3}s_w^2$	$+\frac{1}{3}s_W^2$	0.185	0.94

(92)

In this table, the quantities evaluated numerically are

$$S_f = Q_{ZL}^2 + Q_{ZR}^2 \quad A_f = \frac{Q_{ZL}^2 - Q_{ZR}^2}{Q_{ZL}^2 + Q_{ZR}^2} . \quad (93)$$

The quantity S_f gives the contribution of the species f to the total decay rate of the Z boson. The quantity A_f gives the polarization asymmetry for f , that is, the preponderance of f_L over f_R , in Z decays,

4.2 Measurements of the Z properties

It is possible to measure many of the total rates and polarization asymmetries for individual species in a very direct way through experiments on the Z resonance. This subject is reviewed in great detail in the report [22]. Values of the Z observables given below are taken from this reference unless it is stated otherwise.

The S_f are tested by the measurement of the Z resonance width and its branching ratios. Using (86), we find for the total width of the Z

$$\Gamma_Z = \frac{\alpha_w m_Z}{6c_w^2} \left[3 \cdot 0.25 + 3 \cdot 0.126 + 2 \cdot (3.1) \cdot 0.144 + 3 \cdot (3.1) \cdot 0.185 \right] . \quad (94)$$

The four terms denote the contributions from 3 generations of ν , e , u , and d , minus the top quark, which is too heavy to appear in Z decays. The numerical prediction is

$$\Gamma_Z = 2.49 \text{ GeV} \quad (95)$$

The separate terms in (94) give the branching ratios

$$\begin{aligned} BR(\nu_e \bar{\nu}_e) &= 6.7\% & BR(e^+ e^-) &= 3.3\% \\ BR(u \bar{u}) &= 11.9\% & BR(d \bar{d}) &= 15.3\% \end{aligned} \quad (96)$$

The measured value of the total width, whose extraction I will discuss in a moment, is

$$\Gamma_Z = 2.4952 \pm 0.0023 \text{ GeV} . \quad (97)$$

This is in very good agreement with (95), with accuracy such that a valid comparison with theory requires the inclusion of electroweak radiative corrections, with typically are of order 1%. The measurements of branching ratios and polarization asymmetry that I review later in this section are also of sub-% accuracy. At the end of this section, I will present a more complete comparison of theory and experiment, including radiative corrections to the theoretical predictions.

To begin our review of the experimental measurements, we should discuss the measurement of the Z resonance mass and width in more detail. Ideally, the Z is a Breit-Wigner resonance, with cross section shape

$$\sigma \sim \left| \frac{1}{s - m_Z^2 + im_Z \Gamma_Z} \right|^2 . \quad (98)$$

At first sight, it seems that we can simply read off the Z mass as the maximum of the resonance and the width as the observed width at half maximum. However, we must take into account that the resonance is distorted by initial-state radiation. As the electron and positron collide and annihilate into a Z , they can radiate hard collinear photons. Because of this, the resonance is pushed over to higher energies, an effect that shifts the peak and creates a long tail on above the resonance. The magnitude of the photon radiation is given by the parameter

$$\beta = \frac{2\alpha}{\pi} \left(\log \frac{s}{m_e^2} - 1 \right) = 0.108 \quad \text{at } s = m_Z^2 \quad (99)$$

In addition, since the Z is narrow, the effect of this radiation is magnified, since even a relatively soft photon can push the center of mass energy off of the resonance. The size of the correction can be roughly estimated as

$$-\beta \cdot \log \frac{m_Z}{\Gamma_Z} = 40\% . \quad (100)$$

To make a proper accounting of this effect, we need to include arbitrary numbers of radiated collinear photons. Fadin and Kuraev introduced the idea of viewing the radiated photons and the final annihilating electron as partons in the electron in the same way that quarks and gluons are treated as partons in the proton [21]. For the proton, the parton distribution is generated by non-perturbative effects, but for the electron the parton distributions are generated only by QED, so that they can be calculated as a function of α . The result for the parton distribution of the electron in the electron, to order α , is

$$f_e(z, s) = \frac{\beta}{2}(1-z)^{\beta/2-1}\left(1 + \frac{3}{8}\beta\right) - \frac{1}{4}\beta(1+z) + \dots, \quad (101)$$

where z is the momentum fraction of the original electron carried into the e^+e^- annihilation to a Z boson. The cross section for producing a Z boson would then be a convolution of the Breit-Wigner cross section (98) with the parton distribution (101) and the corresponding distribution for the positron. For the LEP experiments, this theory was extended to include two orders of subleading logarithms and finite corrections of order α^2 [23].

The experimental aspects of the measurement of the Z resonance lineshape were also very challenging; see Section 2.2 of [22]. Careful control was needed for point-to-point normalization errors across the Z resonance. The absolute energy of the LEP ring was calibrated using resonant depolarization of a single electron beam and then corrected for two-beam effects. This calibration was found to depend on the season and the time of day. Some contributing effects were the changes in the size of the LEP tunnel due to the annual change in the water level in Lake Geneva and current surges in the LEP magnets due to the passage to the TGV leaving Geneva for Paris.

Some final results for the resonance line shape measurement are shown in Figs. 8, 9. The first of these figures shows the measurements by the OPAL experiment over the resonance and the detailed agreement of the shape between theory and experiment [24]. The second shows the combination of the resonance height and width measurements from the four LEP experiments ALEPH, DELPHI, L3, and OPAL [22]. In this figure, the lower curve is the radiatively corrected result; the higher curve is the inferred Breit-Wigner distribution excluding the effects of radiative corrections.

The measurement of branching ratios is more straightforward. It is necessary only to collect Z decay events and sort them into categories. The various types of leptonic and hadronic decay modes have very different, characteristic forms. Typical events are shown in Fig. 10 for hadronic, e^+e^- , $\mu^+\mu^-$, and $\tau^+\tau^-$ decays [25]. The major backgrounds are from Bhabha scattering and 2-photon events. These do not resemble Z decay events and are rather straightforwardly separated. Nonresonant e^+e^- annihilations are also a small effect, generally providing backgrounds at only the level of parts per mil. An exception is the Z decay to $\tau^+\tau^-$, which can be faked by hadronic e^+e^- annihilations with radiation to provide a background level of a few

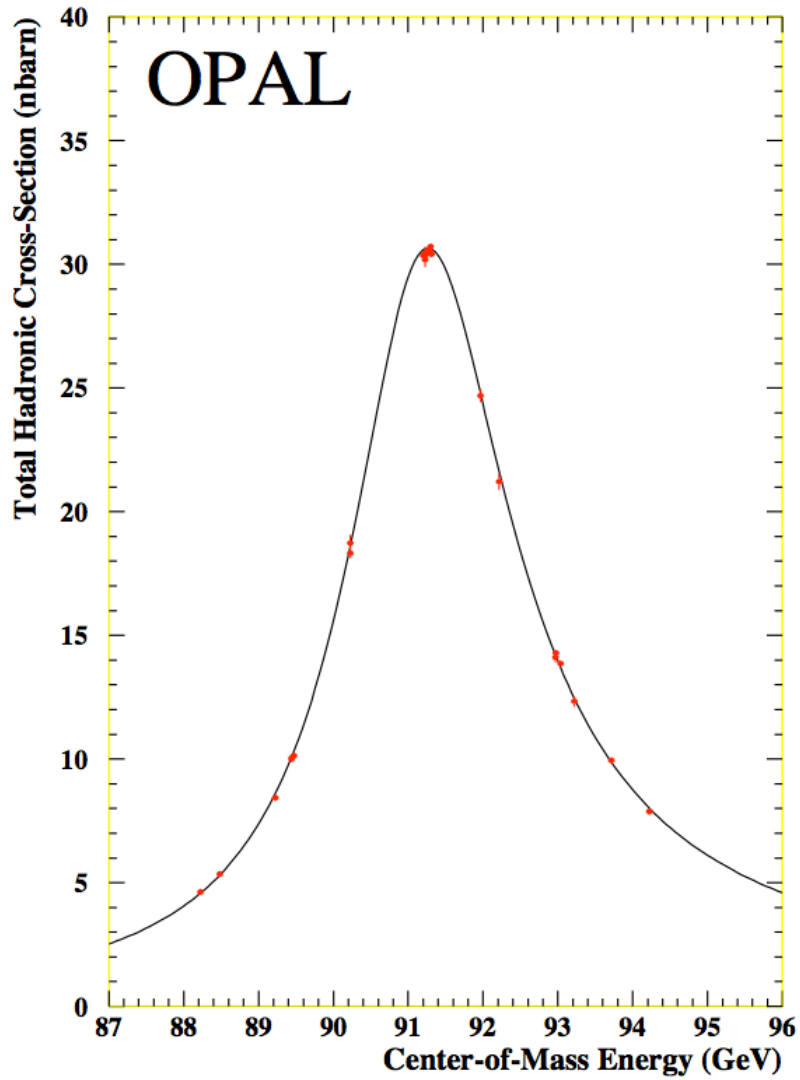


Figure 8: Resonance line shape of the Z in e^+e^- annihilation, as measured by the OPAL experiment [24].

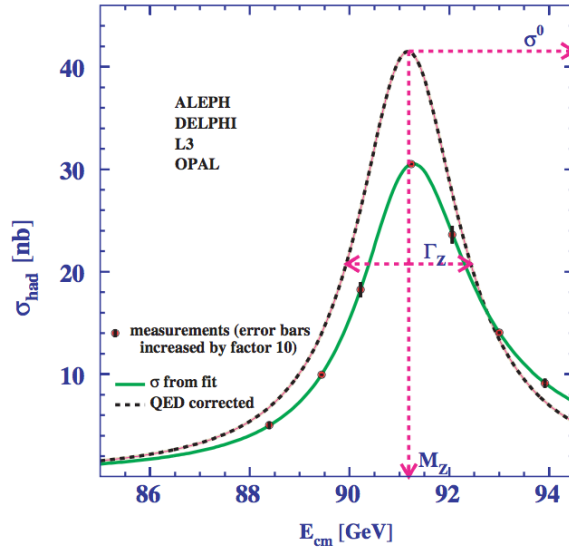


Figure 9: Resonance line shape of the Z in e^+e^- annihilation, as measured by the four LEP experiments, from [22]. The dotted curve shows the zeroth-order resonance line shape of the Z resonance. The solid line shows the Standard Model prediction including initial-state radiative corrections.

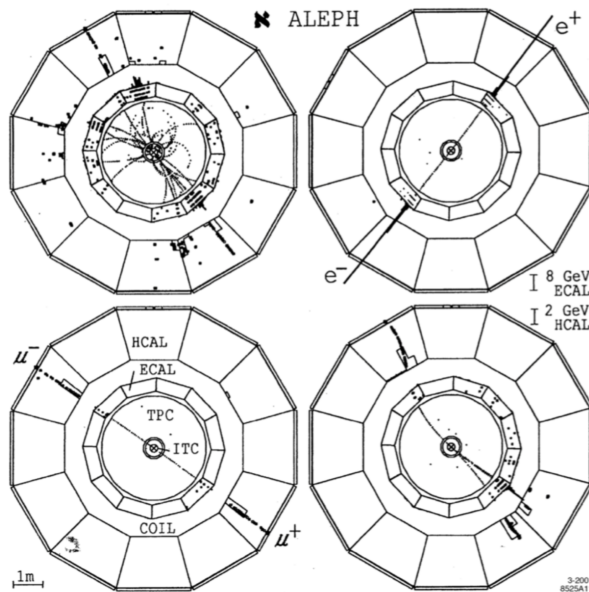


Figure 10: Typical $e^+e^- \rightarrow Z$ events corresponding to the Z decays to hadrons, to e^+e^- , to $\mu^+\mu^-$, and to $\tau^+\tau^-$, from [25].

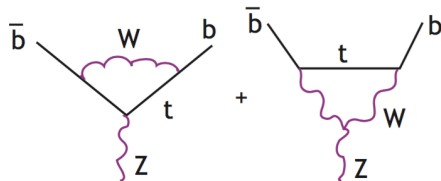


Figure 11: Diagrams containing the top quark which give a relatively large correction to the partial width for $Z \rightarrow b\bar{b}$.

percent. Still, these high signal to background ratios are completely different from the situation at the LHC and enable measurements of very high precision.

Two particular branching ratios merit special attention. First, consider Z decays to invisible final states. The SM includes Z decays to 3 species of neutrino, with a total branching ratio of 20%. Even though these decays are not seen in the detector, the presence of invisible final states affects the resonance lineshape by increasing the Z width and decreasing the Z peak height to visible modes such as hadrons. Measurement of the resonance parameters then effectively gives the number of light neutrinos into which the Z can decay. The result is

$$n_\nu = 2.9840 \pm 0.0082 , \quad (102)$$

strongly constraining extra neutrinos or more exotic neutral particles.

Second, the Z branching ratio to b quarks is of special interest, for two reasons. First, the b belongs to the same $SU(2) \times U(1)$ multiplet as the top quark, and, even in the SM, there is a relatively large radiative correction due to top quark loops, from the diagrams shown in Fig. 11. These produce

$$Q_{ZbL} = -\left(\frac{1}{2} - \frac{1}{3}s_w^2 - \frac{\alpha}{16\pi s_w^2} \frac{m_t^2}{m_W^2}\right) , \quad (103)$$

a shift of about -2% . More generally, the b is a third-generation particle that might have a nontrivial coupling to new, heavier, particles.

An observable that specifically tracks this effect is

$$R_b = \frac{\Gamma(Z \rightarrow b\bar{b})}{\Gamma(Z \rightarrow \text{hadrons})} . \quad (104)$$

At leading order, we predict $R_b = 0.22$, but in the full SM this value should be reduced according to (103). Z decays to $b\bar{b}$ could be identified by vertex tags. The SLD detector at SLAC included a pixel vertex detector capable of separating decays to b and c by vertex mass and by the presence of tertiary charm decay vertices in b jets.

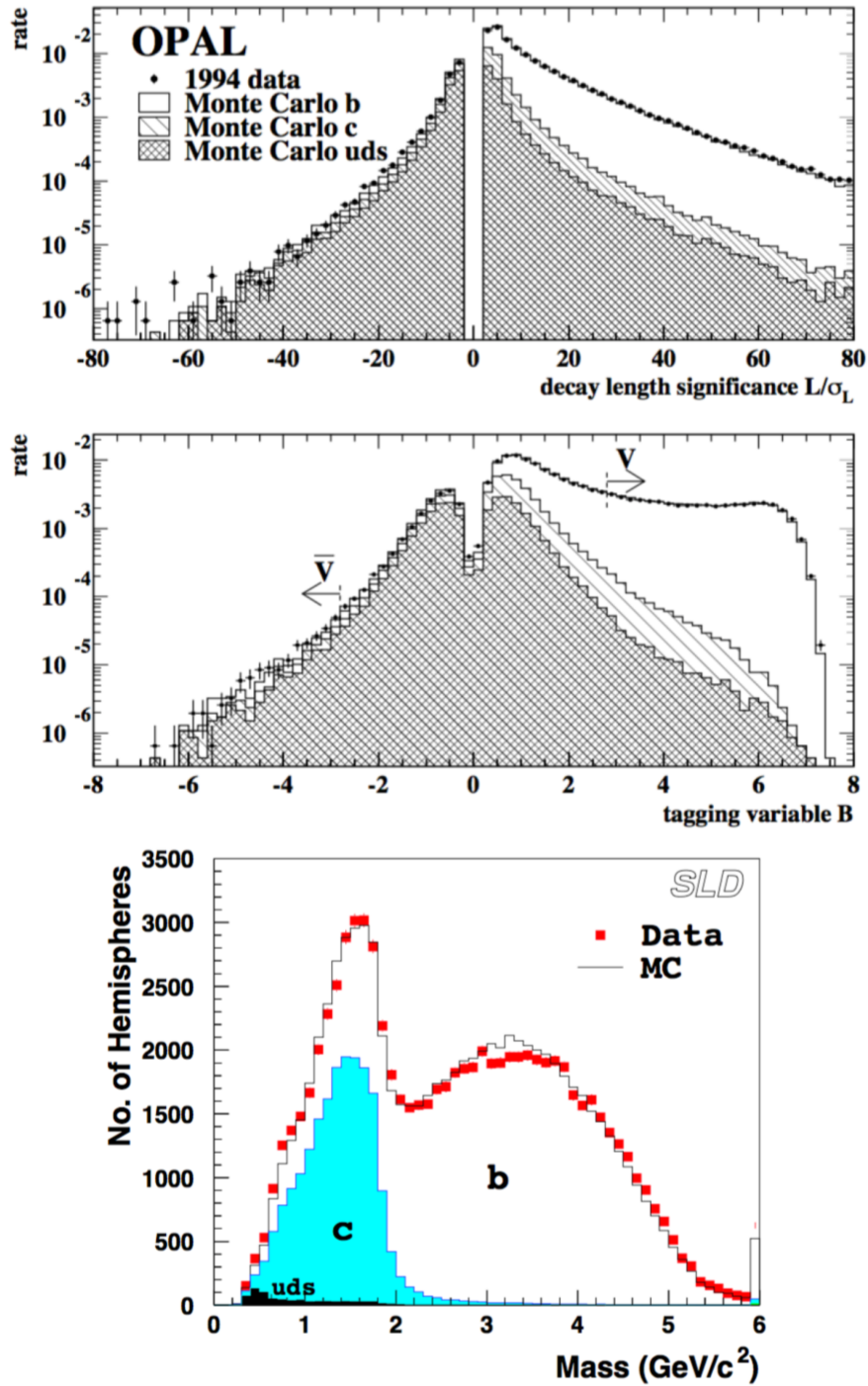


Figure 12: Measurements of the b and c branching fractions of the Z . Top: Distributions in decay length significance and the b quark tagging variable, from the OPAL experiment, showing the relative contributions of light quarks, c , and b , from [26]. Right: Vertex mass distribution from the SLD experiment, showing the contributions from c and b meson decays, from [27].

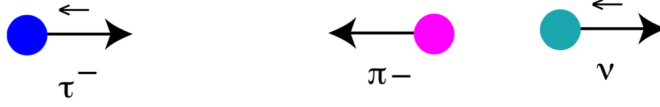


Figure 13: Kinematics of $\tau \rightarrow \nu\pi$ decay.

Fig. 12(a) shows the signal and background separation in the OPAL experiment [26]. Fig. 12(b) shows a corresponding result from SLD, in which the observed vertex mass was used to discriminate between the c and b contributions [27]. The final LEP and SLC results gave

$$\begin{aligned} R_b &= 0.21629 \pm 0.00066 \\ R_c &= 0.1721 \pm 0.0030, \end{aligned} \quad (105)$$

confirming the shift predicted by (103) and demonstrating consistency with the SM also for $Z \rightarrow c\bar{c}$.

While the total rates for the Z decay to the various species have similar values, the asymmetries listed in (92) vary over a wide range, from 15% for the charged leptons to almost maximal for the d -type quarks. The SM predicts these disparate values from a common value of s_w^2 .

There are three very different methods to measure the lepton asymmetries A_e . First, the A_e can be found from the forward-backward asymmetry for $e^+e^- \rightarrow f\bar{f}$ at the Z . Second, A_e can be determined from the final-state polarization effects in the decays of $\tau^+\tau^-$ produced at the Z . Finally, A_e can be measured directly from the rate for Z production from polarized electron beams.

For unpolarized beams, the angular distribution for $e^+e^- \rightarrow f\bar{f}$ can be found from (77). On the Z resonance, the distribution takes the form

$$\begin{aligned} \frac{d\sigma}{d\cos\theta} &= \left(\frac{1+A_e}{2}\right)\left(\frac{1+A_f}{2}\right)(1+\cos\theta)^2 + \left(\frac{1-A_e}{2}\right)\left(\frac{1+A_f}{2}\right)(1-\cos\theta)^2 \\ &\quad + \left(\frac{1+A_e}{2}\right)\left(\frac{1-A_f}{2}\right)(1-\cos\theta)^2 + \left(\frac{1-A_e}{2}\right)\left(\frac{1-A_f}{2}\right)(1+\cos\theta)^2. \end{aligned} \quad (106)$$

The forward-backward asymmetry predicted by this expression is

$$A_{FB} = \frac{3}{4}A_eA_f \quad (107)$$

Especially for b quarks, which have an almost maximal asymmetry, the dependence of this quantity on s_w^2 is mainly through A_e .

The value of A_e determines the polarization of τ leptons produced in Z decays, and this polarization becomes visible through the $V-A$ structure of the τ decays.

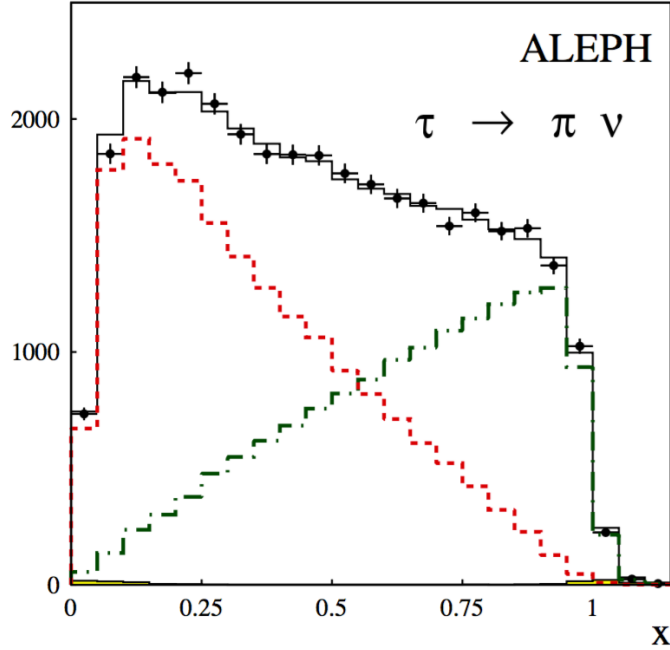


Figure 14: Pion energy spectrum in $\tau \rightarrow \nu\pi$ decays at the Z resonance, from [28]. The ordinate $x = 2E_\pi/m_Z$. The separate contributions from τ_L and τ_R decays are indicated.

The easiest case to understand is the decay $\tau^- \rightarrow \nu_\tau \pi^-$. Since the neutrino is always left-handed and the pion has zero spin, a τ^- at rest with $S^3 = -\frac{1}{2}$ will decay to a forward neutrino and a backward π^- , as shown in Fig. 13. When the τ^- is boosted, a left-handed τ will decay to a high-energy neutrino and a slow pion. A right-handed τ will decay to a low-energy neutrino and a fast pion. More generally, if x is the fraction of the τ momentum carried by the π^- ,

$$\tau_L : \frac{d\Gamma}{dx} \sim (1-x) \quad \tau_R : \frac{d\Gamma}{dx} \sim x. \quad (108)$$

Similar asymmetries appear in the other τ decay modes. Fig. 14 shows the distributions measured by the ALEPH experiment for $\tau \rightarrow \pi\nu$, compared to the expected distributions from τ_L and τ_R . The 15% asymmetry is apparent. The SM also predicts a correlation between polarization and $\cos\theta$ that can be used to improve the s_w^2 measurement.

The SLC produced $e^+e^- \rightarrow Z$ events using linear acceleration of the electrons. This technique allowed the preservation of electron polarization from the source to the collisions. The experiment was conducted by flipping the the electron polarization in each bunch randomly, and measuring the correlation between the polarization orientation and the total Z production rate—measured 4 km downstream of the

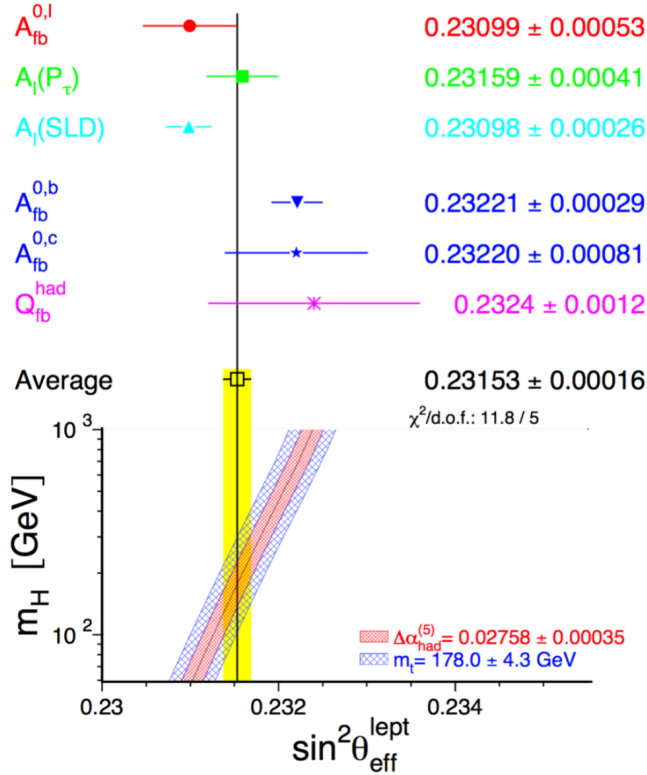


Figure 15: Summary of A_ℓ measurements at the Z resonance from different observables, from [22].

source. This gave a direct measurement [29]

$$A_e = 0.1516 \pm 0.0021 \quad (109)$$

Figure 15 shows the summary of the various determinations of s_w^2 from the leptonic asymmetries [22]. The measurements are statistically consistent and lead to a very precise value.

The prediction that the b asymmetry is close to maximal implies that the angular distribution of $e^+e^- \rightarrow b\bar{b}$ at the Z should show a large dependence on beam polarization. The distribution should be close to $(1 + \cos\theta)^2$ for a left-handed polarized beam and close to $(1 - \cos\theta)^2$ for a right-handed polarized beam. The distributions measured by the SLD experiment at the SLC for left- and right-handed beams are shown in Fig. 16. Allowing for the expected confusion in separating b and \bar{b} jets, the results are consistent with a high b polarization in Z decays. The difference in normalization of the two distributions reflects the 15% asymmetry in the production cross section.

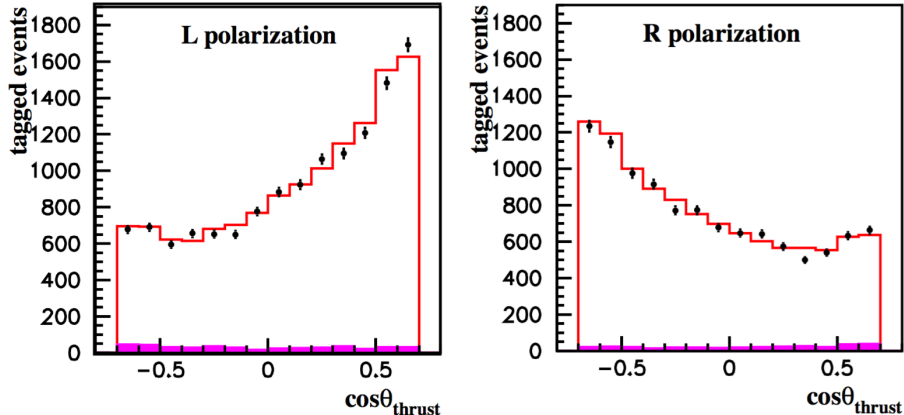


Figure 16: Angular distribution of $e^+e^- \rightarrow Z \rightarrow b\bar{b}$ events measured by the SLD experiment for left- and right-handed polarized beams, from [30].

Figure 17 shows a summary of the precision measurements of the properties of the Z boson [22]. The measured values listed in the first column are compared to the values from the best fit to the SM, including one-loop radiative corrections. The bars show the deviations from the SM prediction, in units of the σ of the measurement. This is an impressive confirmation of the $SU(2) \times U(1)$ weak interaction model.

4.3 Constraints on oblique radiative corrections

From the excellent agreement of the Z measurements with the SM, it is possible to put general constraints on possible new particles coupling to the weak interactions.

To explain this, we should first discuss the properties of one-loop corrections to the $SU(2) \times U(1)$ predictions in more detail. The SM contains a large number of parameters. However, the predictions discussed in this Section depend, at the three level, only on the three parameters

$$g, g', v. \quad (110)$$

The loop corrections will include divergences, including quadratically divergent corrections to v^2 . However, because the $SU(2) \times U(1)$ theory is renormalizable, once these three parameters are fixed, all of the 1-loop corrections must be finite. Then each specific reaction acquires a finite prediction, which is a testable consequence of the SM.

Different schemes are used to fix the three underlying divergent amplitudes. Each gives different expressions for the measurable cross sections. Three common schemes are

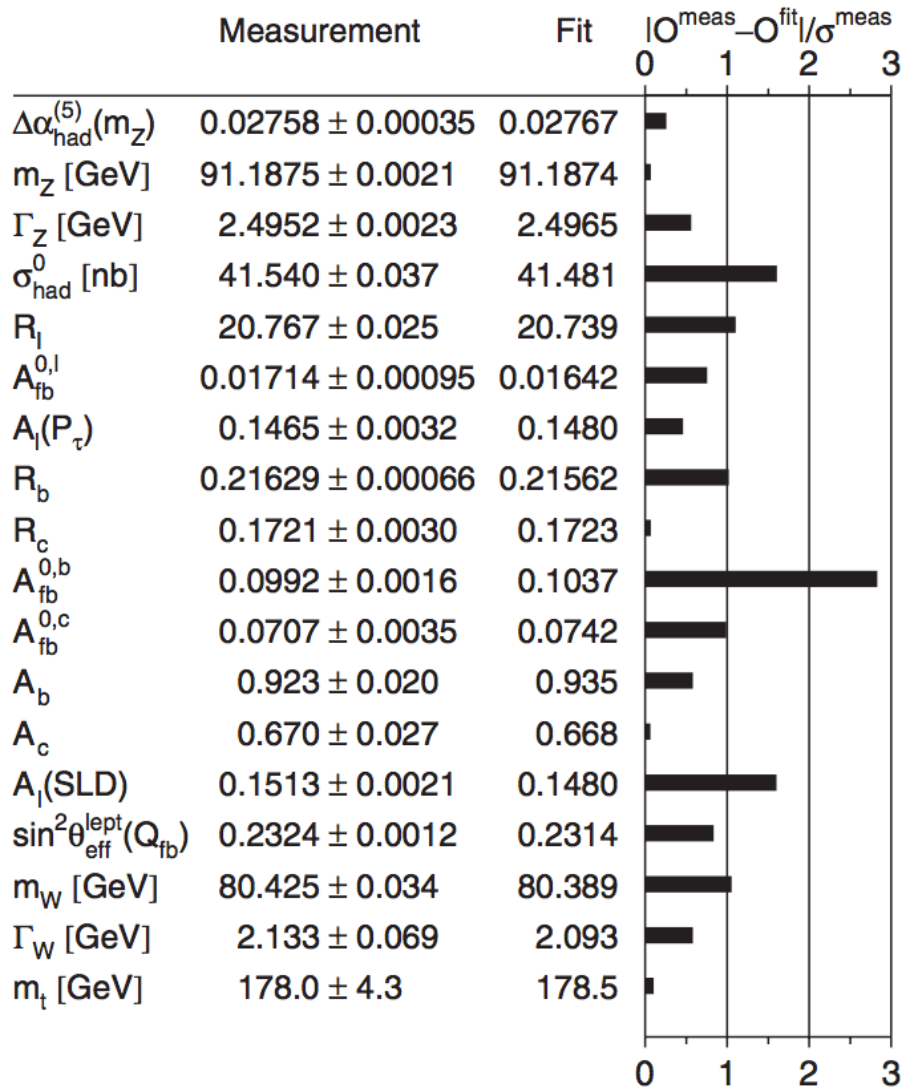


Figure 17: Summary of precision electroweak measurements at the Z resonance, from [22].

- applying \overline{MS} subtraction, as in QCD
- fixing $\alpha(m_Z)$, m_Z , m_W to their measured values (Marciano-Sirlin scheme) [32]
- fixing $\alpha(m_Z)$, m_Z , G_F to their measured values (on shell Z scheme)

In the \overline{MS} scheme, used by the Particle Data Group, the \overline{MS} parameters g , g' , and v are unphysical but can be defined as the values that give the best fit to the corpus of SM measurements [31].

The various schemes for renormalizing the $SU(2) \times U(1)$ model lead to different definitions of s_w^2 that are found in the literature. In the Marciano-Sirlin scheme, we define θ_w by

$$c_w \equiv m_W/m_Z . \quad (111)$$

This leads to

$$s_w^2 = 0.22290 \pm 0.00008 . \quad (112)$$

We will see in Section 4 that the relation (111) is often needed to insure the correct behavior in high-energy reactions of W and Z , so it is useful that this relation is insured at the tree level. Thus, the Marciano-Sirlin definition of θ_w is the most common one used in event generators for LHC. However, one should note that the value (112) is significantly different from the value (89) that best represents the sizes of the Z cross sections and asymmetries.

In the on-shell Z scheme, θ_w is defined by

$$\sin^2 2\theta_w = (2c_w s_w)^2 \equiv \frac{4\pi\alpha(m_Z)}{\sqrt{2}G_F m_Z^2} , \quad (113)$$

leading to

$$s_w^2 = 0.231079 \pm 0.000036 . \quad (114)$$

This definition gives at tree level a value that is much closer to (89). All three values of $\sin^2 \theta_w$ lead to the same predictions for the relation of observables to observables after the (scheme-dependent) finite 1-loop corrections are included.

One particular class of radiative corrections is especially simple to analyze. If new particles have no direct coupling to light fermions, they can appear in radiative corrections to the Z observables only through vector boson vacuum polarization amplitudes. Effects of this type are called *oblique* radiative corrections. These effects can be analyzed in a quite general way.

There are four electroweak vacuum polarization amplitudes $\Pi_{AB}(q^2)$. I will notate them as shown in Fig. 18. The subscripts 1, 3 refer to the weak isospin currents $j^{\mu a}$, $a = 1, 3$; the subscript Q refers to the electromagnetic current. The Z vacuum polarizations are found from these elements using (82). If the particles in the loop

Figure 18: Vector boson vacuum polarization diagrams..

have large masses M , we can Taylor expand the vacuum polarization amplitudes in powers of q^2/M^2 . Up to order q^2/M^2 , we find

$$\begin{aligned}
\Pi_{QQ}(q^2) &= Aq^2 + \dots \\
\Pi_{3Q}(q^2) &= Bq^2 + \dots \\
\Pi_{33}(q^2) &= C + Dq^2 + \dots \\
\Pi_{11}(q^2) &= E + Fq^2 + \dots
\end{aligned} \tag{115}$$

There are six constants in this set of formulae. Three of them are fixed by the renormalizations of g , g' , v . This leaves 3 finite combinations of vacuum polarization amplitudes will be predicted in any new physics model. These combinations are canonically defined as [33]

$$\begin{aligned}
S &= \frac{16\pi}{m_Z^2} \left[\Pi_{33}(m_Z^2) - \Pi_{33}(0) - \Pi_{3Q}(m_Z^2) \right] \\
T &= \frac{4\pi}{s_w^2 m_W^2} \left[\Pi_{11}(0) - \Pi_{33}(0) \right] \\
U &= \frac{16\pi}{m_Z^2} \left[\Pi_{11}(m_Z^2) - \Pi_{11}(0) - \Pi_{33}(m_Z^2) + \Pi_{33}(0) \right]
\end{aligned} \tag{116}$$

In [33], the amplitudes appearing in (116) are the new physics contributions only, but other analyses, for example, [31], use different conventions. The three parameters in (116) have clear physical interpretations. T parametrizes the size of weak isospin violating corrections to the relation $m_W = m_Z c_w$. S parametrizes the q^2/M^2 corrections. U requires both effects and is predicted to be very small in most new physics models.

The leading oblique corrections to electroweak observables can then be expressed as linear shifts proportional to S and T . For example,

$$\frac{m_W^2}{m_Z^2} - c_0^2 = \frac{\alpha c_w^2}{c_w^2 - s_w^2} \left(-\frac{1}{2}S + c_w^2 T \right)$$

$$s_*^2 - s_0^2 = \frac{\alpha}{c_w^2 - s_w^2} \left(-\frac{1}{2} \frac{1}{4} S - s_w^2 c_w^2 T \right), \quad (117)$$

where s_0, c_0 are the values of s_w and c_w in the on-shell Z scheme and s_* is the value of s_w used to evaluate the Z asymmetries A_f . By fitting to the formulae such as (117), we can obtain general constraints that can be applied to a large class of new physics models.

Some guidance about the expected sizes of S and T is given by the result for one new heavy electroweak doublet,

$$S = \frac{1}{6\pi} \quad T = \frac{|m_U^2 - m_D^2|}{m_Z^2}. \quad (118)$$

A complete heavy fourth generation gives $S = 0.2$. The effects of the SM top quark and Higgs boson can also be expressed approximately in the S, T framework,

$$\begin{aligned} \text{top :} \quad & S = \frac{1}{6\pi} \log \frac{m_t^2}{m_Z^2} & T = \frac{3}{16\pi s_w^2 c_w^2} \frac{m_t^2}{m_Z^2} \\ \text{Higgs :} \quad & S = \frac{1}{12\pi} \log \frac{m_h^2}{m_Z^2} & T = -\frac{3}{16\pi c_w^2} \log \frac{m_h^2}{m_Z^2} \end{aligned} \quad (119)$$

The appearance of corrections proportional to m_t^2/m_Z^2 , which we have already seen in (103), will be explained in Section 5.

Figure 19 shows the progress of the S, T fit with our improved understanding of the SM. Figure 19(a) reflects the situation in 1991, before the discovery of the top quark [33]. The two vertical lines to the left are predictions of the SM with a varying top quark mass. Values of m_t in the range of 170–180 GeV are highly favored by the precision electroweak data. The measurement of S , even without the value of m_t , strongly constrained the “technicolor” models of electroweak symmetry breaking. (I will describe these models at the end of Section 7.2.) Figure 19(b) shows the S, T fit in 2008. The solid curve shows the predictions of the SM with a variable Higgs boson mass. Values of the Higgs mass close to 100 GeV are strongly favored. Figure 19(c) shows the current S, T fit [34]. The fit is in good agreement with the SM with the now-measured values of m_t and m_h . It also is in substantial tension with the presence of a fourth generation of quarks and leptons.

5 The Goldstone Boson Equivalence Theorem

In this section, I will describe the properties of the weak interactions at energies much greater than m_W and m_Z . Some new conceptual issues appear here. These affect the energy-dependence of W and Z boson reactions at high energy and the

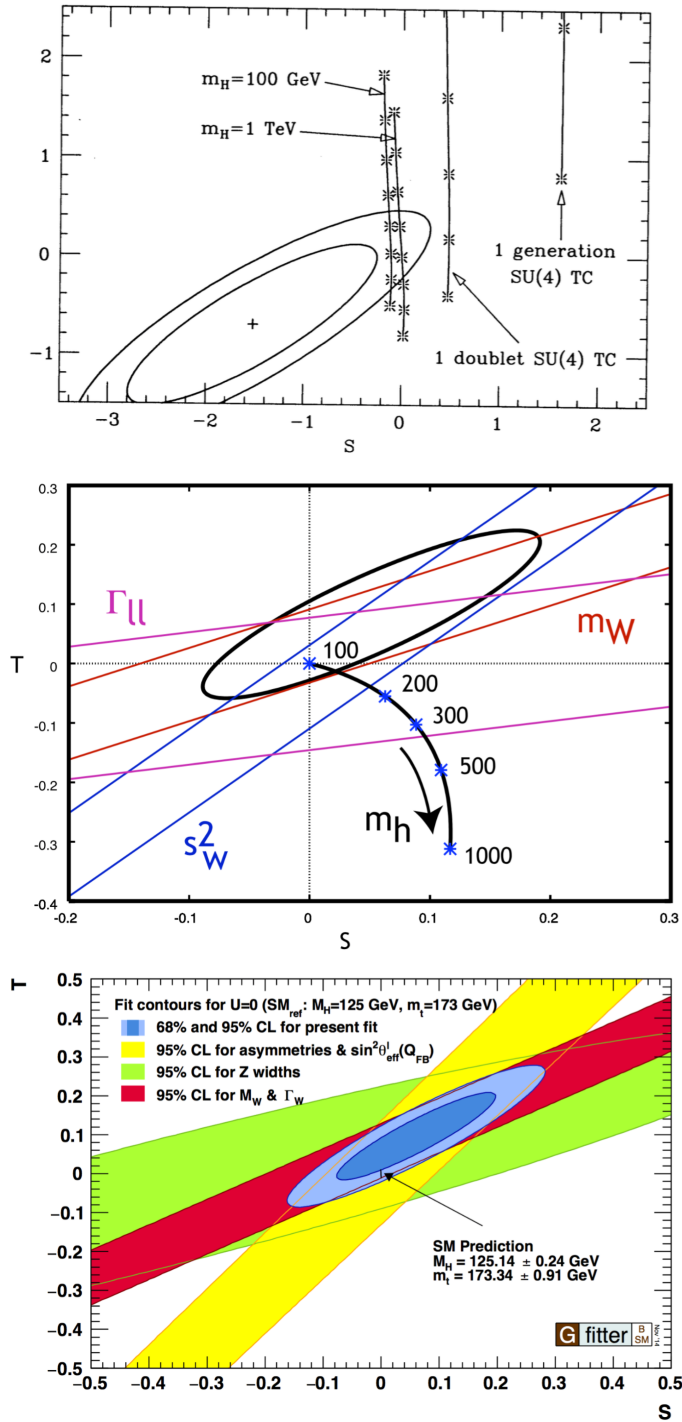


Figure 19: Allowed domain for the S, T parameters in three different eras: in 1991, before the discovery of the top quark [33]; in 2008, before the discovery of the Higgs boson; today [34].

parametrization of possible effects of new physics. I will introduce a way of thinking that can be used as a skeleton key for understanding these issues, called the Goldstone Boson Equivalence Theorem.

5.1 Questions about W and Z bosons at high energy

To begin this discussion, I will raise a question, one that turns out to be one of the more difficult questions to answer about spontaneously broken gauge theories.

In its rest frame, with $p^\mu = (m, 0, 0, 0)^\mu$, a massive vector boson has 3 polarization states, corresponding to the 3 orthogonal spacelike vectors

$$\begin{aligned}\epsilon_+^\mu &= \frac{1}{\sqrt{2}}(0, 1, +i, 0)^\mu \\ \epsilon_0^\mu &= (0, 0, 0, 1)^\mu \\ \epsilon_-^\mu &= \frac{1}{\sqrt{2}}(0, 1, -i, 0)^\mu .\end{aligned}\tag{120}$$

These vectors represent the states of the vector boson with definite angular momentum $J^3 = +1, 0, -1$.

Now boost along the \hat{z} axis to high energy, $p^\mu = (E, 0, 0, p)^\mu$. The boosts of the polarization vectors in (120) are

$$\begin{aligned}\epsilon_+^\mu &= \frac{1}{\sqrt{2}}(0, 1, +i, 0)^\mu \\ \epsilon_0^\mu &= \left(\frac{p}{m}, 0, 0, \frac{E}{m}\right)^\mu \\ \epsilon_-^\mu &= \frac{1}{\sqrt{2}}(0, 1, -i, 0)^\mu .\end{aligned}\tag{121}$$

The transverse polarization vectors ϵ_+ , ϵ_- are left unchanged by the boost. However, for the longitudinal polarization vector ϵ_0 , the components grow without bound. At very high energy

$$\epsilon_0^\mu \rightarrow \frac{p^\mu}{m} .\tag{122}$$

Another way to understand this is to recall that the polarization sum for a massive vector boson is written covariantly as

$$\sum_i \epsilon_i^\mu \epsilon_j^\nu = -\left(g^{\mu\nu} - \frac{p^\mu p^\nu}{m^2}\right) .\tag{123}$$

In the rest frame of the vector boson, this is the projection onto the 3 spacelike polarization vectors. For a highly boosted vector boson, however, the second term in

parentheses in this expression has matrix elements that grow large in the same way as (122).

This potentially leads to very large contributions to amplitudes for high-energy vector bosons, even threatening violation of unitarity. An example of this problem is found in the production of a pair of massive vector bosons in e^+e^- annihilation. The amplitude for production of a pair of scalar bosons in QED is

$$i\mathcal{M}(e^+e^- \rightarrow \phi^+\phi^-) = -i\frac{e^2}{s}(2E)\sqrt{2}\epsilon_- \cdot (k_- - k_+) , \quad (124)$$

where k_+, k_- are the scalar particle momenta. In $e^+e^- \rightarrow W^+W^-$, we might expect that this formula generalizes to

$$i\mathcal{M}(e^+e^- \rightarrow \phi^+\phi^-) = i\frac{e^2}{s}(2E)\sqrt{2}\epsilon_- \cdot (k_+ - k_-) \epsilon^*(k_+) \cdot \epsilon^*(k_-) . \quad (125)$$

where $\epsilon(k_+), \epsilon(k_-)$ are the W^+ and W^- polarization vectors. For longitudinally polarized W bosons, this extra factor becomes

$$\frac{k_+ \cdot k_-}{m_W^2} = \frac{s - 2m_W^2}{2m_W^2} \quad (126)$$

at high energy. This growth of the production amplitude really would violate unitarity.

This raises the question: Are the enhancements due to $\epsilon_0 \sim p/m$ at high energy actually present? Do these enhancements appear always, sometimes, or never?

The answer to this question is given by the Goldstone Boson Equivalence Theorem (GBET) of Cornwall, Levin, and Tiktopoulos and Vayonakis [5,6].

When a W boson or other gauge boson acquires mass through the Higgs mechanism, this boson must also acquire a longitudinal polarization state that does not exist for a massless gauge boson. The extra degree of freedom is obtained from the symmetry-breaking Higgs field, for which a Goldstone boson is gauged away. When the W is at rest, it is not so clear which polarization state came from the Higgs field. However, for a highly boosted W boson, there is a clear distinction between the transverse and longitudinal polarization states. The GBET states, in the limit of high energy, the couplings of the longitudinal polarization state are precisely those of the original Goldstone boson,

$$\mathcal{M}(X \rightarrow Y + W_0^+(p)) = \mathcal{M}(X \rightarrow Y + \pi^+(p)) \left(1 + \mathcal{O}\left(\frac{m_W}{E_W}\right)\right) \quad (127)$$

The proof is too technical to give here. Some special cases are analyzed in Chapter 21 of [7]. A very elegant and complete proof, which accounts for radiative corrections

and includes the possibility of multiple boosted vector bosons, has been given by Chanowitz and Gaillard in [35]. Both arguments rely in an essential way on the underlying gauge invariance of the theory.

In the rest of this section, I will present three examples that illustrate the various aspects of this theorem.

5.2 W polarization in top quark decay

The first application is the theory of the polarization of the W boson emitted in top quark decay, $t \rightarrow bW^+$.

It is straightforward to compute the rates for top quark decay to polarized W bosons. These rates follow directly from the form of the $V-A$ coupling. The matrix element is

$$i\mathcal{M} = i \frac{g}{\sqrt{2}} u_L^\dagger(b) \bar{\sigma}^\mu u_L(t) \epsilon_\mu^* . \quad (128)$$

In evaluating this matrix element, I will ignore the b quark mass, a very good approximation. I will use coordinates in which the t quark is at rest, with spin orientation given by a 2-component spinor ξ , and the W^+ is emitted in the $\hat{3}$ direction. The b quark is left-handed and moves in the $-\hat{3}$ direction. Then the spinors are

$$u_L(b) = \sqrt{2E_b} \begin{pmatrix} -1 \\ 0 \end{pmatrix} \quad u_L(t) = \sqrt{m_t} \xi . \quad (129)$$

For a W_-^+ ,

$$\bar{\sigma} \cdot \epsilon_-^* = \frac{1}{\sqrt{2}} (\sigma^1 + i\sigma^2) = \sqrt{2} \sigma^+ \quad (130)$$

and so the amplitude is

$$i\mathcal{M} = ig \sqrt{2m_t E_b} \xi_2 . \quad (131)$$

with, from 2-body kinematics, $E_b = (m_t^2 - m_w^2)/2m_t$. For a W_+^+ , the sigma matrix structure is proportional to σ^- and the amplitude vanishes. For a W_0^+ ,

$$\bar{\sigma} \cdot \epsilon_0^* = -\frac{p + E\sigma^3}{m_W} \quad (132)$$

and the amplitude is

$$i\mathcal{M} = ig \sqrt{2m_t E_b} \frac{m_t}{m_W} \xi_1 . \quad (133)$$

Squaring these matrix elements, averaging over the t spin direction, and integrating over phase space, we find

$$\Gamma(t \rightarrow bW_-^+) = \frac{\alpha_w}{8} m_t \left(1 - \frac{m_W^2}{m_t^2}\right)^2$$

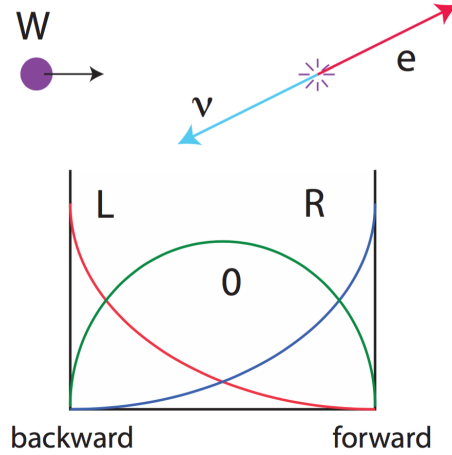


Figure 20: Angular distributions of $\cos \theta_*$ in W boson decay for each of the three possible polarization states.

$$\begin{aligned}\Gamma(t \rightarrow bW_+^+) &= 0 \\ \Gamma(t \rightarrow bW_0^+) &= \frac{\alpha_w}{8} m_t \left(1 - \frac{m_W^2}{m_t^2}\right)^2 \cdot \frac{m_t^2}{2m_W^2} .\end{aligned}\quad (134)$$

From these formulae, we see that the fraction of longitudinally polarized W bosons is

$$\frac{\Gamma(t \rightarrow bW_0^+)}{\Gamma(t \rightarrow bW^+)} = \frac{m_t^2/2m_W^2}{1 + m_t^2/2m_W^2} \approx 70\% .\quad (135)$$

The polarization of W bosons in t decay can be measured by reconstructing full $pp \rightarrow t\bar{t} \rightarrow \ell\nu + 4 \text{ jet}$ events. Beginning in the t rest frame, we boost the leptonically decaying W to rest. The angular distribution of the decay lepton in the W frame is then given by for the three polarization states by

$$\frac{d\Gamma}{d\cos\theta_*} \sim \begin{cases} (1 + \cos\theta_*)^2 & + \\ \sin^2\theta_*/2 & 0 \\ (1 - \cos\theta_*)^2 & - \end{cases} ,\quad (136)$$

where θ_* is the angle between the boost direction and the lepton direction. These angular distributions, which are also a consequence of $V-A$, are illustrated in Fig. 20. The actual distributions measured in hadron collisions are distorted from the idealized ones, since leptons with $\cos\theta_*$ near -1 , which implies low lab-frame energy, have low acceptance. Figure 21 shows the $\cos\theta_*$ distribution measured by the CMS experiment at the LHC and indicates an excellent agreement with the SM prediction [36].

An interesting feature of this prediction is the form of the amplitude (133). This amplitude is enhanced by a factor m_t/m_W , just as we might have expected from

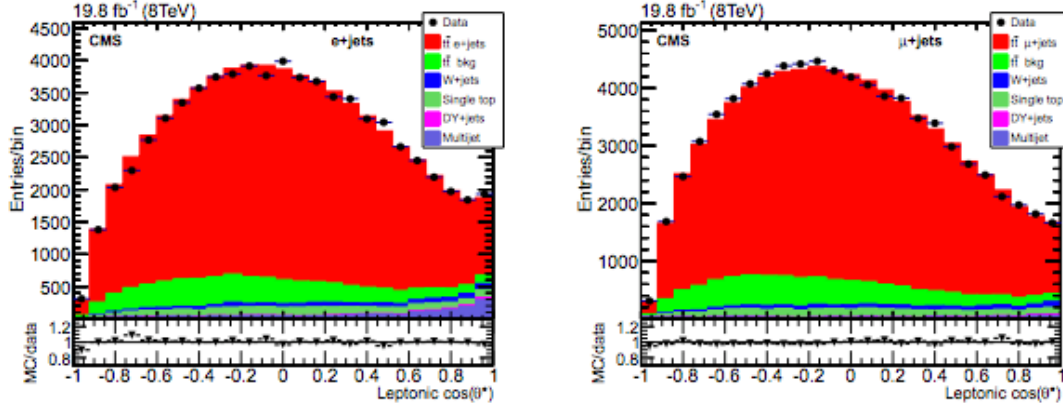


Figure 21: CMS measurement of the $\cos \theta_*$ distribution in top decay, compared to a simulation that represents the SM expectation [36].

(122). This behavior can be understood using the GBET. According to the GBET, we should find

$$i\mathcal{M}(t \rightarrow bW_0^+) \rightarrow i\mathcal{M}(t \rightarrow b\pi^+) . \quad (137)$$

The amplitude for emission of a Higgs boson should be proportional to the top quark Yukawa coupling y_t , given by

$$m_t = \frac{y_t v}{\sqrt{2}} . \quad (138)$$

So the GBET predicts that the rate for t decay to a longitudinal W should be larger than the rate to a transverse W by the factor

$$\frac{y_t^2}{g^2} = \frac{2m_t^2/v^2}{4m_W^2/v^2} = \frac{m_t^2}{2m_W^2} , \quad (139)$$

and this is exactly what we found in the explicit calculation.

5.3 High energy behavior in $e^+e^- \rightarrow W^+W^-$

The next example to study is the high energy behavior of the reaction

$$e^+e^- \rightarrow W^+W^- . \quad (140)$$

I argued earlier that the amplitude for this process cannot show the enhancement (122), at least in the most straightforward way, since this would lead to an amplitude that violates unitarity. Indeed, the prediction of the GBET is that

$$\mathcal{M}(e^+e^- \rightarrow W_0^+W_0^-) \rightarrow \mathcal{M}(e^+e^- \rightarrow \pi^+\pi^-) . \quad (141)$$

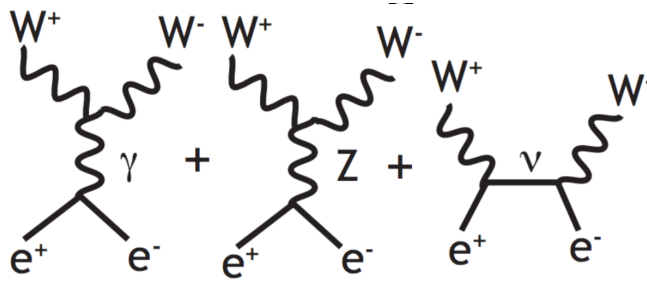


Figure 22: Feynman diagrams for the process $e^+e^- \rightarrow W^+W^-$.

Using (36), the high-energy limit of $SU(2) \times U(1)$, and the quantum numbers of the Higgs field $(I, Y) = (\frac{1}{2}, \frac{1}{2})$, we can readily work out that the right-hand side of (141) is, for an $e_R^- e_L^+$ initial state,

$$i\mathcal{M} = -i(2E)\sqrt{2} \epsilon_+ \cdot (k_- - k_+) \cdot \frac{e^2}{2c_w^2} \frac{1}{s}, \quad (142)$$

and for an $e_L^- e_R^+$ initial state,

$$i\mathcal{M} = -i(2E)\sqrt{2} \epsilon_- \cdot (k_- - k_+) \cdot \left(\frac{e^2}{4c_w^2} \frac{1}{s} + \frac{e^2}{4c_w^2} \frac{1}{s} \right), \quad (143)$$

where k_- and k_+ are the final-state momenta. So it must be that the expression we guessed in (125) is either incorrect or is cancelled by other factors.

In the SM, the complete tree level amplitude for $e^+e^- \rightarrow W^+W^-$ is given by a sum of three diagrams, shown in Fig. 22. It will be instructive to work out the sum of diagrams in a careful way. I will do this first for the initial state $e_R^- e_L^+$, for which the neutrino diagram does not appear.

The full matrix element involves the Yang-Mills vertex for the $WW\gamma$ and WWZ interactions. It is

$$i\mathcal{M} = (-ie)(ie)2E\sqrt{2} \epsilon_{+\mu} \left[\frac{-i}{s} + \frac{-s_w^2 c_w}{s_w c_w s - m_Z^2} \frac{-i}{s} \right] \cdot \left[\epsilon^*(-) \epsilon^*(+)(k_- - k_+)^\mu + (-q - k_-) \epsilon^*(+) \epsilon^{*\mu}(-) + (k_+ + q) \epsilon^*(-) \epsilon^{*\mu}(+) \right], \quad (144)$$

where $q = k_- + k_+$ and, in the second line, $\epsilon^*(-)$ and $\epsilon^*(+)$ are the W polarizations. To evaluate the high-energy limit for longitudinally polarized W bosons, send

$$\epsilon^*(-) \rightarrow \frac{k_-}{m_W} \quad \epsilon^*(+) \rightarrow \frac{k_+}{m_W}. \quad (145)$$

Then the second term in brackets becomes

$$\begin{aligned} & \frac{1}{m_W^2} \left[k_- k_+ (k_- - k_+)^{\mu} - 2k_- k_+ k_-^{\mu} + 2k_+ k_- k_+^{\mu} \right] \\ &= -\frac{k_- k_+}{m_W^2} (k_- - k_+)^{\mu} = -\frac{s - 2m_W^2}{2m_W^2} (k_- - k_+)^{\mu} . \end{aligned} \quad (146)$$

This expression has the enhancement (126). However, there is a nice cancellation in the first term in brackets,

$$\left[\frac{-i}{s} - \frac{-i}{s - m_Z^2} \right] = \frac{i m_Z^2}{s(s - m_Z^2)} . \quad (147)$$

Assembling the pieces and using $m_W^2 = m_Z^2 c_w^2$, we find

$$i\mathcal{M} = ie^2 2E\sqrt{2} \epsilon_{+\mu} (k_- - k_+)^{\mu} \left(-\frac{s - 2m_W^2}{2c_w^2 s (s - m_Z^2)} \right) , \quad (148)$$

which indeed agrees with (142) in the high energy limit.

For the $e_L^- e_R^+$ case, the γ and Z diagrams do not cancel, and so the neutrino diagram is needed. The first two diagrams contribute

$$\begin{aligned} i\mathcal{M} &= (-ie)(ie)2E\sqrt{2} \epsilon_{+\mu} \left[\frac{-i}{s} + \frac{(1/2 - s_w^2) c_w}{s_w c_w} \frac{-i}{s_w s - m_Z^2} \right] \\ &\cdot \left[\epsilon^*(-) \epsilon^*(+) (k_- - k_+)^{\mu} + (-q - k_-) \epsilon^*(+) \epsilon^{*\mu}(-) + (k_+ + q) \epsilon^*(-) \epsilon^{*\mu}(+) \right] , \end{aligned} \quad (149)$$

After the reductions just described, there is a term in the high-energy behavior that does not cancel,

$$\begin{aligned} i\mathcal{M} &= ie^2 2E\sqrt{2} \epsilon_{-\mu} (k_- - k_+)^{\mu} \left[\frac{1}{2s_w^2 s} \right] \left(-\frac{s}{2m_W^2} \right) \\ &= \frac{ie^2}{4s_w^2} 2E\sqrt{2} \epsilon_{-\mu} (k_- - k_+)^{\mu} \frac{1}{m_W^2} . \end{aligned} \quad (150)$$

We must add to this the neutrino diagram, which contributes

$$i\mathcal{M} = \left(i\frac{g}{\sqrt{2}} \right)^2 v_R(\bar{p})^{\dagger} \bar{\sigma} \cdot \epsilon^*(+) \frac{i\sigma \cdot (p - k_-)}{(p - k_-)^2} \bar{\sigma} \cdot \epsilon^*(-) u_L(p) . \quad (151)$$

Substituting $\epsilon^*(-) \rightarrow k_-/m_W$, the second half of this formula becomes

$$\frac{i\sigma \cdot (p - k_-)}{(p - k_-)^2} \bar{\sigma} \cdot \frac{k_-}{m_W} u(p) . \quad (152)$$

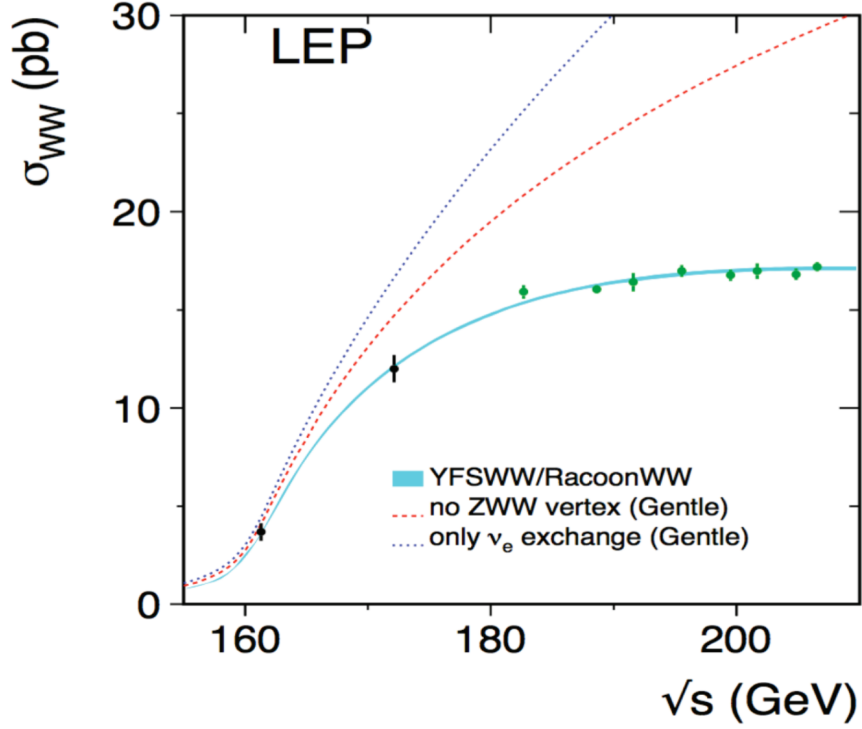


Figure 23: Measurement of $\sigma(e^+e^- \rightarrow W^+W^-)$ from the four LEP experiments, from [20].

Since $\bar{\sigma} \cdot p u_L(p) = 0$, this can be written

$$\frac{i\sigma \cdot (p - k_-)}{(p - k_-)^2} \bar{\sigma} \cdot \frac{(k_- - p)}{m_W} u(p) = -\frac{i}{m_W^2} u(p). \quad (153)$$

Sending $\epsilon^*(+) \rightarrow k_+/m_W = ((p + \bar{p})/2 + (k_+ - k_-)/2)/m_W$ and using $(\bar{\sigma} \cdot p)u_L = v_R^\dagger(\bar{\sigma} \cdot \bar{p}) = 0$, we finally find

$$i\mathcal{M} = -\frac{ie^2}{2s_w^2} 2E\sqrt{2} \epsilon_{-\mu} \frac{1}{2} (k_- - k_+)^\mu \frac{1}{m_W^2}, \quad (154)$$

and this indeed cancels the high-energy behavior (150) from the γ and Z diagrams. To fully verify (143), we would need to carry out this calculation more exactly to pick up all subleading terms at high energy. It does work out correctly, as was first shown by Alles, Boyer, and Buras [37].

The cross section for $e^+e^- \rightarrow W^+W^-$ was measured by the LEP experiments. The result is shown in Fig. 23 [20]. The lowest, solid line is the prediction of the SM, including one-loop radiative corrections. It is in excellent agreement with the measurements. The upper curves show the effect of omitting, first, the Z diagram and, second, both the γ and Z diagrams. Apparently, the cancellation I have demonstrated

here is important not only at very high energy but even in the qualitative behavior of the cross section quite close to threshold.

5.4 Parametrizing corrections to the Yang-Mills vertex

The cancellation described in the previous section clearly requires the precise structure of the Yang-Mills vertex that couples three vector bosons. Before the LEP measurements, when the gauge boson nature of the W and Z was less clear, theorists suggested that the $WW\gamma$ and WWZ vertices might be modified from the Yang-Mills form, and that such modifications could be tested by measurements of W reactions at high energy.

The most general Lorentz-invariant, CP conserving $WW\gamma$ vertex in which the photon couples to a conserved current has the form [38]

$$\begin{aligned} \Delta\mathcal{L} = e \left[i g_{1A} A_\mu (W^-_\nu W^{+\mu\nu} - W^+_\nu W^{-\mu\nu}) + i \kappa_A A_{\mu\nu} W^-_\mu W^+_\nu \right. \\ \left. + i \lambda_A \frac{1}{m_W^2} W^-_{\lambda\mu} W^{+\mu\nu} A_\nu \right]. \end{aligned} \quad (155)$$

In this formula, for each vector field, $V_{\mu\nu} = (\partial_\mu V_\nu - \partial_\nu V_\mu)$. We can write a similar generalization of the SM WWZ vertex, with parameters g_{1Z} , κ_Z , λ_Z and overall coupling ec_w/s_w . The choice

$$g_{1\gamma} = g_{1Z} = \kappa_A = \kappa_Z = 1 \quad \lambda_A = \lambda_Z = 0 \quad (156)$$

gives the SM coupling. If we relax the assumption of CP conservation, several more terms can be added.

It was quickly realized that any changes to the SM vertex produce extra contributions to the W production amplitudes that are enhanced by the factor s/m_W^2 . In view of the discussion earlier in this section, this is no surprise. If the additional terms violate the gauge invariance of the theory, the GBET will not be valid, and the cancellations it requires will not need to occur. However, this idea would seem to be already excluded by the strong evidence from the precision electroweak measurements that the W and Z are the vector bosons of a gauge theory.

Still, there is a way to modify the $WW\gamma$ and WWZ vertices in a way that is consistent with gauge invariance. It is certainly possible that there exist new heavy particles that couple to the gauge bosons of the SM. The quantum effects of these particles can be described as a modification of the SM Lagrangian by the addition of new gauge-invariant operators. This approach to the parametrization of new physics effects has become known as Effective Field Theory (EFT). The SM already contains the most general $SU(2) \times U(1)$ -invariant operators up to dimension 4, but new physics at high energy can add higher-dimension operators, beginning with dimension 6.

There are many dimension 6 operators that can be added to the SM. Even for 1 generation of fermions, there are 84 independent dimension 6 operators, of which 59 are baryon-number and CP-conserving [39]. The theory of these operators has a complexity that I do not have room to explain here. It is possible to make many different choices for the basis of these operators, using the fact that combinations of these operators are set to zero by the SM equations of motion. The theory of EFT modifications of the SM is reviewed in [40] and, in rather more detail, in [41]. I will give only a simple example here.

Consider, then, adding to the SM the dimension-6 operators

$$\Delta\mathbf{L} = \frac{c_T}{2v^2}\Phi^\mu\Phi_\mu + \frac{4gg'}{m_W^2}\Phi^a W_{\mu\nu}^a B^{\mu\nu} + \frac{g^3 c_{3W}}{m_W^2}\epsilon^{abc}W_{\mu\nu}^a W^{b\nu}{}_\rho W^{c\rho\mu} , \quad (157)$$

where, in this formula, $W_{\mu\nu}^a$ and $B_{\mu\nu}$ are the $SU(2)$ and $U(1)$ field strengths and Φ_μ , Φ^a are bilinears in the Higgs field,

$$\Phi_\mu = \varphi^\dagger D_\mu \varphi - (D_\mu \varphi)^\dagger \varphi \quad \Phi^a = \varphi^\dagger \frac{\sigma^a}{2} \varphi . \quad (158)$$

It can be shown that these shift the parameters of the $WW\gamma$ and WWZ couplings to

$$\begin{aligned} g_{1Z} &= 1 + \left[\frac{c_T}{2(c_w^2 - s_w^2)} - \frac{8s_w^2 c_{WB}}{c_w^2(c_w^2 - s_w^2)} \right] \\ \kappa_A &= 1 - 4c_{WB} \\ \lambda_A &= -6g^2 c_{3W} \end{aligned} \quad (159)$$

The parameter $g_{1A} = 1$ is not shifted; this is the electric charge of the W boson. The remaining two parameters obey

$$\kappa_Z = g_{1Z} - \frac{s_w^2}{c_w^2}(\kappa_A - 1) \quad \lambda_Z = \lambda_A . \quad (160)$$

It can be shown that the relations (160) are maintained for any set of dimension-6 perturbations of the SM. They may be modified by dimension-8 operators.

Dimension-6 operators also contribute to the S and T parameters discussed at the end of the previous section. From the perturbation (157),

$$\begin{aligned} \alpha S &= 32s_w^2 c_{WB} \\ \alpha T &= c_T \end{aligned} \quad (161)$$

Given that EFT is based on gauge-invariant Lagrangian, this formalism for parametrizing new physics can be worked out explicitly in great detail. QCD and

electroweak radiative corrections can be included. The higher-dimension operators in the EFT must of course be renormalized according to some scheme, and the detailed formulae will depend on the scheme.

A dimension-6 operator has a coefficient with the units of $(\text{GeV})^{-2}$. Thus, the effects of such operators are suppressed by one factor of s/M^2 , where M is then mass scale of new particles. Contributions from dimension-8 operators suppressed by $(s/M^2)^2$, and similarly for operators of still higher dimension. So, an analysis that puts constraints on dimension-6 operators, ignoring the effects of dimension-8 operators is properly valid only when $s/M^2 \ll 1$.

As a corollary to this point, I call your attention to a Devil's bargain that arises frequently in tests of the structure of W and Z vertices at hadron colliders. In pp collisions, the parton center of mass energy \hat{s} varies over a wide range. There is always a region of phase space where \hat{s} becomes extremely large. This is the region that has the greatest sensitivity to higher-dimension operators. It is tempting to apply event selections that emphasize this region to obtain the strongest possible limits.

However, this is exactly the region where operators of dimension 8 and higher might also be important. In many models, these give negative contribution. Then a parametrization that uses only dimension-6 operators leads to limits on their coefficients that are stronger than the limits that would be obtained in a more complete theory.

The question of how to interpret limits on dimension-6 EFT coefficients is now hotly debated in the literature. My personal position is on one extreme, that only analyses in which $\hat{s}/M^2 \ll 1$ for all events included in the analysis should be trusted. The authors of [42] advocate for a much more aggressive approach. Experimenters who quote such limits should study this issue carefully.

On the other hand, the SM itself makes precise predictions in all regions of \hat{s} . Your first priority should be to discover a deviation from these predictions. If you are able to demonstrate a substantial deviation from the SM predictions in any region of phase space, we can all have fun quarreling about the interpretation of this result.

5.5 W parton distributions

As a final topic in this section, I will discuss a situation in which the GBET might be expected to apply, but it does not. This involves processes in which a W boson is radiated from a quark or lepton with small transverse momentum relative to the fermion direction. In QCD, the collinear radiation of gluons from initial quarks is essential in creating the observed quark and gluon parton distributions. In Section 4.2, we saw that collinear radiation of photons from initial electrons and positrons is also an important effect that makes qualitative changes in the Z resonance line shape. In

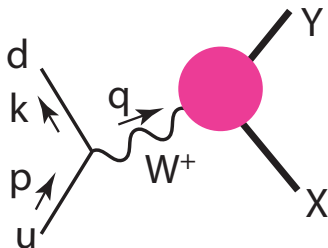


Figure 24: Kinematics of a process in which a W is emitted collinearly from a quark and then initiates a large-momentum-transfer reaction.

this section, I will present the analogous theory for collinear W boson emission [43]. I will carry out the analysis for quark initial states, but the same theory applies to electron and positron initial states.

For definiteness, consider the following setup: An initial u quark, with momentum p , emits an almost collinear W^+ boson, with momentum q ,

$$u(p) \rightarrow d(k) + W^+(q) . \quad (162)$$

The W boson must be off-shell. This emission will be part of a process shown in Fig. 24, in which the virtual W collides with a parton from the other proton to initiate a hard-scattering reaction. An important class of processes of this type is WW scattering, including the reaction $W^+W^- \rightarrow h$ that we will discuss in Section 6.2.

For W reactions that involve the Higgs boson, it will be important to have W bosons with longitudinal polarization. According to the GBET, a longitudinally polarized W boson should have a coupling equal to that of the corresponding Goldstone boson π^+ from the Higgs sector. Then the study of high energy W boson reactions allows us to directly measure the strength of Higgs boson interactions. However, it is not clear that it is possible to radiate longitudinally polarized W bosons from initial quarks. A π^+ couples to a light fermion with its Higgs Yukawa coupling, that is, negligibly, the the radiation of longitudinally polarized W bosons would seem to be forbidden by the GBET.

To understand the correct story, we must compute the $u \rightarrow Wd$ emission amplitude explicitly. In this calculation, I will take the W boson to be emitted approximately collinearly with the u quark. The analysis is very similar to calculation of the Altarelli-Parisi splitting functions that you will find, for example, in Chapter 17 of [7]. I will assume that the W has $p_T \sim m_W \ll p_{\parallel}$.

First, I write the momentum vectors for the quarks, taking the u quark to move in the $\hat{3}$ direction and the d quark to carry away an energy fraction $(1 - x)$ and to

have a small transverse momentum,

$$\begin{aligned} p &= (E, 0, 0, E) \\ k &= ((1-z)E, -p_T, 0, (1-z)E - \frac{p_T^2}{2(1-z)E}). \end{aligned} \quad (163)$$

The momentum k is on-shell to order p_T^2 . The W momentum vector is then determined by momentum conservation

$$q = (zE, p_T, 0, zE + \frac{p_T^2}{2(1-z)E}). \quad (164)$$

The denominator of the W propagator is then

$$q^2 - m_W^2 = -p_T^2 - \frac{z}{(1-z)}p_T^2 - m_W^2 = -(\frac{p_T^2}{1-z} + m_W^2). \quad (165)$$

Next, we compute the matrix elements for W emission

$$i\mathcal{M} = ig u_L^\dagger(k) \bar{\sigma} \cdot \epsilon_W^* u_L(p) \quad (166)$$

to first order in (p_T, m_W) . The explicit form of the spinors is

$$u_L(k) = \sqrt{2(1-z)E} \begin{pmatrix} p_T/2(1-z) \\ 1 \end{pmatrix} \quad u_L(p) = \sqrt{2E} \begin{pmatrix} 0 \\ 1 \end{pmatrix}. \quad (167)$$

The W polarization vectors are

$$\epsilon_\pm^{*\mu} = (0, 1, \mp i, -p_T/zE)^\mu / \sqrt{2} \quad (168)$$

for the transverse polarizations, and

$$\epsilon_0^{*\mu} = (q, p_T, 0, zE)^\mu / m_W \quad (169)$$

for the longitudinal polarization state. In this formula

$$q = [(zE)^2 - m_W^2]^{1/2} = zE - \frac{m_W^2}{2zE} \quad (170)$$

Then

$$\begin{aligned} \bar{\sigma} \cdot \epsilon_+^* &= \frac{1}{\sqrt{2}} \begin{pmatrix} -p_T/zE & 0 \\ 2 & p_T/zE \end{pmatrix} \\ \bar{\sigma} \cdot \epsilon_-^* &= \frac{1}{\sqrt{2}} \begin{pmatrix} -p_T/zE & 2 \\ 0 & p_T/zE \end{pmatrix} \\ \bar{\sigma} \cdot \epsilon_0^* &= \frac{1}{m_W} \begin{pmatrix} q + zE & p_T \\ p_T & q - zE \end{pmatrix} \end{aligned} \quad (171)$$

With these ingredients, it is straightforward to work out the matrix elements for the three W polarization states,

$$i\mathcal{M}(u \rightarrow dW^+) = ig \cdot \begin{cases} \sqrt{1-z} p_T/z & + \\ \sqrt{1-z} p_T/z(1-z) & - \\ -\sqrt{1-z} m_W/\sqrt{2z} & 0 \end{cases} . \quad (172)$$

We can convert these expressions to cross sections for complete W -induced processes. The cross section for a process $uX \rightarrow dY$, in the approximation in which the W is almost on shell, is given by

$$\sigma = \frac{1}{2s} \int \frac{d^3k}{(2\pi)^3 2k} \int d\Pi_Y (2\pi)^4 \delta^{(4)}(p + p_X - k - p_Y) \left| \mathcal{M}(u \rightarrow dW^+) \frac{1}{q^2 - m_W^2} \mathcal{M}(W^+ X \rightarrow Y) \right|^2 \quad (173)$$

In the collinear kinematics, with $\hat{s} = zs$

$$\frac{1}{2s} \int \frac{d^3k}{(2\pi)^3 2k} = \frac{1}{2\hat{s}/z} \int \frac{dz E d^2p_T}{16\pi^3 E(1-z)} = \frac{1}{2\hat{s}} \int \frac{dz dp_T^2 \pi}{16\pi^3} \frac{z}{(1-z)} \quad (174)$$

Then, also using (165), (173) simplifies to

$$\sigma = \int dz \int \frac{dp_T^2}{(4\pi)^2} \frac{z}{(1-z)} |\mathcal{M}(u \rightarrow dW^+)|^2 \frac{1}{p_T^2/(1-z) + m_W^2} \cdot \frac{1}{2\hat{s}} \int d\Pi_Y (2\pi)^4 \delta^{(4)}(q + p_X - p_Y) |\mathcal{M}(W^+ X \rightarrow Y)|^2 \quad (175)$$

The last line of (175) is $\sigma(W^+(q) + X \rightarrow Y)$. Then (175) has the form of a parton model cross section

$$\sigma(uX \rightarrow dY) = \int dz f_{W \leftarrow u}(z) \sigma(W^+ X \rightarrow Y) \quad (176)$$

where $f_{W \leftarrow u}(z)$ is the parton distribution for a W boson in the u quark,

$$f_{W \leftarrow u}(z) = \int \frac{dp_T^2}{(4\pi)^2} \frac{z}{(1-z)} \frac{(1-z)^2}{(p_T^2 + (1-z)m_W^2)^2} |\mathcal{M}(u \rightarrow dW^+)|^2 . \quad (177)$$

We can evaluate this parton distribution for each W polarization state by using the formula (172). The result is

$$\begin{aligned} f_{W-}(z) &= \frac{\alpha_2}{4\pi} \int \frac{dp_T^2 p_T^2}{(p_T^2 + (1-z)m_W^2)^2} \frac{1}{z} \\ f_{W+}(z) &= \frac{\alpha_2}{4\pi} \int \frac{dp_T^2 p_T^2}{(p_T^2 + (1-z)m_W^2)^2} \frac{(1-z)^2}{z} \\ f_{W0}(z) &= \frac{\alpha_2}{8\pi} \int \frac{dp_T^2 m_W^2}{(p_T^2 + (1-z)m_W^2)^2} \frac{(1-z)^2}{z} \end{aligned} \quad (178)$$

For the transverse polarizations, we find a result very similar to the Altarelli-Parisi splitting function for collinear gluon emission,

$$f_{WT}(z) = \frac{\alpha_w}{4\pi} \frac{1 + (1 - z)^2}{z} \cdot \log \frac{Q^2}{m_W^2}, \quad (179)$$

where Q^2 is the upper limit of the p_T^2 integral, which is set by the momentum transfer in the hard reaction.

For the longitudinal W polarization, the story is different. The integral over p_T is convergent, so that the p_T is restricted to the region $p_T \sim m_W$. In this regime, as we see explicitly, longitudinal W bosons can be produced with coupling strength g . Apparently, in this process, the error term in the GBET is actually $\mathcal{O}(m_W/p_T)$, which is consistent with (127) but, still, larger than we might expect. The reduction of the longitudinal W boson to a Higgs boson then is not accurate in the region $p_T \sim m_W$, though it does apply—and cuts off the amplitude—when $p_T \gg m_W$.

When we perform the convergent integral over p_T , we find that the parton distribution for W_0 is substantial [43],

$$f_{W_0}(z) = \frac{\alpha_w}{8\pi} \frac{1 - z}{z}. \quad (180)$$

Then the proton does contain longitudinal W bosons, which can induce Higgs sector reactions when this proton collides with another proton at high energy. The collinear longitudinal W bosons have $p_T \sim m_W$ but not higher, a kinematic feature that can be used to suppress backgrounds from reactions involving transversely-polarized W bosons.

6 The Standard Model theory of Higgs boson decays

There remains one heavy particle of the SM that we have not yet discussed, the Higgs boson. The Higgs boson has a central role in the structure of the weak interactions. Its field is the agent that breaks the $SU(2) \times U(1)$ symmetry and generates the masses of all quarks, leptons, and vector bosons. This at the same time forms a unified picture of the electroweak interactions as we have studied them so far and also points to new mysteries whose explanations are still to be found.

The best way to enter a discussion of the Higgs boson is to understand thoroughly the predictions for the properties of this particle given by the SM. The Higgs sector involves one more parameter of the SM beyond those we have discussed already, the Higgs field self-coupling λ . However, this coupling is fixed by the measurement of the

Figure 25: Feynman rules for couplings of the Higgs boson.

Higgs boson mass. Thus, the SM makes precise predictions for all of the Higgs boson cross sections and branching fractions. These predictions provide a starting point for any discussion of the properties of the Higgs boson in model that generalize the SM. An excellent reference on the theory of the Higgs boson in the Standard Model is [44]. The best current calculations of the Higgs boson properties are compiled in [45].

6.1 Decay modes of the Higgs boson

The basic elements of the SM description of the Higgs boson are extremely simple. A general configuration of the Higgs field can be written in the form of an $SU(2)$ gauge transformation acting on a simple scalar field

$$\varphi(x) = \exp[-i\alpha^a(x)\sigma^a/2] \begin{pmatrix} 0 \\ (v + h(x))/\sqrt{2} \end{pmatrix}. \quad (181)$$

We can remove the prefactor by a choice of gauge. Then the Higgs field reduces to a vacuum expectation value v and the dynamical scalar field $h(x)$. The values of m_W and g give

$$v = 246 \text{ GeV}. \quad (182)$$

The vertices of $h(x)$ are given by shifting v everywhere it appears in the SM

$$v \rightarrow v + h(x). \quad (183)$$

This gives rise to the Feynman rules shown in Fig. 25. Within the SM, there is no freedom to change these vertices.

The couplings in Fig. 25 imply that a heavy Higgs boson would decay dominantly into pairs of the other heavy particles of the SM,

$$h \rightarrow W^+W^-, h \rightarrow ZZ, h \rightarrow t\bar{t} \quad (184)$$

However, it has been found at the LHC that there is no heavy resonance that decays to these final states. On the other hand, a narrow resonance with the properties of

the Higgs boson has been found at the LHC at a mass of 125 GeV. At this mass value, the otherwise dominant decay modes of the Higgs boson are kinematically forbidden. The actual decay modes of the Higgs are all suppressed in some way, by factors

$$\frac{m_f^2}{m_W^2}, \quad \frac{\alpha_w}{4\pi}, \quad \text{or} \quad \left(\frac{\alpha_s}{4\pi}\right)^2. \quad (185)$$

This means that the decay pattern of the Higgs boson will be more complex than might have been expected, but also that it should be very rich, with a large number of decay modes accessible to observation.

To describe these decays, I begin with the decays to fermions. The matrix element for Higgs decay to a light fermion is

$$i\mathcal{M}(h \rightarrow f_R \bar{f}_R) = -i \frac{m_f}{v} u_R^\dagger v_R = -i \frac{m_f}{v} (2E). \quad (186)$$

and similarly for decay to $f_L \bar{f}_L$. The total decay rate is

$$\Gamma(h \rightarrow f \bar{f}) = \frac{1}{2m_h} \frac{1}{8\pi} \frac{m_f^2 m_h^2}{v^2} \cdot 2, \quad (187)$$

or, using $v^2 = 4m_W^2/g^2$,

$$\Gamma(h \rightarrow f \bar{f}) = \frac{\alpha_w}{8} m_h \frac{m_f^2}{m_W^2}. \quad (188)$$

For final-state leptons, we can immediately evaluate this,

$$\Gamma(h \rightarrow \tau^+ \tau^-) = 260 \text{ keV} \quad \Gamma(h \rightarrow \mu^+ \mu^-) = 9 \text{ keV} \quad (189)$$

for $m_h = 125 \text{ GeV}$.

For decays to quarks, a few more details must be added. The quark mass must be defined by some renormalization convention. An appropriate choice that absorbs large logarithms is to set the quark mass in (188) equal to the \overline{MS} quark mass evaluated at $Q = m_h$. This is related to the quark mass as usually quoted by

$$m_f(m_h) = m_f(m_f) \left[\frac{\alpha_s(m_h)}{\alpha_s(m_f)} \right]^{4/b_0} (1 + \mathcal{O}(\alpha_s)), \quad (190)$$

where b_0 is the first coefficient of the QCD β function, equal to 23/3 for 5 light quark flavors. This means that the values of the quark masses appropriate to the calculation of Higgs boson branching ratios are

$$\begin{array}{ccccc} m_u & m_d & m_s & m_c & m_b \\ 1.5 & 3 & 60 & 700 & 2800 \end{array} \quad (191)$$

with all values in MeV. The formula (188) must also be multiplied by the color factor of 3 and a substantial QCD correction

$$3 \cdot \left(1 + \frac{17}{3\pi} \alpha_s(m_h) + \dots\right) = 3 \cdot 1.24 . \quad (192)$$

Then, for example,

$$\Gamma(h \rightarrow b\bar{b}) = \frac{\alpha_w m_h}{8} \left(\frac{2.8}{m_W}\right)^2 \cdot 3 \cdot 1.24 = 2.4 \text{ MeV} . \quad (193)$$

After we compute the other major Higgs boson decay rates, this will correspond to a branching fraction of 58%. Then the total width of the Higgs boson is predicted to be about 4.1 MeV, and the other fermion branching fractions should be

$$\begin{array}{cccc} \tau^+\tau^- & c\bar{c} & s\bar{s} & \mu^+\mu^- \\ 6.3\% & 3\% & 0.03\% & 0.02\% \end{array} \quad (194)$$

It is somewhat surprising that the branching ratio for $\tau^+\tau^-$ is larger than that for $c\bar{c}$, despite the presence of the color factor of 3.

For a heavy Higgs boson that can decay to on-shell W and Z bosons, the decay amplitudes would be

$$\begin{aligned} i\mathcal{M}(h \rightarrow W^+W^-) &= i \frac{2m_W^2}{v} \epsilon^*(+) \cdot \epsilon^*(-) \\ i\mathcal{M}(h \rightarrow ZZ) &= i \frac{2m_Z^2}{v} \epsilon^*(1) \cdot \epsilon^*(2) . \end{aligned} \quad (195)$$

For a very heavy Higgs boson, there is a further enhancement for the longitudinal polarization states,

$$\epsilon_0^*(1) \cdot \epsilon_0^*(2) \sim \frac{k_1 \cdot k_2}{m_Z^2} \sim \frac{m_h^2}{2m_Z^2} . \quad (196)$$

This factor is just

$$\frac{\lambda}{(g^2 + g'^2)} . \quad (197)$$

so the longitudinal Z and W couple to the Higgs boson as Higgs boson rather than as gauge bosons. This is in accord with the GBET.

For the actual situation of a 125 GeV Higgs boson, one or both of the W and Z bosons must be off-shell. Then the decay is best described as a Higgs decay to 4 fermions, as shown in Fig. 26. The rate is suppressed by a factor of α_w and by the off-shell W or Z propagator. The result is that the rate is competitive with $b\bar{b}$ for the WW mode and a factor 10 smaller for ZZ . The SM branching fractions for these off-shell vector boson modes are

$$BR(h \rightarrow WW^*) = 22\% \quad BR(h \rightarrow ZZ^*) = 2.7\% . \quad (198)$$

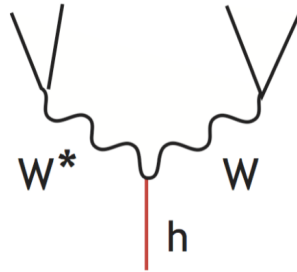


Figure 26: Feynman diagram for $h \rightarrow WW$ or $h \rightarrow ZZ$ decay with the vector bosons off-shell.

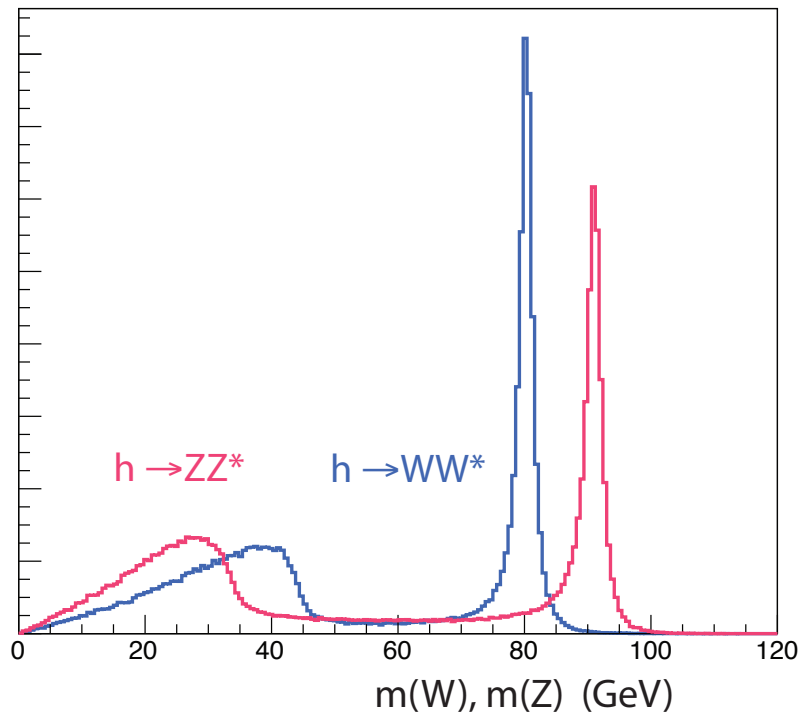


Figure 27: Mass distributions of the off-shell W and Z bosons in the decay of a 125 GeV Higgs boson.

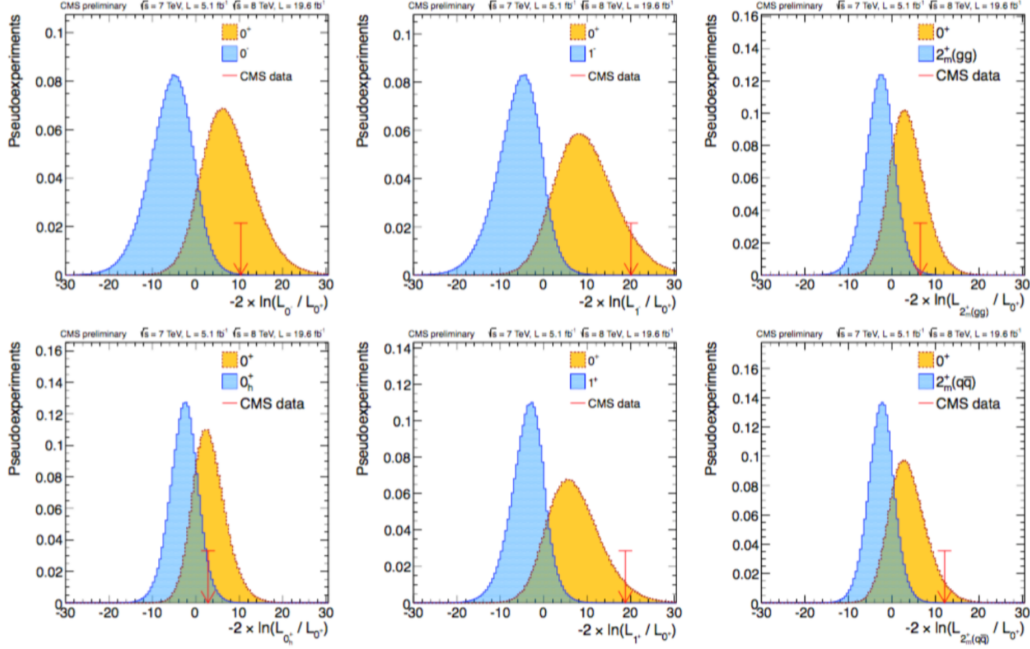


Figure 28: Likelihood distributions for tests of the spin and parity of the Higgs boson, from [46].

The W and Z mass distributions in these decays are shown in Fig. 27.

The Higgs boson decay to ZZ^* is exceptionally interesting because it is completely reconstructable in LHC events in which both Z s decay to charged leptons. The angular distribution of the leptons permits an analysis of the spin and parity of the Higgs resonance. In the SM, where the Higgs boson must have $J^P = 0^+$, the two Z bosons are predicted to be longitudinally polarized with the two decay planes parallel. The polarization of the Z can be measured from the decay angular distribution, as we have discussed for W bosons in (136). This prediction contrasts with that for other possible spin 0 assignments, in which the Higgs boson couples to ZZ^* through the interactions

$$0^- : h\epsilon^{\mu\nu\lambda\sigma} Z_{\mu\nu} Z_{\lambda\sigma} \quad 0^+ : hZ_{\mu\nu} Z^{\mu\nu} . \quad (199)$$

For the interactions in (199), the Z bosons are preferentially transversely polarized; also, with the 0^- type interaction, the two decay planes tend to be orthogonal. The SM prediction was tested even with the relatively small sample of about 15 $Z \rightarrow 4$ lepton events collected by each LHC experiment in run 1 of the LHC. Figure 28 shows the expected distributions of the likelihood for tests of the predicted SM coupling structure against the coupling structures in (199) and 4 other structures for which the resonance has spin 1 or spin 2. The actual value of the likelihood found by CMS experiment is shown by the arrow. In all cases, the results strongly favor the

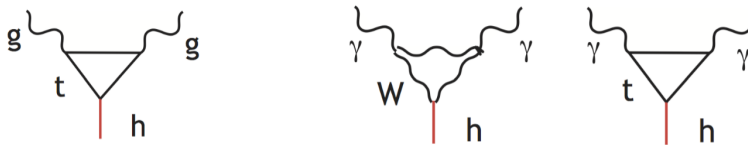


Figure 29: Loop diagrams contributing to the $h \rightarrow gg$ and $h \rightarrow \gamma\gamma$ decays.

SM hypothesis [46].

Finally, there are loop processes that allow the Higgs boson to decay to a pair of massless vector bosons, gg or $\gamma\gamma$, or to $Z\gamma$. The most straightforward of these to analyze is the hgg vertex. This is generated by loop diagrams that involve quarks, such as the diagram shown on the left in Fig. 29.

If we compute these loop diagrams, we obtain a local operator that gives an effective description of the Higgs boson coupling to gg . The lowest-dimension operator that is invariant under the $SU(3)$ gauge symmetry is

$$\Delta\mathcal{L} = \frac{1}{4}AhF_{\mu\nu}^a F^{\mu\nu a} , \quad (200)$$

where $F_{\mu\nu}^a$ is the QCD field strength. The coefficient A has the dimensions $(\text{GeV})^{-1}$. This operator yields the hgg vertex

$$-iA\delta^{ab}(k_1 \cdot k_2 g^{\mu\nu} - k_2^\mu k_1^\nu) . \quad (201)$$

I will compute the coefficient A in a moment, but, first I will estimate the order of magnitude of the contribution from a quark of mass m_q . There is a surprise here. This contribution is proportional to the Higgs Yukawa coupling, so it must be of the form

$$\alpha_s \frac{m_f}{v} \frac{1}{M} , \quad (202)$$

where M is the momentum that flows in the loop. For $2m_q \ll m_h$, M will be of order m_h and so the contribution (202) will be suppressed by a factor m_f/m_h . On the other hand, if $2m_q \gg m_h$, M will be of order m_q . In this case, the factors of m_q cancel and the diagram is at full strength no matter how large m_q is. This is bizarre but correct: The hgg vertex gets only small contributions from quarks to which the Higgs boson can decay and obtains full-strength contributions from quarks to which the Higgs boson *cannot* decay because they are too heavy.

In the SM, the only quark that contributes to the hgg vertex at full strength is the top quark. If there were a fourth generation of quarks that obtained their masses from the SM Higgs boson, each quark would produce an equal contribution to the hgg coupling, so that the total decay rate $\Gamma(h \rightarrow gg)$ would be $3^2 = 9$ times

the SM prediction [47]. Such a large shift is already excluded by the LHC Higgs measurements. This is a much stronger constraint on a fourth generation than the one that we found from precision electroweak measurements at the end of Section 3.

We can compute the contribution to the hgg vertex from a heavy quark t from the starting point of the QCD vacuum polarization. The 1-loop quark vacuum polarization diagram has the value

$$i(k^2 g^{\mu\nu} - k^\mu k^\nu) \text{tr}[t^a t^b] \frac{\alpha_s}{3\pi} \log \frac{\Lambda^2}{m_t^2}$$

$$i(k^2 g^{\mu\nu} - k^\mu k^\nu) \text{tr}[t^a t^b] \frac{\alpha_s}{3\pi} \log \frac{\Lambda^2}{m_t^2} . \quad (203)$$

We can produce the top quark loop diagram in Fig. 29, adding a zero-momentum Higgs boson, by shifting $v \rightarrow v + h$ as in (183). The expression (203) depends on v through $m_t = y_t v / \sqrt{2}$. This yields a contribution to the hgg vertex that is finite and equal to

$$i(k^2 g^{\mu\nu} - k^\mu k^\nu) \delta^{ab} \frac{\alpha_s}{3\pi} \frac{1}{v} . \quad (204)$$

Comparing to (201), we find

$$A = \frac{\alpha}{3\pi v} = \frac{g\alpha_s}{6\pi m_W} . \quad (205)$$

From this expression, we can compute the partial width $\Gamma(h \rightarrow gg)$ in the limit $m_h^2 \ll 4m_t^2$,

$$\Gamma(h \rightarrow gg) = \frac{\alpha_w \alpha_s^2}{72\pi^2} \frac{m_h^3}{m_W^2} . \quad (206)$$

The full expression can be shown to be

$$\Gamma(h \rightarrow gg) = \frac{\alpha_w \alpha_s^2}{72\pi^2} \frac{m_h^3}{m_W^2} \cdot \left| \frac{3}{2} \tau (1 - (\tau - 1) (\sin^{-1} \frac{1}{\sqrt{\tau}})^2) \right|^2 , \quad (207)$$

where $\tau = 4m_t^2/m_h^2$.

Another way to interpret this argument is that the shift of v in (183) is a change of scale for the SM. Then the 1-loop Higgs couplings to a gauge boson should be proportional to the 1-loop contribution to the renormalization group β function. The calculation just performed satisfies this, since (203) give the contribution of a quark to the QCD β function. Changing what needs to be changed, we can obtain the coupling of a Higgs boson to $\gamma\gamma$. The contribution from the top quark and the W boson to the QED vacuum polarization is

$$i(k^2 g^{\mu\nu} - k^\mu k^\nu) \frac{\alpha}{4\pi} \left[-\frac{22}{3} + \frac{1}{3} + \frac{4}{3} \cdot 3 \cdot \left(\frac{2}{3}\right)^2 \right] \log \frac{\Lambda^2}{m_{t,W}^2} . \quad (208)$$

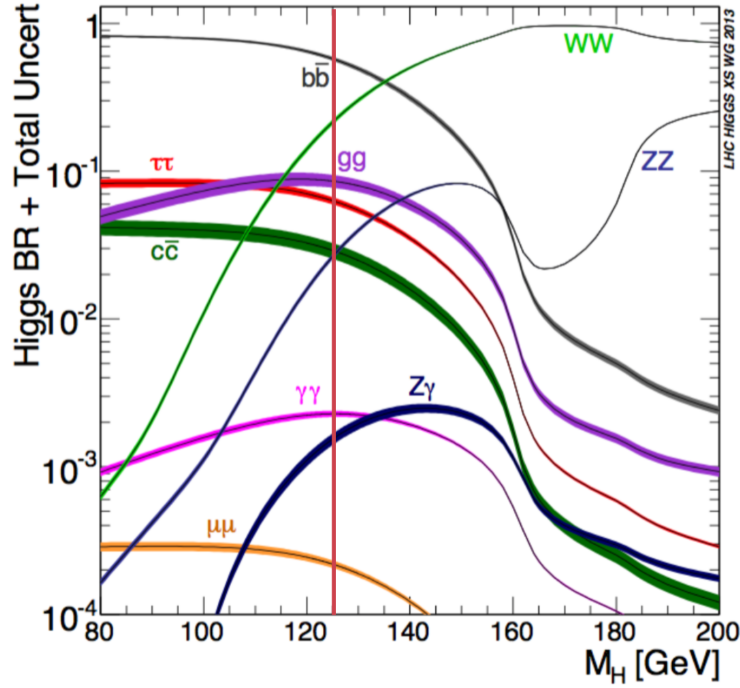


Figure 30: Standard Model predictions for the branching ratios of the Higgs boson as a function of the its mass, from [45].

The first term here is contribution from the W , it is just the standard vector boson contribution to the β function for an $SU(2)$ gauge theory. The second term comes from the Higgs boson that the W boson must eat to become massive. The third term comes from the top quark; the last two factors are the top quark color factor and electric charge. In all, we find, for $m_h \ll 2m_W, 2m_t$,

$$\Gamma(h \rightarrow \gamma\gamma) = \frac{\alpha_w \alpha^2}{144\pi^2} \frac{m_h^3}{m_W^2} \left| \frac{21}{4} - \frac{4}{3} \right|^2. \quad (209)$$

Careful evaluation, including all finite mass effects and the QCD corrections to the gluon width, gives

$$BR(h \rightarrow gg) = 8.6\% \quad BR(h \rightarrow \gamma\gamma) = 0.23\%. \quad (210)$$

We are now ready to put all of the pieces together to compile the SM predictions for the various Higgs boson branching ratios. Figure 30 shows the predictions as a function of the Higgs boson mass. It is a useful exercise to understand the shape of the curves based on the physics discussed in this section. The position of the observed Higgs resonance is shown by the vertical line. At this mass value, there are 10 distinct final states with branching fractions larger than 10^{-4} , including the $s\bar{s}$ channel not shown on this plot.

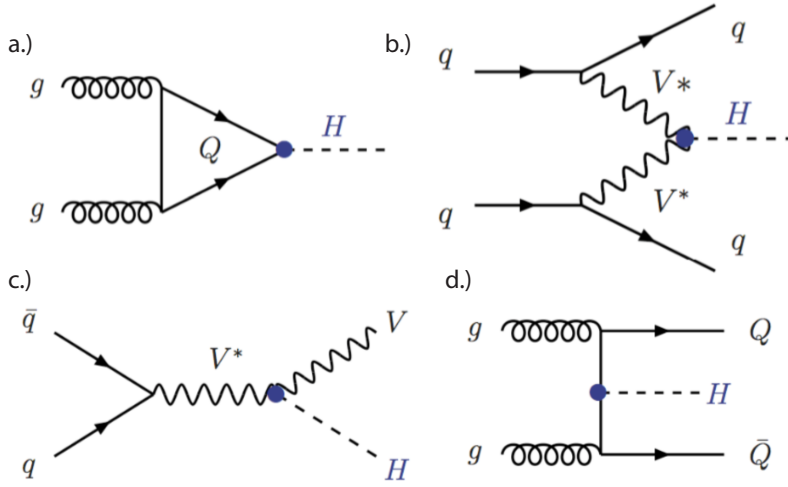


Figure 31: Reactions producing the Higgs boson in pp collisions

6.2 Study of the Higgs boson at the LHC

With this understanding of the Higgs boson couplings, I will review very briefly the results for Higgs boson couplings obtained by the ATLAS and CMS experiments. The most important processes for the production of a Higgs boson at the LHC are those shown in Fig. 31: gluon-gluon fusion, vector boson fusion, radiation of the Higgs boson from a W or Z (“Higgsstrahlung”), and associate production of a Higgs boson with a pair of top quarks. The cross sections predicted for these processes for a 125 GeV Higgs boson are shown in Fig. 32.

The four reactions have different advantages for the study of Higgs decays. Gluon-gluon fusion has the highest cross section, so it gives access to rare Higgs decays. In vector boson fusion, Higgs events are tagged by the presence of forward quark jets, reducing the background from non-Higgs SM processes. This reaction also has the smallest theoretical error on the predicted cross section. Higgsstrahlung also gives tagged Higgs decays. It also can lead to highly boosted Higgs bosons, which is an advantage for isolating the $h \rightarrow b\bar{b}$ decay. Finally, the top associated production process gives access to the $ht\bar{t}$ coupling.

In all cases, what is measured is a combination of the cross section for Higgs production and the branching fraction for Higgs decay into the observed final state. This observable is related to the Higgs couplings through

$$\sigma(pp \rightarrow A\bar{A} \rightarrow h)BR(h \rightarrow B\bar{B}) \sim \frac{\Gamma(h \rightarrow A\bar{A})\Gamma(h \rightarrow B\bar{B})}{\Gamma_h}. \quad (211)$$

In this relation, $A\bar{A}$ is the parton combination used to produce the Higgs boson— gg ,

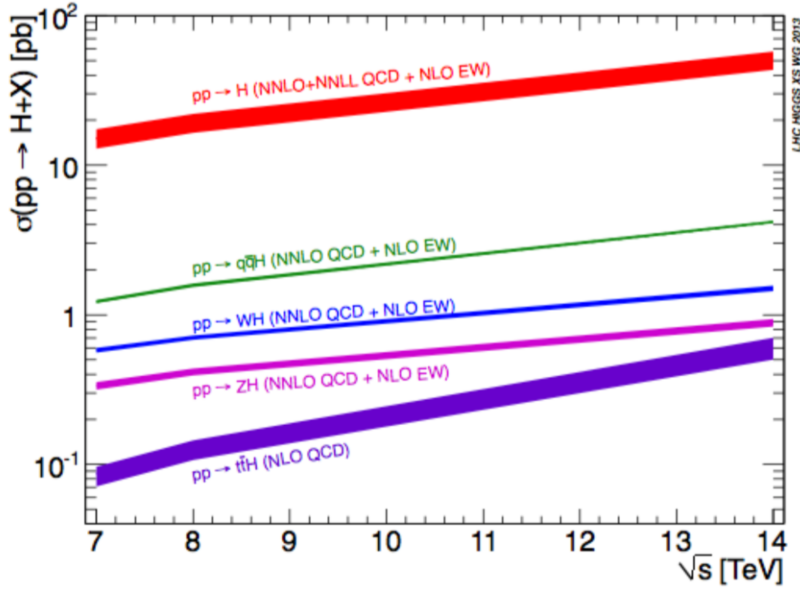


Figure 32: Cross sections for Higgs production in pp collisions for a 125 GeV Higgs boson, from [48].

WW or ZZ , and tt , respectively, for the processes in Fig. 32. The measured rates are quoted in terms of the *signal strength* μ

$$\mu = \sigma(pp \rightarrow h \rightarrow B\bar{B}) / (\text{SM prediction}) . \quad (212)$$

Note that, if a departure from the SM value $\mu = 1$ is seen, this might be due to a nonstandard value of the $hA\bar{A}$ coupling, the $hB\bar{B}$ coupling, or the Higgs total width. Multiple measurements would be needed to resolve this ambiguity.

The original strategy for observing the Higgs boson at the LHC used the characteristic decay modes in which this particle could be reconstructed as a resonance.

$$h \rightarrow \gamma\gamma , \quad h \rightarrow ZZ^* \rightarrow 4 \text{ leptons} \quad (213)$$

These modes correspond to branching fractions of

$$0.23\% \quad \text{and} \quad 0.012\% \quad (214)$$

With production cross sections of about 20 pb at 7 TeV, these processes have rates corresponding to fractions

$$4 \times 10^{-13} \quad \text{and} \quad 2 \times 10^{-14} , \quad (215)$$

respectively, of the pp total cross section. The observation of these very tiny components of the total reaction rate at the LHC is quite an achievement! Signals of the Higgs resonance in LHC run 1 data are shown in Fig. 33.

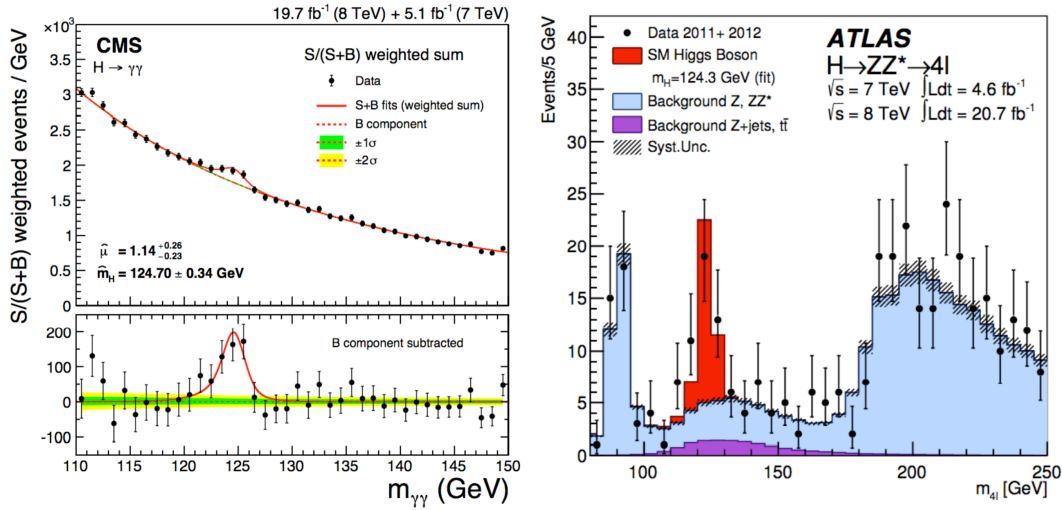


Figure 33: Signals of the Higgs boson resonance at the LHC in run 1: left: Higgs resonance in the $m(\gamma\gamma)$ distribution, from [49]; right: Higgs resonance in the $m(4\ell)$ distribution [50].

Once we are convinced that the Higgs resonance is actually present at a mass of 125 GeV, we can look for the signatures of this resonance in other decay modes. Higgs decays to these channels give larger total rates than the decays to the discovery modes. But, these channels produce events that are not obviously distinguishable from other SM reactions.

An example is

$$pp \rightarrow h \rightarrow W^+W^- \rightarrow \ell^+\ell^-\nu\bar{\nu} . \quad (216)$$

The observable properties of these events overlap strongly with events from

$$pp \rightarrow W^+W^- \rightarrow \ell^+\ell^-\nu\bar{\nu} . \quad (217)$$

The signal to background ratio can be enhanced by selecting the region where $m(\ell^+\ell^-)$ and the angle between the two leptons are both relatively small. It is also necessary to apply a jet veto (that is, to select events with at most 1 high- p_T jet) in order to avoid background from

$$pp \rightarrow t\bar{t} \rightarrow b\bar{b}\ell^+\ell^-\nu\bar{\nu} . \quad (218)$$

Figure 34 shows the distributions in $m(\ell^+\ell^-)$ for four event selections from the ATLAS analysis at 8 TeV. The histograms show the SM simulation of this event sample, with the various colored bands indicating the contributions of expected processes. The largest event rates come from $pp \rightarrow WW$ and, for the 1-jet events shown in the bottom row, $pp \rightarrow t\bar{t}$. The data points indicate a 10% excess rate over the SM expectation from processes that do not involve a Higgs boson, which is well accounted for by the expected rate for Higgs production.

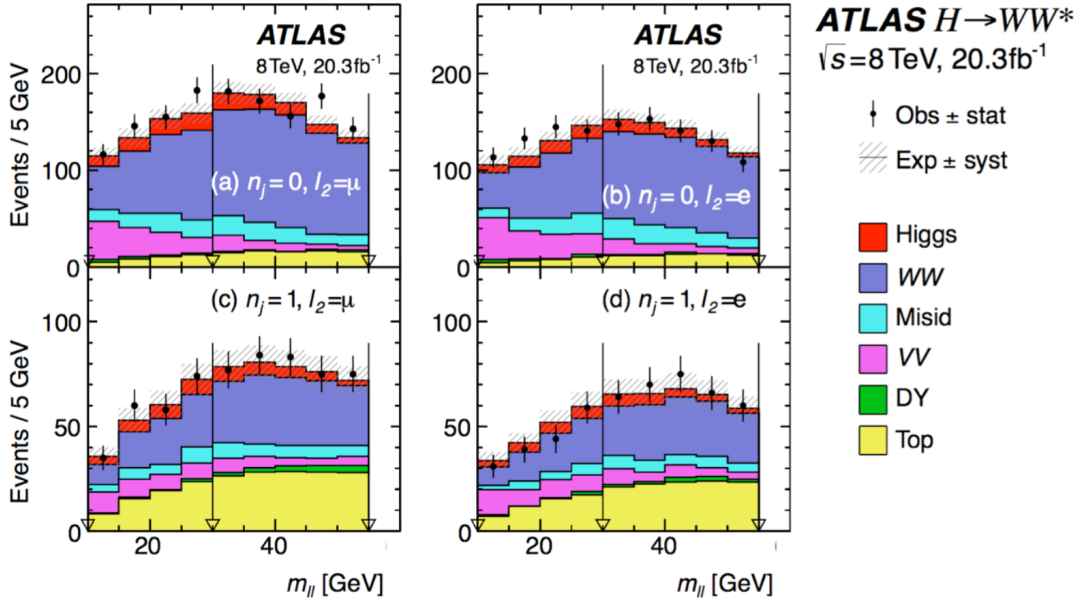


Figure 34: Evidence for the Higgs boson in its decay to WW^* , from [51].

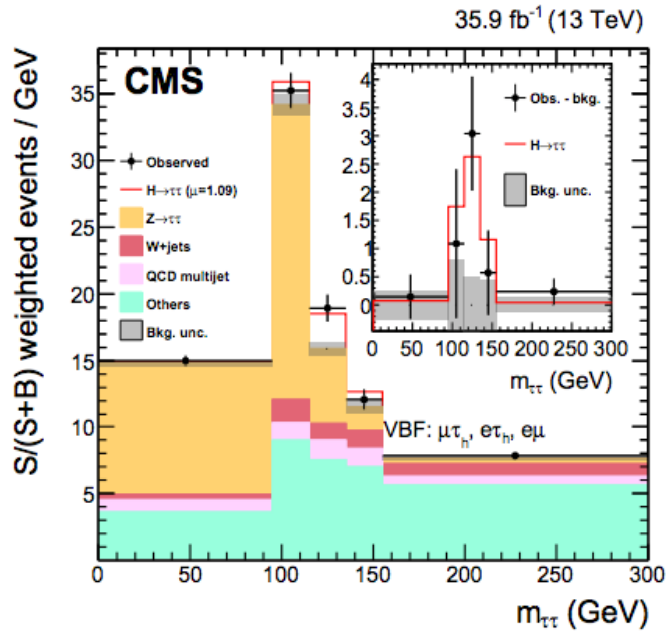


Figure 35: Evidence for the Higgs boson decay to $\tau^+\tau^-$, from [52].

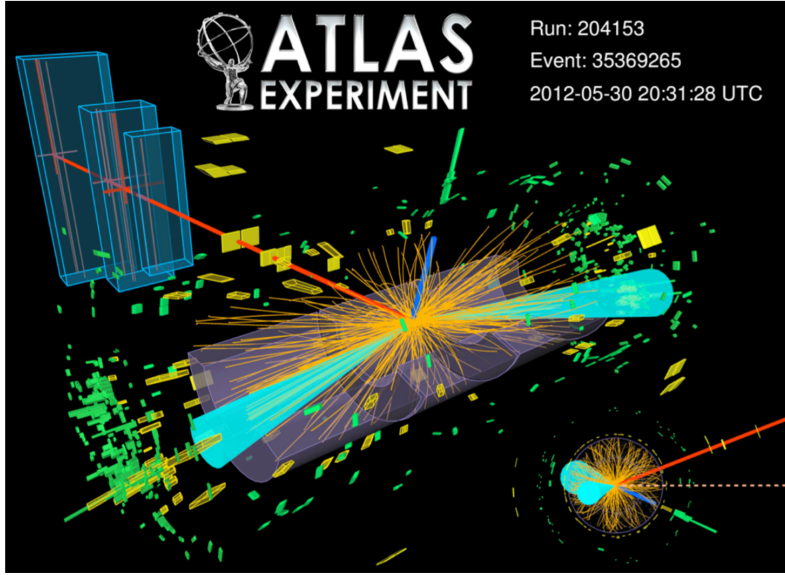


Figure 36: A candidate event for vector boson fusion production of a Higgs boson decaying to $\tau^+\tau^-$, from [53].

Similar analyses support the presence of Higgs boson production and decay to $\tau^+\tau^-$. The most important backgrounds are

$$pp \rightarrow Z \rightarrow \tau^+\tau^- , \quad pp \rightarrow W^+W^- , \quad (219)$$

and QCD reactions where two jets in the final state fake the τ signatures. The strongest evidence for the reaction comes from vector boson fusion, since the tagging by forward jets helps to minimize the QCD background. Figure 35 shows the very recent CMS run 2 analysis with data from 13 TeV. These events are dominated by the large background from $Z \rightarrow \tau^+\tau^-$. However, this background can be understood using the observed distribution of $Z \rightarrow \mu^+\mu^-$ events. The backgrounds from WW and QCD are more challenging to estimate. Fig. 36 shows a candidate vector boson fusion $h \rightarrow \tau^+\tau^-$ event from ATLAS. I use the word “candidate” advisedly; probably this event is a $Z \rightarrow \tau^+\tau^-$ event produced by vector boson fusion.

The most challenging of the major modes of Higgs decay is the one with the highest branching ratio, $h \rightarrow b\bar{b}$. It is probably hopeless to observe this mode in gluon fusion at low Higgs p_T , since $gg \rightarrow b\bar{b}$ with $m(b\bar{b}) \sim 125$ GeV has a cross section about a million times larger than that of the Higgs process. Current analyses use the Higgsstrahlung process with a tagging W or Z

$$pp \rightarrow Vh , \quad h \rightarrow b\bar{b} \quad (220)$$

where V is W or Z . However, there are other SM processes with similar signatures

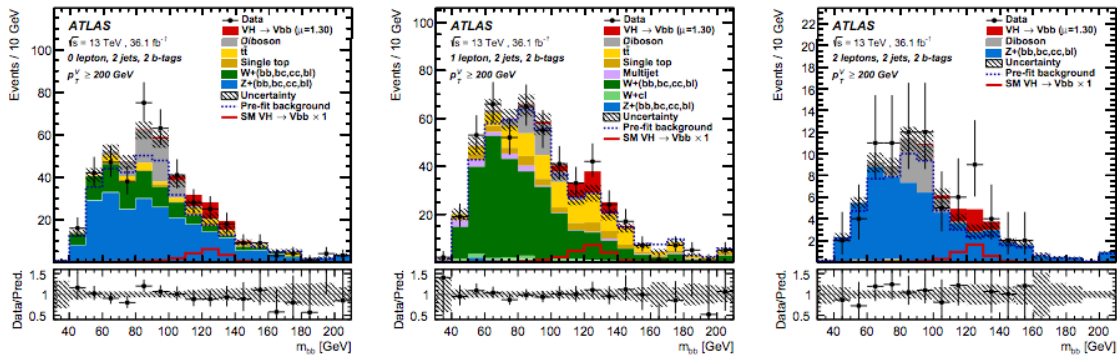


Figure 37: Evidence for the Higgs boson decay to $b\bar{b}$, from [54]. The three distributions show 0, 1, and 2-lepton events. The red (dark) boxes near the mass value of 125 GeV show the expectation from $pp \rightarrow Vh, h \rightarrow b\bar{b}$.

that do not involve a Higgs boson,

$$\begin{aligned}
 pp &\rightarrow VZ, & Z &\rightarrow b\bar{b} \\
 pp &\rightarrow Vg, & g &\rightarrow b\bar{b}.
 \end{aligned}
 \tag{221}$$

The second reaction involves an off-shell gluon with a mass near 125 GeV that converts to $b\bar{b}$. Convincing evidence for this decay has been obtained only very recently, in the 13 TeV data [54]. The current evidence from the ATLAS run 2 data is shown in Fig. 37. It is expected that discrimination of the three processes (220), (221) can be improved in an event sample in which the state recoiling against the vector boson is highly boosted, using techniques that measure the dijet mass and color flow. A recent analysis by CMS shows a small signal for $h \rightarrow b\bar{b}$ in a sample of high p_T jets recoiling against a gluon jet [55].

Figure 38 shows a summary of the measurements of the Higgs boson signal strengths made by ATLAS and CMS in run 1 of the LHC [56]. A signal strength of 0 indicates no presence of the Higgs boson. This hypothesis is excluded by run 1 data for all of the modes considered except $h \rightarrow b\bar{b}$. I have discussed above the more significant evidence for $h \rightarrow \tau^+\tau^-$ and $h \rightarrow b\bar{b}$ found already in run 2. A signal strength of 1 is the prediction of the SM. The measured rates agree with this prediction within about 30% accuracy. So the quantitative study of the Higgs boson has begun and will be improved as the LHC accumulates data.

7 Precision measurements of the Higgs boson properties

In the last segment of these lectures, I take a step outside the Standard Model. In this section, I will discuss the expectations for the couplings of the Higgs boson

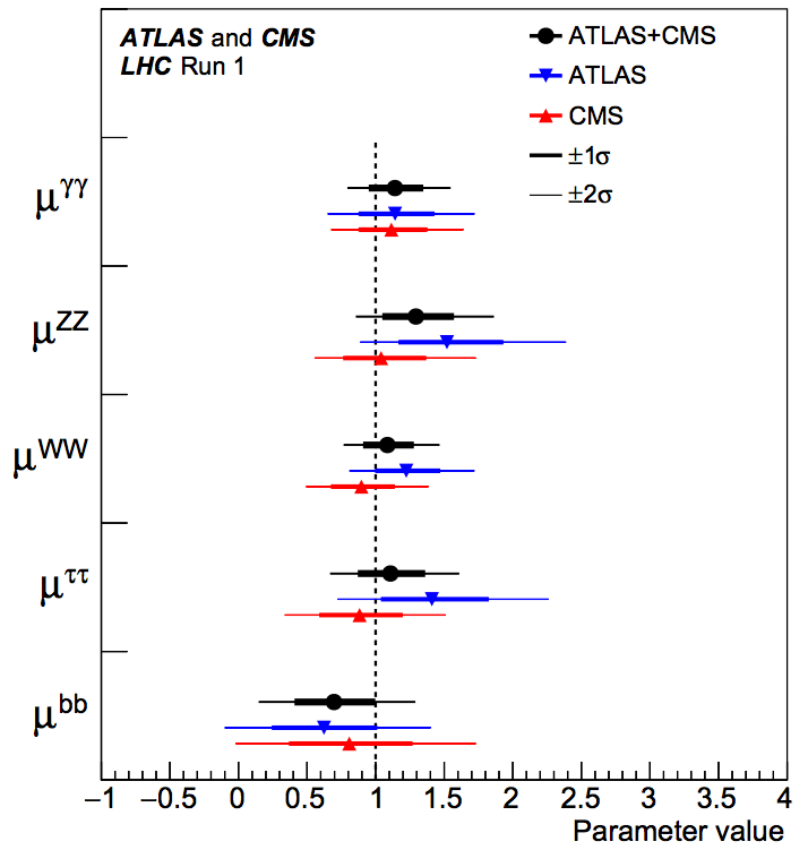


Figure 38: Summary of Higgs μ measurements, from [56].

in theories beyond the Standard Model. This is an interesting story that motivates a dedicated experimental campaign to measure the couplings of the Higgs boson with high precision. First, though, I will explain why I believe there must be new interactions of physics waiting to be discovered.

7.1 The mystery of electroweak symmetry breaking

I have shown in the previous lectures that the SM of weak interactions is an extremely successful theory in its own domain. It is not a complete theory of nature, but we can supplement it by adding gravity, quantum chromodynamics (QCD) as the theory of the strong interactions, and some model of dark matter and dark energy. It is also not difficult to add neutrino masses to the model, either by introducing three generations of right-handed neutrinos or by adding lepton-number-violating Majorana mass terms. Each of these additions accounts for some set of observed phenomena that is outside the range of topics considered in these lectures.

But this is not enough. A key part of the explanation for the structure of the weak interactions and the generation of masses for quarks, leptons, and gauge bosons is the spontaneous symmetry breaking of $SU(2) \times U(1)$ and the generation of the Yukawa couplings that link the symmetry-breaking Higgs field to the quarks and leptons. The structure that I have described leads immediately to questions about all of these ingredients:

- Why just quarks and leptons? What is the origin of the quantum number assignments (I, Y) for the matter particles seen in nature?
- What explains the spectrum of quark and lepton masses? The SM gives the relation

$$m_f = \frac{y_f v}{\sqrt{2}}, \quad (222)$$

where v is the Higgs field vacuum expectation value. But the y_f are renormalized parameters that cannot be predicted with the Standard Model. The presence of nonzero CKM angles—and, with neutrinos, PMNS angles—adds further difficulty to this problem.

- What is the origin of the Higgs field? Is there only one such field, or are there multiplets of scalar fields with different quantum numbers? The SM makes the minimal choice of one Higgs multiplet. Is this necessary?
- Why is $SU(2) \times U(1)$ spontaneously broken? The shape of the Higgs potential energy function is an input for which the SM gives no explanation.

This last question merits more discussion. Here is the explanation for electroweak symmetry breaking given in the SM: The model instructs us to write the most general

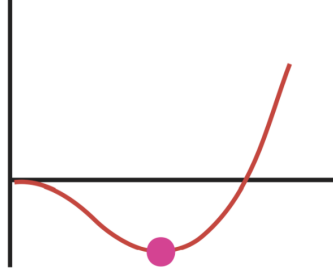


Figure 39: The Higgs potential $V(|\varphi|)$.

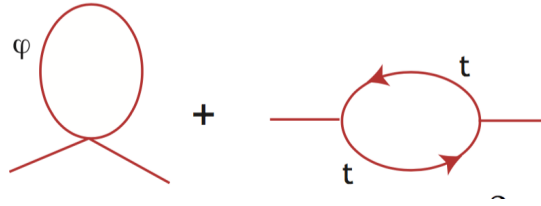


Figure 40: One-loop corrections to the μ^2 parameter from the Higgs field coupling to the top quark and from the Higgs field self-coupling.

renormalizable potential for the Higgs field φ ,

$$V(\varphi) = \mu^2|\varphi|^2 + \lambda|\varphi|^4 . \quad (223)$$

We assume that $\mu^2 < 0$. Then the potential has the correct shape, shown in Fig. 39, to drive spontaneous symmetry breaking.

Why must μ^2 be negative? That question cannot be addressed within the model. It is just a choice, perhaps a random one.

We get into deeper trouble if we try to take this explanation to a higher level of precision by computing the radiative corrections to the parameter μ^2 . The leading one-loop corrections, from loops containing the Higgs and top quark fields, are shown in Fig 40. They give

$$\mu^2 = \mu_{\text{bare}}^2 + \frac{\lambda}{8\pi^2}\Lambda^2 - \frac{3y_t^2}{8\pi^2}\Lambda^2 + \dots . \quad (224)$$

The diagrams are ultraviolet divergent. I have regularized them by cutting off their momentum integrals at a mass scale Λ , arbitrarily chosen to be the same for Higgs and top. The final value of μ^2 needed to produce the observed Higgs boson mass is $\mu^2 \approx -(100 \text{ GeV})^2$. So if Λ is much larger than 1 TeV, this formula requires large cancellations among the ingredients with no obvious explanation. If we assert

that the SM is correct up to the Planck scale, the first 33 significant figures must cancel. It is also apparent that the right-hand side contains both positive and negative contributions, so it is not obvious without invoking a much deeper explanation why the final answer after the cancellation should turn out to be negative.

The simplest resolution of this set of problems would be that there are new particles, not yet known to us, that generate additional diagrams contributing to the calculation of μ^2 . If these particles have masses of TeV size, they might cancel the divergences seen in (224) and—in the best case—leave over a calculable answer for μ^2 . However, we have not yet been able to discover these particles in high-energy experiments.

The general problem of the uncalculability of the parameter μ^2 is not new to high-energy physics. It is encountered in all systems in which a symmetry is spontaneously broken. Condensed matter physics gives many examples.

The most direct analogy to the Higgs theory comes in the phenomenon of superconductivity seen in most metals at cryogenic temperatures. The original papers on the Higgs mechanism by Englert and Brout, Higgs, and Guralnik, Hagen, and Kibble [9,10,11] all used the analogy to superconductivity to motivate their arguments. However, they used only a piece of the complete theory. Superconductivity was discovered in 1911 by Kamerlingh Onnes and was quickly seen to be associated with a sharp phase transition [57]. However, the explanation for this phase transition was not understood for another 45 years.

In 1950, Landau and Ginzburg proposed a phenomenological theory of superconductivity based on a scalar field with the potential (223) [58]. They assumed that the parameter μ^2 would be a function of temperature, taking negative values below the phase transition temperature T_C . Coupling this theory to electromagnetism, they found that the photon acquires a mass by the Higgs mechanism and that the scalar fields in the vacuum can transmit electric current frictionlessly. This theory turned out to be extremely successful in explaining many aspects of superconductivity, including the Meissner effect in which superconductors repel magnetic flux, the existence of Type I and Type II superconductors, and the systematics of the destruction of superconductivity by high currents or high magnetic fields.

However, this theory could not address the most important problem of why superconductivity occurred in the first place. The answer to that question waited until 1957, when Bardeen, Cooper, and Schrieffer discovered the mechanism that causes electrons in a metal to pair up into bound states and form a boson condensate with the properties of the Landau-Ginzburg scalar field [59].

In our understanding of the phase transition to symmetry breaking of $SU(2) \times U(1)$, we are now at the Landau-Ginzburg stage.

In the case of superconductivity, physicists knew that there must be a deeper

explanation that had to be given in terms of the interactions of electrons and atoms. For the symmetry-breaking of the weak interactions, any analogous explanation must involve new elementary particles outside the SM. We do not know what these particles are. We only know that we have not discovered them yet.

7.2 Expectations for the Higgs boson in theories beyond the Standard Model

Even if we cannot discover new heavy particles responsible for the Higgs potential energy, we can hope to find clues to the nature of these new particles and interactions by looking more deeply into the properties of the Higgs boson itself. In the previous lecture, I emphasized that the SM makes precise predictions for the couplings of the Higgs boson to all particles of the SM in terms of the measured masses of those particles. Any deviation from these predictions must indicate the presence of new interactions beyond the SM. In this and the next two sections, I will trace out the expectations for corrections to the Higgs properties in different classes of models of new physics.

To begin, I will present two sets of expectations for the properties of new physics models. The first is guidance from the concept that these models should solve the problem of the calculability of the Higgs potential. The second comes from a constraint that is well-satisfied in the precision electroweak measurements.

I have already explained that the parameter μ^2 in the Higgs potential cannot be computed within the SM. To construct a model in which μ^2 can be computed, that model must satisfy some special properties. In particular, some structure in the theory must require the cancellation of quadratically divergent Feynman diagrams which would otherwise add large, arbitrary terms to the final result for μ^2 .

There are two strategies to achieve this. The first is to include in the model a symmetry that forbids the appearance of the

$$\mu^2|\varphi|^2 \tag{225}$$

term in the Lagrangian. It is not so obvious how to construct such a symmetry, since the operator (225) seems to be completely neutral. It would be forbidden in a scale-invariant theory, but in quantum field theory scale invariance is usually explicitly broken by the running of coupling constants. Two schemes that do forbid such a term are supersymmetry, the spacetime symmetry that links fermions and bosons, and the identification of φ with a Goldstone boson of some spontaneous symmetry breaking at a very high mass scale. The computation of the Higgs potential in models of supersymmetry is reviewed in [60,61]. The computation of the Higgs potential in models in which the Higgs boson is a Goldstone boson is reviewed in [62,63]. There are also other proposed generalizations of the SM Higgs sector in which the Higgs potential is not calculable.

One of the properties of mass generation in the SM is the relation $m_W = m_Z c_w$, as we saw in (16). This property can be derived from a symmetry of the Higgs potential assumed in the SM. Since the relation works so well, it is suggested that generalizations of the SM Higgs sector should also have this property.

The origin of the relation (16) can be seen as follows: Look at the form of the vector boson mass matrix acting on the original $SU(2) \times U(1)$ fields,

$$m^2 = \begin{pmatrix} g^2 & & & \\ & g^2 & & \\ & & g^2 & -gg' \\ & & -gg' & g'^2 \end{pmatrix} \quad \text{on} \quad \begin{pmatrix} A^1 \\ A^2 \\ A^3 \\ B \end{pmatrix}. \quad (226)$$

The form of the matrix is dictated by the requirement that the matrix have a zero eigenvalue, associated with the massless photon, and that the part of the matrix acting on the $SU(2)$ fields (A^1, A^2, A^3) should be symmetric among these fields. The requirement for the latter statement is that the theory contains an $SO(3)$ transformation that rotates the $SU(2)$ gauge fields into one another and is unbroken even when the $SU(2)$ gauge symmetry is spontaneously broken. This extra transformation is called *custodial symmetry* [64].

Custodial symmetry is an accidental property of the SM Higgs potential. If we write

$$\varphi = \frac{1}{\sqrt{2}} \begin{pmatrix} \varphi^1 + i\varphi^2 \\ \varphi^0 + i\varphi^3 \end{pmatrix} \quad (227)$$

the Higgs potential depends only on the combination

$$|\varphi|^2 = (\varphi^0)^2 + (\varphi^1)^2 + (\varphi^2)^2 + (\varphi^3)^2. \quad (228)$$

A vacuum expectation value for φ^0 preserves the $SO(3)$ symmetry that acts on $(\varphi^1, \varphi^2, \varphi^3)$. From this observation, we understand why the SM satisfies (16).

There are many generalizations of the SM Higgs theory that also satisfy this condition. For example, we could introduce two or more scalar field multiplets with $(I, Y) = (\frac{1}{2}, \frac{1}{2})$. In the most general case, a different Higgs boson can be used to give mass to the charged leptons, d quarks, and u quarks, by writing the Higgs Yukawa interactions as

$$\mathbb{L} = -y_e L^\dagger \cdot \varphi_1 e_R - y_d Q^\dagger \cdot \varphi_2 d_R - y_u Q_a^\dagger \epsilon_{ab} \varphi_{3b}^\dagger u_R + h.c.. \quad (229)$$

In this equation, L is the left-handed lepton doublet, Q is the doublet of left-handed quarks, and all three Higgs multiplets have $I = \frac{1}{2}$, $Y = \frac{1}{2}$. The three Higgs fields should have a potential that aligns their vacuum expectation values so that the $U(1)$ symmetry giving electromagnetism remains unbroken. This structure can be extended to three generations by replacing the three Yukawa couplings by three 3×3 matrices.

The resulting theory shares with the Standard Model the property that, after a change of variables, the Higgs couplings are all CP even and flavor diagonal.

It can be shown that the Yukawa coupling with a complex conjugated field ϕ_3^\dagger is inconsistent with supersymmetry. Then, in models of supersymmetry, we must introduce at least two Higgs double fields, one with $I = \frac{1}{2}, Y = +\frac{1}{2}$, to give mass to the d quarks and leptons, and a different field with $I = \frac{1}{2}, Y = -\frac{1}{2}$, to give mass to the u quarks.

More complex Higgs field multiplets are also possible. Georgi and Machacek found a way to preserve custodial symmetry with Higgs bosons in higher representations, corresponding to spin I under the weak interaction $SU(2)$ symmetry [65,66]. For example, for $I = 1$, we could introduce a 3×3 matrix of fields

$$X = \begin{pmatrix} \chi^{0*} & \xi^+ & \chi^{++} \\ -\chi^{+*} & \xi^0 & \chi^+ \\ \chi^{++*} & -\xi^{+*} & \chi^0 \end{pmatrix}, \quad (230)$$

in which the rows are $SU(2)$ triplets and the columns have $Y = -1, 0, 1$, respectively. The potential for this field can be arranged to have $SU(2) \times SU(2)$ symmetry and a minimum at

$$\langle X \rangle = V \cdot \mathbf{1}_3 \quad (231)$$

that preserves the diagonal $SU(2)$ as a global symmetry. We need at least one $I = \frac{1}{2}$ Higgs multiplet to give mass to the quarks and leptons, but we can supplement this with additional Higgs fields with any value of I .

The criterion of custodial symmetry also provides guidance in constructing models of composite Higgs bosons that satisfy current phenomenological constraints. To provide examples of such models, let me begin by describing the Technicolor model introduced in 1978 by Weinberg and Susskind [67,68]. These authors introduced a copy of QCD with two massless techni-quark flavors (U, D), and with a strong interaction mass scale corresponding to a techni- ρ meson mass at 2 TeV. This model has $SU(2) \times SU(2)$ chiral symmetry, analogous to that in the known strong interactions. Just as happens there, the theory should have a spontaneous breaking of this symmetry to a diagonal $SU(2)$ symmetry, dynamically generating masses for the techni-quarks and creating three techni-pions as Goldstone bosons. The diagonal $SU(2)$ symmetry remains unbroken, and this plays the role of the custodial symmetry. If this model is coupled to the $SU(2) \times U(1)$ gauge symmetry of the SM, the W and Z bosons eat the Goldstone techni-pions and acquire mass through the Higgs mechanism. The W and Z masses obey (16), with

$$m_W = \frac{gF_\pi}{2}, \quad (232)$$

where F_π is the analogue of the pion decay constant in the technicolor interactions. We obtain the observed W and Z masses for $F_\pi = 246$ GeV, the Higgs field expectation

value in the SM. In this model, the Higgs boson would be a spin zero, isoscalar bound state of the U and D quarks and their antiquarks.

The Weinberg-Susskind technicolor model is now excluded. The model predicts a Higgs boson mass at about 1 TeV, and also too large an S parameter to be consistent with precision electroweak measurements. However, it points the way to more sophisticated models that also build the Higgs boson as a composite state.

An example is given by the following scenario, which uses the strong interaction chiral symmetry breaking in a different way: Introduce new QCD-like strong interactions at a mass scale of 10 TeV, with 4 associated quarks in real, rather than complex, representations of the gauge group. This theory has a chiral symmetry $SU(4)$, which is spontaneously broken to $SO(4)$ when the quarks dynamically acquire mass. $SU(4)$ has 15 generators, and $SO(4)$ has 6, so the symmetry-breaking creates $15 - 6 = 9$ Goldstone bosons. We might take two of the four quarks to transform as a doublet under the weak interaction $SU(2)$ and the other two to be weak interaction singlets that form a doublet under another $SU(2)$. Then the Goldstone boson multiplet will contain 4 bosons that transform as $(\frac{1}{2}, \frac{1}{2})$ under this $SU(2) \times SU(2)$. We can identify this multiplet with the Higgs boson doublet. This scenario realizes the idea of the Higgs doublet as a set of Goldstone bosons that, by Goldstone's theorem, stay massless while the strong interaction chiral symmetry is broken. In a set of models called *Little Higgs*, it is possible to perturb the strong interaction theory to produce a nonzero, calculable Higgs potential [69,70].

7.3 The Decoupling Theorem

Through the strategies described in the previous section, it is possible to build many models of the Higgs field that are more complex than the SM and yet compatible with all current experimental constraints. One's first instinct is that these models will lead to wildly different predictions for the properties of the Higgs boson that are easily distinguished experimentally. However, this is not correct. To distinguish models of the Higgs sector, it is necessary to make detailed measurements reaching a relatively high degree of precision. This is a consequence of the Decoupling Theorem, enunciated by Howard Haber in [71].

The Decoupling Theorem states: If the spectrum of the Higgs sector contains one Higgs boson of mass m_h , with all other Higgs particles having masses at least M , then the influence of these particles on the properties of the light Higgs boson is proportional to

$$m_h^2/M^2 . \tag{233}$$

If the Higgs sector contains additional particles, but these particles have masses of 1 TeV, they shift the properties of the known Higgs boson by corrections to the Higgs couplings at the percent level.

The proof of this theorem is quite straightforward. It uses the viewpoint of effective Lagrangians described in Section 5.4. As I have explained above, once we have measured the mass of the Higgs boson, the parameters of the SM relevant to the Higgs field are fixed, and the SM makes precise predictions for the Higgs couplings. On the other hand, I have also explained that the SM Lagrangian is the most general renormalizable Lagrangian with the known quark and lepton fields and the gauge symmetry $SU(3) \times SU(2) \times U(1)$. So, in an effective Lagrangian description, any perturbation of the Higgs couplings away from the SM predictions must be associated with operators of dimension 6. These operators have dimensionful coefficients. If they are generated by particles of mass M , their coefficients will be of order $1/M^2$.

This situation is challenging but not hopeless. It implies that the current level of agreement of the Higgs boson properties with the predictions of the SM—to 20–30%, as described in the previous section—is absolutely to be expected no matter how complex the Higgs sector might be. But, it offers the opportunity that, with measurements of higher precision, a picture of the Higgs boson entirely different from that of the SM might be revealed.

7.4 Effects on the Higgs boson couplings from models of new physics

To amplify this discussion of the effects of new physics on the SM Higgs couplings, I will now review some specific examples of those effects.

To begin, consider models with two Higgs scalar doublets. I remind you that supersymmetric models necessarily contain these effects, since supersymmetry requires two different Higgs doublets φ_u, φ_d to give mass to the u and d quarks.

In a model with two Higgs doublets, there are a total of 8 Higgs degrees of freedom. When the Higgs fields acquire vacuum expectation values, 3 of these bosons are eaten by W and Z when these particles obtain mass through the Higgs mechanism. The remaining physical Higgs particles include two CP-even neutral Higgs bosons h^0 and H^0 , a neutral pseudoscalar bosons A^0 , and a pair of charged Higgs bosons H^\pm . Most of the parameter space for such particles to have masses below 200 GeV has been excluded by searches at the LHC [72,73].

In general, these particles correspond to mixtures of the fields in the original two Higgs doublets. The mixing angle that defines the CP-even mass eigenstates is called α . For the CP-odd states, one mixture gives the eaten Goldstone bosons and orthogonal combination gives the physical boson mass eigenstates. The mixing angle that defines these linear combinations is called β , with

$$\tan \beta = \langle \varphi_u \rangle / \langle \varphi_d \rangle . \tag{234}$$

The properties of the observed Higgs boson are then predicted to be modified as a

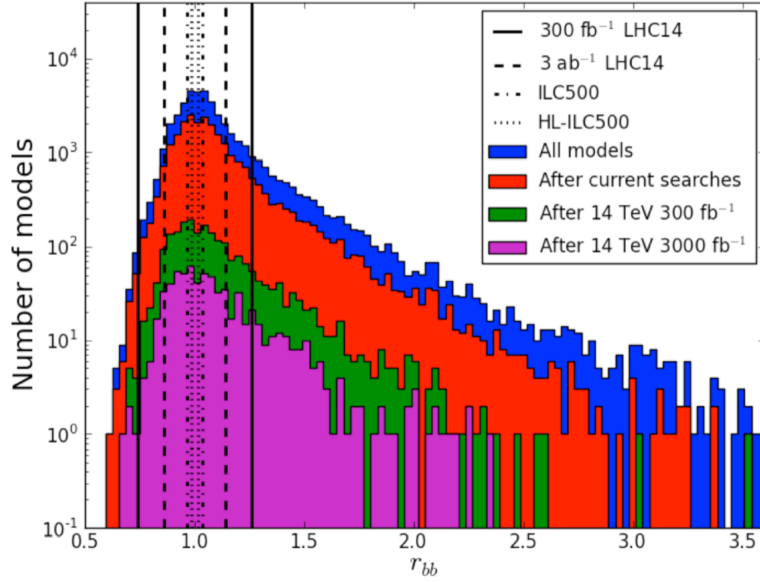


Figure 41: Values of $r_{bb} = \Gamma(h \rightarrow b\bar{b})/SM$ in a collection of about 250,000 allowed parameter points of the Minimal Supersymmetric Standard Model, from [74]. The colored bands show models that can be discovered in new particle searches in the various stages of the LHC and the HL-LHC.

result of these mixings. At the lowest order,

$$g(hdd) = -\frac{\sin \alpha}{\cos \beta} \frac{m_d}{v} \quad g(huu) = \frac{\cos \alpha}{\sin \beta} \frac{m_d}{v} . \quad (235)$$

The first of these modifications applies to the b quark-Higgs coupling, the second to the c and t couplings.

The Decoupling Theorem requires that the angles α , β cannot take arbitrary values but rather must be correlated. For example, in the minimal supersymmetric model,

$$-\frac{\sin \alpha}{\cos \beta} = 1 + \mathcal{O}\left(\frac{m_Z^2}{m_A^2}\right) , \quad (236)$$

consistent with the expected decoupling.

In supersymmetric models, the Higgs couplings also receive corrections from loop diagrams involving the partners of the quarks and leptons. Typically, the largest effects come from diagrams with the b squarks and the gluino. These diagrams obey decoupling, but they are enhanced when $\tan \beta$ is large.

Figure 41 shows the distribution of effects on the Higgs coupling $g(hbb)$ seen in a large collection of supersymmetric models constructed by Cahill-Rowley, Hewett,

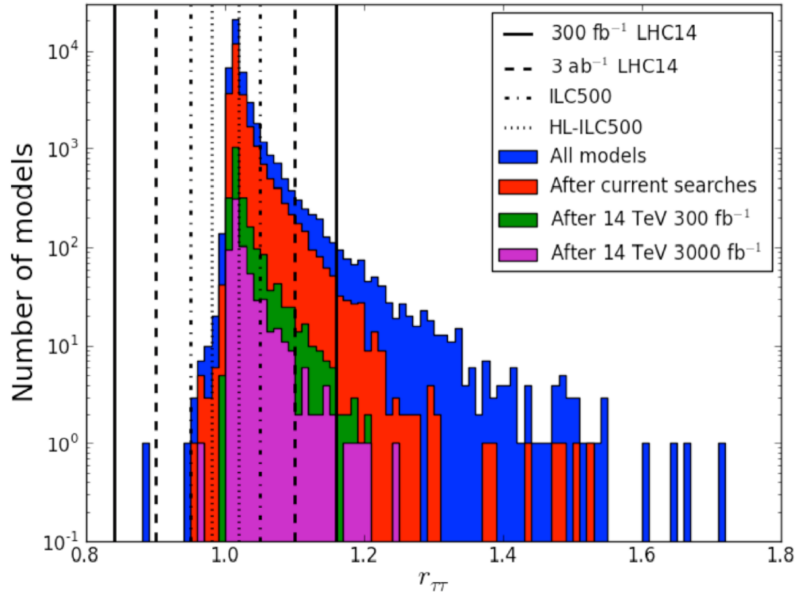


Figure 42: Values of $r_{\tau\tau} = \Gamma(h \rightarrow \tau^+\tau^-)/SM$ in a collection of about 250,000 allowed parameter points of the Minimal Supersymmetric Standard Model, from [74]. The colored bands show models that can be discovered in new particle searches in the various stages of the LHC and the HL-LHC.

Ismail, and Rizzo [74]. The colored panels in the figure show the sensitivity of the models to searches for supersymmetric particles at the LHC. It is interesting that the constraint from a precision measurement of the Higgs coupling to $b\bar{b}$ is essentially orthogonal to the current and expected constraints from LHC searches. Thus, the precision study of Higgs couplings gives us a new and different way to probe for new physics. Figure 42 shows the comparable distribution for perturbations of the coupling $g(h\tau\tau)$.

It is important to note that, while the presence of multiple Higgs doublets can have significant effects on the Higgs couplings to fermions, it typically has a smaller effect on the Higgs couplings to the W and Z bosons. In the minimal supersymmetric model,

$$g(hVV) = \frac{2m_V^2}{v} \cdot (1 + \mathcal{O}(\frac{m_Z^4}{m_A^4})) \quad (237)$$

for $V = W, Z$.

However, there are many other scenarios in which the Higgs couplings to W and Z are shifted as much as possible consistent with the Decoupling Theorem. If the Higgs boson mixes with a Higgs singlet field of mass m_s by an angle γ , the whole set

of Higgs couplings is shifted by

$$g(hVV) = \frac{2m_V^2}{v} \cdot \cos \gamma \quad (238)$$

where, typically, $\gamma \sim m_h/m_s$. A similar effect is produced by loop corrections from any new particles that modify the Higgs boson self-energy diagrams [75,76].

If the Higgs boson is a composite Goldstone boson, the Higgs couplings are corrected in a similar way by the nonlinear Lagrangian generated by spontaneous symmetry breaking. This gives

$$g(hVV) = \frac{2m_V^2}{v} \cdot (1 - v^2/F^2)^{1/2} \approx \frac{2m_V^2}{v} \cdot (1 - \frac{1}{2}v^2/F^2) , \quad (239)$$

an effect of 1–3%.

We have seen in the previous section that the decays

$$h \rightarrow gg , \quad h \rightarrow \gamma\gamma , \quad h \rightarrow \gamma Z \quad (240)$$

proceed through loop diagrams in which the dominant contributions come from particles for which $2M > m_h$. This means that new heavy particles have the potential to make large corrections to the rates of these decays. But this would only be true for particles that obtain their full mass from electroweak symmetry breaking.

As we have discussed already, the LHC measurement of $pp \rightarrow h \rightarrow \gamma\gamma$ already excludes a conventional fourth generation of quarks and lepton, up the mass at which the Yukawa coupling exceeds the unitarity bound. Any fermions that we have not yet discovered must then be vectorlike fermions, with equal electroweak quantum numbers for the left- and right-handed fields. Such fermions can obtain an $SU(2) \times U(1)$ -invariant mass term that does not require the Higgs field vacuum expectation value. For example, in models with extra space dimensions, excitations in the extra dimensions lead to separate Dirac fermion partners for the left- and right-handed states, which obtain masses $M \sim \pi/R$, where R is the size of the extra dimensions. The Higgs field can mix these states, leading to a small correction δM to the mass matrix that depends on the Higgs vacuum expectation value. The relative shift in the masses due to the Higgs vacuum expectation value is of the order of $(\delta M)^2/M^2$, and so the contribution of these particles to loop decays of the Higgs is suppressed by this factor—just as we would expect from the decoupling theorem.

A similar effect is seen in Little Higgs models. These models typically contain several new heavy quarks, which also mix with the top quark. An estimate of the corrections to the loop decays in the “Littlest Higgs” model is shown in Fig. 43 [77]. Mixing with heavy states can also modify the top quark Yukawa coupling. To fully

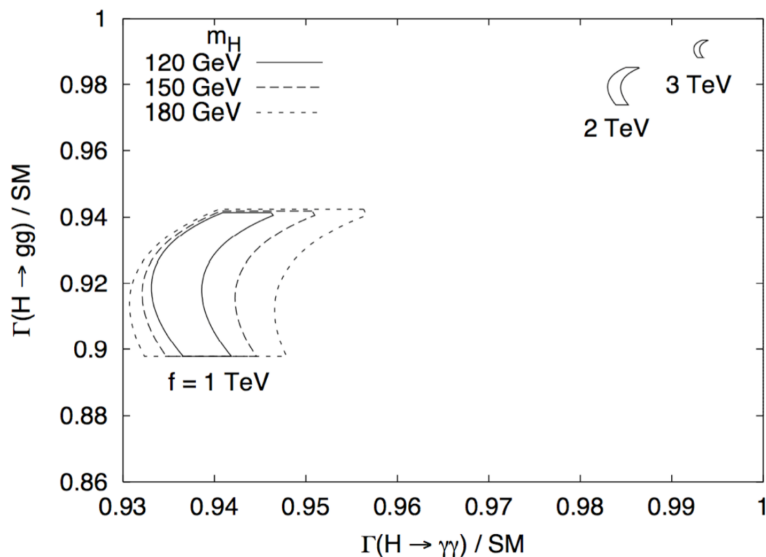


Figure 43: Corrections to $\Gamma(h \rightarrow \gamma\gamma)$ and $\Gamma(h \rightarrow gg)$ in the Littlest Higgs model.

understand the origin of the effects, it is important to measure separately the Higgs-gluon coupling and the Higgs-top coupling. The LHC might provide some complementary information by measuring Higgs boson production from gluon fusion at large p_T [78].

The Higgs boson also has a self-coupling that determines the shape of the Higgs potential. This is something of a special case in the general story of the Higgs couplings. On one hand, the Higgs self-coupling is more difficult to measure. While there are realistic proposals to measure the other Higgs couplings to the percent level, it will already be difficult to measure the self-coupling to the level of 10–20% accuracy. On the other hand, there are models that require very large deviations of the Higgs self-coupling from its SM value. Theories of baryogenesis, the origin of the matter-antimatter asymmetry of the universe, require a period when the early universe was out of thermal equilibrium. We are confident that the nonzero Higgs field expectation value was established at a phase transition from a hot symmetric phase just after the Big Bang. In the SM, this phase transition is predicted to be second-order and thus too smooth for substantial out-of-equilibrium effects. If the Higgs phase transition were strongly first-order, then it is possible the the universe might have developed a baryon-antibaryon asymmetry through CP- and baryon number violating interactions available at that time [79]. This requires values of the Higgs self-coupling substantially different from that in the SM, a 50% increase or more [80].

The result of this survey of new physics effects is that each individual Higgs coupling has its own personality and is guided by different types of models. In very

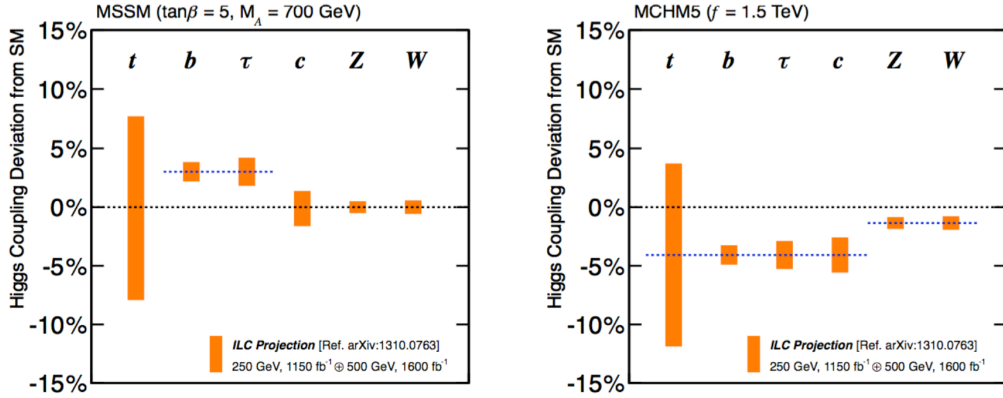


Figure 44: Patterns of deviations in Higgs couplings, from [81]. These examples of nonstandard Higgs effects are taken from a broader survey in [82].

broad terms:

- The Higgs couplings to fermions are sensitive to the presence of multiple Higgs doublets.
- The Higgs couplings to W and Z are sensitive to the presence of Higgs singlets and to compositeness of the Higgs boson.
- The Higgs couplings to gg and $\gamma\gamma$ are sensitive to the presence of new vectorlike fermions.
- The Higgs coupling to $t\bar{t}$ is sensitive to new heavy fermions that mix with the top quark and to composite structure of the top quark.
- The Higgs self-coupling has large deviations from its SM value in models of baryogenesis at the electroweak scale.

Each model of new physics predicts its own pattern of deviations of the Higgs couplings from the predictions of the SM. Two examples of these patterns, for specific supersymmetric and composite Higgs models, is shown in Fig. 44 [82]. The challenge for us is to measure the full suite of couplings with sufficient accuracy that we can read this pattern and use it to gain information about physics beyond the SM.

7.5 Measurement of the Higgs boson properties at e^+e^- colliders

Given the interest in obtaining precise knowledge of the couplings of the Higgs boson and the difficulty of reaching a sufficient level of accuracy at the LHC, it

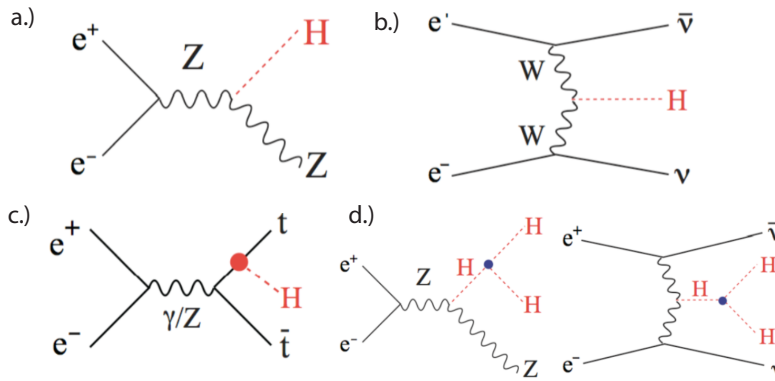


Figure 45: Reactions producing the Higgs boson in e^+e^- collisions

is not surprising that there are a number of proposals for new e^+e^- colliders that would specifically address the measurement of the Higgs couplings. It would be very valuable to study the Higgs boson with precision, in the same way that, in the 1990's, experiments at e^+e^- colliders carried out the precision study of the Z boson that I reviewed in Section 4 of these lectures.

The most important processes for the production of a Higgs boson at e^+e^- colliders are those shown in Fig. 45. These are analogous to the corresponding processes in hadron-hadron collisions shown in Fig. 31. The most important reaction near the Higgs threshold is radiation of the Higgs boson from a W or Z (“Higgsstrahlung”). At higher energies, Higgs bosons are also produced by vector boson fusion, associated production of a Higgs with a pair of top quarks, and the double Higgs production reactions shown in the last line of the figure. The cross sections predicted for the Higgsstrahlung and fusion reactions for a 125 GeV Higgs boson are shown in Fig. 46.

Just as at hadron-hadron colliders, the different reactions available at e^+e^- colliders have different advantages for the study of Higgs boson decays. Higgsstrahlung is available at the lowest center of mass energy. In this reaction, the Higgs boson is produced in association with a Z boson at a fixed energy. At 250 GeV in the center of mass, the Z boson has a lab frame energy of 110 GeV. To a first approximation, any Z boson observed at this energy arises from the reaction $e^+e^- \rightarrow Zh$, and whatever particles are on the other side of the event are the decay products of the Higgs boson. This is an ideal setup for measuring the branching ratios of the Higgs boson and for discovering and identifying Higgs decays into exotic modes not expected in the SM. Also, since $e^+e^- \rightarrow Zh$ events can be recognized without reconstruction of the Higgs boson, this reaction allows a measurement of the absolute cross section rather than a $\sigma \cdot BR$ as in (211). Then this reaction can be used to determine the absolute magnitude of the Z -Higgs coupling.

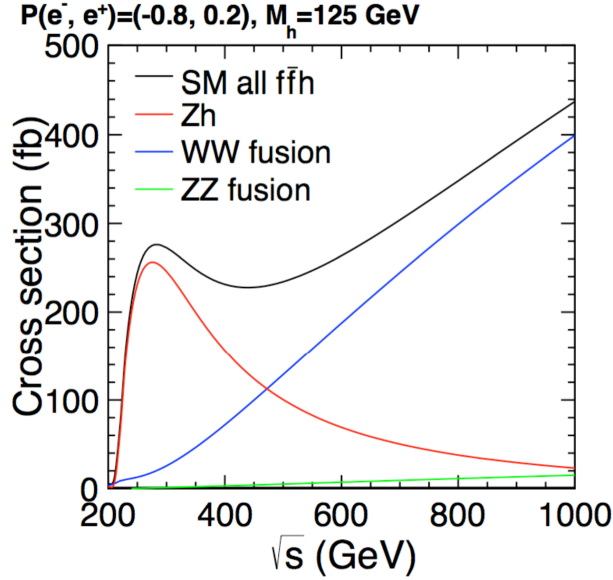


Figure 46: Cross sections for Higgs production in e^+e^- collisions for a 125 GeV Higgs boson.

The remaining reactions have complementary advantages. Using the Higgs branching ratio to $b\bar{b}$ measured with Higgsstrahlung, the WW fusion reaction can complement and firm up the measurement of the absolute normalization of Higgs couplings. As we see from Fig. 46, this reaction also gives higher statistics for Higgs decays at energies well above the threshold. The remaining processes allow the measurement of the Higgs coupling to top quarks and the Higgs self-coupling.

A complete description of the program of Higgs studies at e^+e^- colliders can be found in [83]. Here I will just provide some snapshots of this program. The recoil mass spectrum in the reaction $e^+e^- \rightarrow Zh$, $Z \rightarrow \mu^+\mu^-$ is shown in Fig. 47. The main background is $e^+e^- \rightarrow ZZ$ plus initial state radiation, a reaction that is understood to very high accuracy. We estimate that this measurement gives the Higgs boson mass with an accuracy of 15 MeV [85]. The precision Higgs coupling program actually needs a Higgs boson mass with this high accuracy. The partial widths for $h \rightarrow WW$ and $h \rightarrow ZZ$ depend strongly on the Higgs mass, so that this accuracy already corresponds to a 0.1% systematic error on the SM predictions. Figure 48 shows a Higgsstrahlung event with Higgs decay to $\tau^+\tau^-$. In general, these events are very characteristic of the various Zh event topologies. Figure 49, from the physics study for the CLIC accelerator, shows the separation of Higgs events e^+e^- annihilation events at 250 GeV into 4 Higgs categories and one background category by template fitting [87]. The figure shows that the modes $h \rightarrow gg$ and even $h \rightarrow c\bar{c}$, which has a 3% branching ratio in the SM, can be cleanly extracted. Figure 50 shows the recoil mass distribution for events with a Z boson plus missing momentum. The simulation assumes a high value

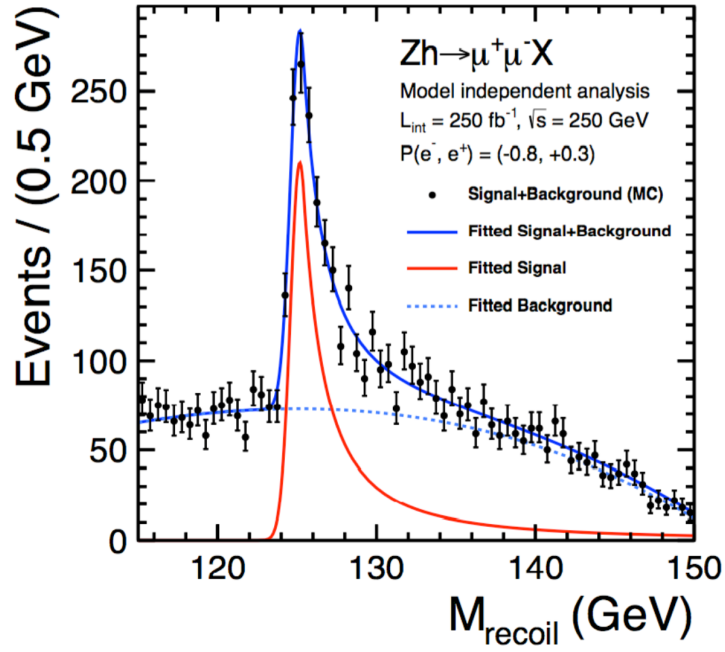


Figure 47: Recoil mass distribution in $e^+e^- \rightarrow Zh, Z \rightarrow \mu^+\mu^-$, from [85]

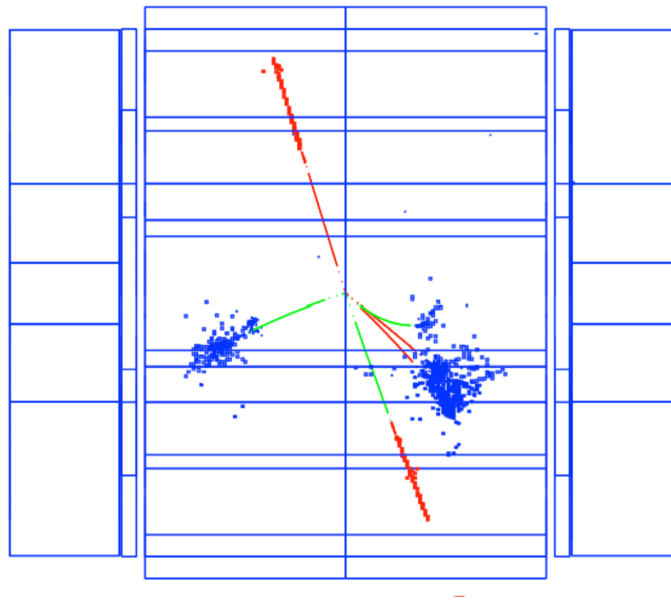


Figure 48: Event display of an $e^+e^- \rightarrow Zh, h \rightarrow \tau^+\tau^-$ event simulated in the ILD detector [84].

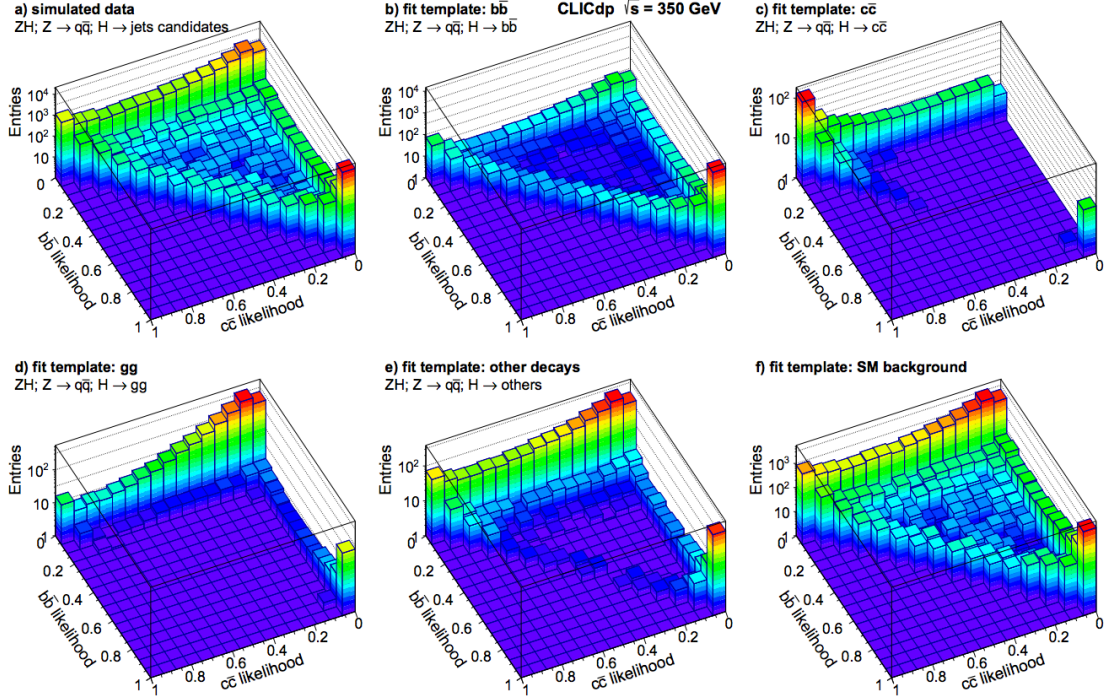


Figure 49: Identification of Higgs boson decays to hadronic final states by template fitting, from [87]. Note in particular the sharp discrimination of the modes $h \rightarrow b\bar{b}$, $h \rightarrow c\bar{c}$, $h \rightarrow gg$.

(10%) for the Higgs branching ratio to invisible decay products, but the figure makes clear that this process is visible at much smaller values of the branching ratio, well below 1% [86].

Finally, Figure 51, from [81], shows the accuracies for the determination of Higgs couplings to the full range of SM particles projected for the complete program of the International Linear Collider (ILC). For the Higgs decay to $\gamma\gamma$, the blue histograms show the result of combining the ILC data with the LHC measurement of $BR(h \rightarrow \gamma\gamma)/BR(h \rightarrow ZZ^*)$. The accuracy of the measurement of the Higgs coupling to the top quark is limited by the fact that this figure considers only ILC running at 500 GeV and below. Even an energy increase to 550 GeV would improve the accuracy of this measurement to 3%.

The precision study of Higgs boson couplings at an e^+e^- collider will then yield a wealth of information about the properties of this particle. Through the logic of the previous section, that information will give us insight not only into the existence of new physics beyond the SM but also into its qualitative nature. I look forward to this program as the next great project in the future of particle physics.

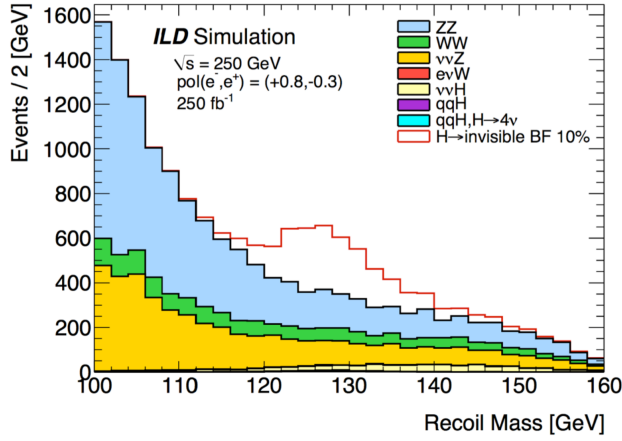


Figure 50: Recoil mass distribution for $e^+e^- \rightarrow Z + \text{missing}$ events, assuming a 10% branching ratio of the Higgs boson into invisible modes, from [86].

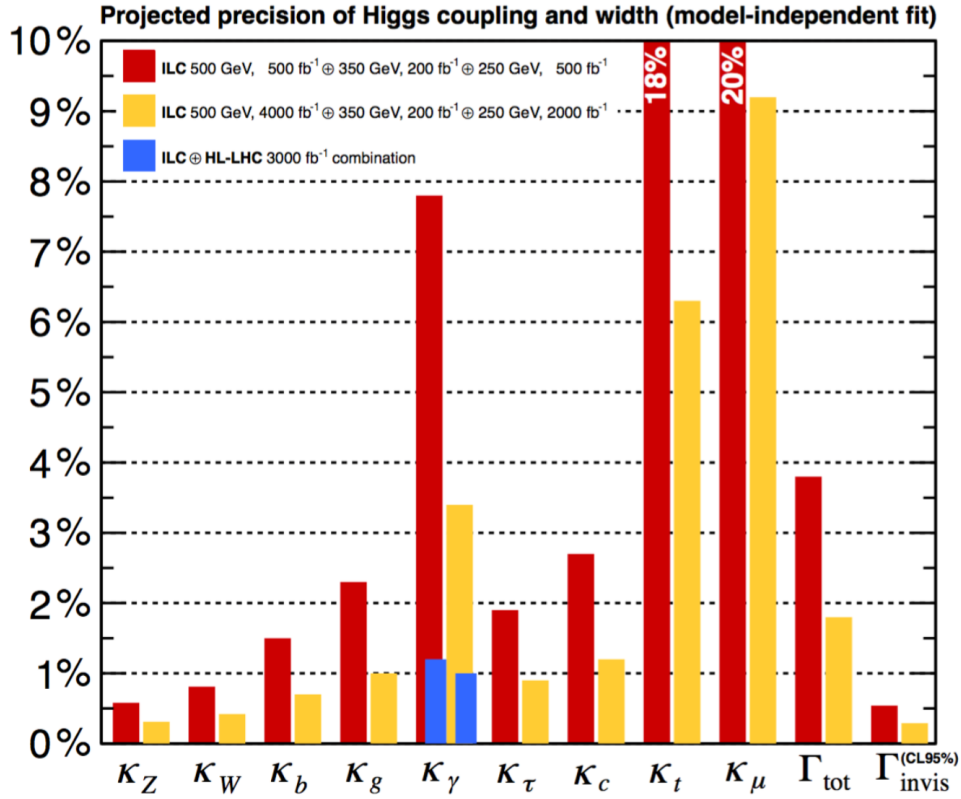


Figure 51: Higgs coupling uncertainties projected for the ILC, from [81].

8 Conclusions

In these lectures, I have developed the theory of the weak interaction from its experimental foundations in the $V-A$ effective theory, through the precision study of $SU(2) \times U(1)$ couplings at the Z resonance, to the present and future study of the couplings of the Higgs boson. We have learned much about this fundamental interaction of nature, but there is much more that we need to learn, and that we can learn from future experiments. The study of the weak interaction is not a closed subject but one that still contains tantalizing questions and promises to open new chapters in our exploration of particle physics.

References

- [1] S. Weinberg, Phys. Rev. Lett. **19**, 1264 (1967).
- [2] A. Salam, in *Proceedings of the 8th Nobel Symposium: Elementary Particle Theory*, N. Svartholm, ed. (Almqvist and Wiksell, 1968).
- [3] G. Aad *et al.* [ATLAS Collaboration], Phys. Lett. B **716**, 1 (2012) [arXiv:1207.7214 [hep-ex]].
- [4] S. Chatrchyan *et al.* [CMS Collaboration], Phys. Lett. B **716**, 30 (2012) [arXiv:1207.7235 [hep-ex]].
- [5] J. M. Cornwall, D. N. Levin and G. Tiktopoulos, Phys. Rev. D **10**, 1145 (1974) Erratum: [Phys. Rev. D **11**, 972 (1975)].
- [6] C. E. Vayonakis, Lett. Nuovo Cim. **17**, 383 (1976).
- [7] M. E. Peskin and D. V. Schroeder, *An Introduction to Quantum Field Theory*. (Westview Press, 1995).
- [8] M. D. Schwartz, *Quantum Field Theory and the Standard Model*. (Cambridge University Press, 2013).
- [9] F. Englert and R. Brout, Phys. Rev. Lett. **13**, 321 (1964).
- [10] P. W. Higgs, Phys. Lett. **12**, 132 (1964), Phys. Rev. Lett. **13**, 508 (1964).
- [11] G. S. Guralnik, C. R. Hagen and T. W. B. Kibble, Phys. Rev. Lett. **13**, 585 (1964).
- [12] C. Patrignani *et al.* (Particle Data Group), Chin. Phys. C **40**, 100001 (2016).

- [13] F. W. J. Koks and J. Van Klinken, Nucl. Phys. A **272**, 61 (1976).
- [14] M. Bardon, P. Norton, J. Peoples, A. M. Sachs and J. Lee-Franzini, Phys. Rev. Lett. **14**, 449 (1965).
- [15] J. G. H. de Groot *et al.*, Z. Phys. C **1**, 143 (1979).
- [16] G. Aad *et al.* [ATLAS Collaboration], Phys. Lett. B **701**, 31 (2011) [arXiv:1103.2929 [hep-ex]].
- [17] S. Chatrchyan *et al.* [CMS Collaboration], JHEP **1104**, 050 (2011) [arXiv:1103.3470 [hep-ex]].
- [18] P. Abreu *et al.* [DELPHI Collaboration], Eur. Phys. J. C **11**, 383 (1999).
- [19] I am grateful to Michael Hildreth for assembling this compilation of preliminary LEP 2 data.
- [20] S. Schael *et al.* [ALEPH and DELPHI and L3 and OPAL and LEP Electroweak Collaborations], Phys. Rept. **532**, 119 (2013) [arXiv:1302.3415 [hep-ex]].
- [21] E. A. Kuraev and V. S. Fadin, Sov. J. Nucl. Phys. **41**, 466 (1985) [Yad. Fiz. **41**, 733 (1985)].
- [22] S. Schael *et al.* [ALEPH and DELPHI and L3 and OPAL and SLD Collaborations and LEP Electroweak Working Group and SLD Electroweak Group and SLD Heavy Flavour Group], Phys. Rept. **427**, 257 (2006) [hep-ex/0509008].
- [23] O. Nicosini and L. Trentadue, Nucl. Phys. B **318**, 1 (1989).
- [24] G. Abbiendi *et al.* [OPAL Collaboration], Eur. Phys. J. C **19**, 587 (2001) [hep-ex/0012018]. I thank Toshinori Mori for the use of this figure.
- [25] D. Decamp *et al.* [ALEPH Collaboration], Z. Phys. C **48**, 365 (1990).
- [26] R. Akers *et al.* [OPAL Collaboration], Z. Phys. C **65**, 17 (1995).
- [27] K. Abe *et al.* [SLD Collaboration], Phys. Rev. Lett. **80**, 660 (1998) [hep-ex/9708015]. Phys. Rev. Lett. **94**, 091801 (2005) [hep-ex/0410042].
- [28] A. Heister *et al.* [ALEPH Collaboration], Eur. Phys. J. C **20**, 401 (2001) [hep-ex/0104038].
- [29] K. Abe *et al.* [SLD Collaboration], Phys. Rev. Lett. **86**, 1162 (2001) [hep-ex/0010015].
- [30] K. Abe *et al.* [SLD Collaboration], Phys. Rev. Lett. **81**, 942 (1998).

- [31] J. Erler and A. Freitas, in [12]
- [32] W. J. Marciano and A. Sirlin, Phys. Rev. D **29**, 945 (1984) Erratum: [Phys. Rev. D **31**, 213 (1985)].
- [33] M. E. Peskin and T. Takeuchi, Phys. Rev. Lett. **65**, 964 (1990), Phys. Rev. D **46**, 381 (1992).
- [34] M. Baak *et al.* [Gfitter Group], Eur. Phys. J. C **74**, 3046 (2014) [arXiv:1407.3792 [hep-ph]].
- [35] M. S. Chanowitz and M. K. Gaillard, Nucl. Phys. B **261**, 379 (1985).
- [36] V. Khachatryan *et al.* [CMS Collaboration], Phys. Lett. B **762**, 512 (2016) [arXiv:1605.09047 [hep-ex]].
- [37] W. Alles, C. Boyer and A. J. Buras, Nucl. Phys. B **119**, 125 (1977).
- [38] K. Hagiwara, R. D. Peccei, D. Zeppenfeld and K. Hikasa, Nucl. Phys. B **282**, 253 (1987).
- [39] B. Grzadkowski, M. Iskrzynski, M. Misiak and J. Rosiek, JHEP **1010**, 085 (2010) [arXiv:1008.4884 [hep-ph]].
- [40] S. Willenbrock and C. Zhang, Ann. Rev. Nucl. Part. Sci. **64**, 83 (2014) [arXiv:1401.0470 [hep-ph]].
- [41] B. Henning, X. Lu and H. Murayama, JHEP **1601**, 023 (2016) [arXiv:1412.1837 [hep-ph]].
- [42] A. Falkowski, M. Gonzalez-Alonso, A. Greljo, D. Marzocca and M. Son, arXiv:1609.06312 [hep-ph].
- [43] S. Dawson, Nucl. Phys. B **249**, 42 (1985).
- [44] J. F. Gunion, H. E. Haber, G. L. Kane and S. Dawson, *The Higgs Hunter's Guide*. (Westview Press, 2000).
- [45] S. Heinemeyer *et al.* [LHC Higgs Cross Section Working Group], *Handbook of LHC Higgs Cross Sections: 3. Higgs Properties*, arXiv:1307.1347 [hep-ph].
- [46] CMS Collaboration, CMS-PAS-HIG-13-002 (2013).
- [47] M. I. Vysotsky, arXiv:1312.0474 [hep-ph].
- [48] M. Carena, C. Grojean, M. Kado, and V. Sharma, in K. A. Olive *et al.* (Particle Data Group), Chin. Phys. **C38**, 090001 (2014).

- [49] V. Khachatryan *et al.* [CMS Collaboration], *Eur. Phys. J. C* **74**, no. 10, 3076 (2014) [arXiv:1407.0558 [hep-ex]].
- [50] G. Aad *et al.* [ATLAS Collaboration], *Phys. Lett. B* **726**, 88 (2013) Erratum: [*Phys. Lett. B* **734**, 406 (2014)] [arXiv:1307.1427 [hep-ex]].
- [51] G. Aad *et al.* [ATLAS Collaboration], *Phys. Rev. D* **92**, 012006 (2015) [arXiv:1412.2641 [hep-ex]].
- [52] A. M. Sirunyan *et al.* [CMS Collaboration], arXiv:1708.00373 [hep-ex].
- [53] ATLAS Collaboration, ATLAS-CONF-2013-108 (2013).
- [54] M. Aaboud *et al.* [ATLAS Collaboration], arXiv:1708.03299 [hep-ex].
- [55] CMS Collaboration, CMS-PAS-HIG-17-010 (2017).
- [56] M. Carena, C. Grojean, M. Kado, and V. Sharma, in C. Patrignani *et al.* (Particle Data Group), *Chin. Phys.* **C40**, 100001 (2016).
- [57] H. K. Onnes, *Commun. Phys. Lab. Univ. Leiden.* **12**, 120 (1911).
- [58] V. L. Ginzburg and L. D. Landau, *Zh. Eksp. Teor. Fiz.* **20**, 1064 (1950).
- [59] J. Bardeen, L. N. Cooper and J. R. Schrieffer, *Phys. Rev.* **108**, 1175 (1957).
- [60] S. P. Martin, in *Perspectives on Supersymmetry*, G. L. Kane, ed. (World Scientific, 1998) [hep-ph/9709356].
- [61] M. E. Peskin, in *Exploring New Frontiers Using Collider and Neutrinos (TASI 2006)*, S. Dawson and R. Mohapatra, eds. (World Scientific, 2008) [arXiv:0801.1928 [hep-ph]].
- [62] R. Contino, Y. Nomura and A. Pomarol, *Nucl. Phys. B* **671**, 148 (2003) [hep-ph/0306259].
- [63] T. Gherghetta, in *Physics of the Large and the Small (TASI 09)*, C. Csaki and S. Dodelson, eds. (World Scientific, 2011) [arXiv:1008.2570 [hep-ph]].
- [64] P. Sikivie, L. Susskind, M. B. Voloshin and V. I. Zakharov, *Nucl. Phys. B* **173**, 189 (1980).
- [65] H. Georgi and M. Machacek, *Nucl. Phys. B* **262**, 463 (1985).
- [66] H. E. Logan and V. Rentsala, *Phys. Rev. D* **92**, no. 7, 075011 (2015) [arXiv:1502.01275 [hep-ph]].
- [67] S. Weinberg, *Phys. Rev. D* **19**, 1277 (1979).

- [68] L. Susskind, Phys. Rev. D **20**, 2619 (1979).
- [69] N. Arkani-Hamed, A. G. Cohen, E. Katz and A. E. Nelson, JHEP **0207**, 034 (2002) [hep-ph/0206021].
- [70] M. Schmaltz and D. Tucker-Smith, Ann. Rev. Nucl. Part. Sci. **55**, 229 (2005) [hep-ph/0502182].
- [71] H. E. Haber, in *Electroweak Symmetry Breaking*, F. Csikor and G. Pocsik, eds. (World Scientific, 1995) [hep-ph/9501320].
- [72] R. K. Dewanjee [CMS Collaboration], PoS DIS **2016**, 100 (2016).
- [73] ATLAS Collaboration, ATLAS-CONF-2017-050 (2017).
- [74] M. Cahill-Rowley, J. Hewett, A. Ismail and T. Rizzo, Phys. Rev. D **90**, 095017 (2014) [arXiv:1407.7021 [hep-ph]].
- [75] V. Barger, T. Han, P. Langacker, B. McElrath and P. Zerwas, Phys. Rev. D **67**, 115001 (2003) [hep-ph/0301097].
- [76] N. Craig, C. Englert and M. McCullough, Phys. Rev. Lett. **111**, 121803 (2013) [arXiv:1305.5251 [hep-ph]].
- [77] T. Han, H. E. Logan, B. McElrath and L. T. Wang, Phys. Lett. B **563**, 191 (2003) Erratum: [Phys. Lett. B **603**, 257 (2004)] [hep-ph/0302188].
- [78] C. Grojean, E. Salvioni, M. Schlaffer and A. Weiler, JHEP **1405**, 022 (2014) [arXiv:1312.3317 [hep-ph]].
- [79] D. E. Morrissey and M. J. Ramsey-Musolf, New J. Phys. **14**, 125003 (2012) [arXiv:1206.2942 [hep-ph]].
- [80] A. Noble and M. Perelstein, Phys. Rev. D **78**, 063518 (2008) [arXiv:0711.3018 [hep-ph]].
- [81] K. Fujii *et al.*, arXiv:1506.05992 [hep-ex].
- [82] S. Kanemura, K. Tsumura, K. Yagyu and H. Yokoya, Phys. Rev. D **90**, 075001 (2014) [arXiv:1406.3294 [hep-ph]].
- [83] H. Baer *et al.*, *The International Linear Collider Technical Design Report - Volume 2: Physics*, arXiv:1306.6352 [hep-ph].
- [84] I thank Manqi Ruan for the use of this figure.
- [85] J. Yan, S. Watanuki, K. Fujii, A. Ishikawa, D. Jeans, J. Strube, J. Tian and H. Yamamoto, Phys. Rev. D **94**, 113002 (2016) [arXiv:1604.07524 [hep-ex]].

- [86] J. Tian and K. Fujii, Nucl. Part. Phys. Proc. **273-275**, 826 (2016).
- [87] H. Abramowicz *et al.*, Eur. Phys. J. C **77**, no. 7, 475 (2017) [arXiv:1608.07538 [hep-ex]].